

Inelastic light scattering in the regime of the persistent spin helix



Dissertation

zur Erlangung des Doktorgrades
der Naturwissenschaften (Dr. rer. nat.)
der Fakultät für Physik
der Universität Regensburg

vorgelegt von

Christoph Schönhuber

geboren am 01.12.1986
in Kelheim

Oktober 2015

Promotionsgesuch eingereicht am 08.07.2015

Die Arbeit wurde angeleitet von: Prof. Dr. Christian Schüller

Prüfungsausschuss:

Vorsitzender: Prof. Dr. Vladimir Braun

Erstgutachter: Prof. Dr. Christian Schüller

Zweitgutachter: Prof. Dr. Sergey Ganichev

Weiterer Prüfer: Prof. Dr. Rupert Huber

Contents

Contents	iii
1 Introduction	1
2 Basics	5
2.1 The material GaAs	5
2.2 Properties of GaAs-based quantum wells	7
2.3 Investigated samples	11
2.3.1 Sample structure	12
2.3.2 First characterization: PL and PLE	15
2.3.3 Fabrication of an electrical gate	17
2.4 Inelastic light scattering	19
2.4.1 General concept	19
2.4.2 Experimental setup	21
3 GaAs/AlGaAs quantum wells: Fundamental concepts	25
3.1 Electronic elementary excitations	25
3.1.1 Single-particle continua	25
3.1.2 Collective charge- and spin-density excitations	27
3.1.3 Scattering process	31
3.1.4 Scattering cross section and selection rules	33
3.2 Scattering from intersubband excitations	35
3.2.1 25 nm-wide quantum well	35
3.2.2 12 nm-wide quantum well	40
4 Spin-orbit coupling and the persistent spin helix	45
4.1 Origin of the $B = 0$ spin splitting	46
4.1.1 Bulk inversion asymmetry	47
4.1.2 Structure inversion asymmetry	51
4.1.3 The persistent spin helix	52
4.2 Intrasubband excitations in (001)-grown quantum wells	56
4.2.1 Theoretical considerations	56
4.2.2 Excitations in the regime of the persistent spin helix state	60
4.2.3 Angular dependency of the spin splitting	64

4.2.4	Impact of the sample design on the direction of the PSH	67
4.2.5	Excitations in polarized scattering geometry	69
4.2.6	Influence of an external electric field	72
4.3	Intrasubband excitations in (110)-grown quantum wells	75
4.3.1	Theoretical considerations	75
4.3.2	The persistent spin helix state in (110)-grown quantum wells	78
5	Anti-Stokes measurements	81
5.1	Wave-vector dependency	81
5.2	Temperature dependency	83
6	GaAs quantum wells in external magnetic fields	85
6.1	Landau quantization	85
6.2	Low and moderate magnetic fields	87
6.3	The magnetoplasmon and Bernstein modes	91
6.4	High magnetic fields	92
7	Conclusion	95
	Bibliography	99

Chapter 1

Introduction

Over the last few decades, spintronics has been grown to a major research topic in solid state physics (see, e. g., [Zut04, Fab07]), since it describes a very promising approach for a modern information technology. The utilization of an electron's spin instead of its charge opened new pathways for novel electronic devices and applications based on the spin degree of freedom in semiconductors. This revolutionary innovation aims to replace conventional technologies like CMOS¹ transistors, as the ongoing minimization of these charge-based devices faces upcoming limits due to quantum mechanical effects and uncontrollable heat production. These restrictions may be eluded by spin-based devices, but yet, a lot of research is required to establish this technology in commercial applications.

A pioneering work in spintronics was the proposal of a spin field-effect transistor (sFET) by S. Datta and B. Das in 1990 [Dat90]. Here, a ferromagnetic contact is used to inject spin-polarized electrons into a two-dimensional semiconductor channel. The spin precession inside the channel is dominated by spin-orbit coupling, which is controlled by an external gate on top of the device. After traveling through the channel, the electron is detected by another ferromagnetic contact but can exit the channel only for a spin orientation consistent with the polarization of the drain [Win04]. The essential impact on the functionality of the transistor is consequently given by the spin-orbit coupling, where between two major contributions may be distinguished: The Dresselhaus field [Dre55], which arises due a lack of inversion symmetry in the crystal lattice, and the Rashba field [Byc84], which is present only in low-dimensional semiconductors and caused by electric fields from modulation doping or external gates for instance. For the sFET, Datta and Das suggested a narrow-gap semiconductor with a dominant Rashba term, since it allows a manipulation of spin polarization by the electric top gate. The Dresselhaus contribution, however, was neglected in this theoretical approach. Even though a working sFET was already demonstrated a few years ago for very low temperatures ($T = 1.8\text{ K}$) [Koo09], a commercial application is rather unlikely due to the requirement of a ballistic transport in the semiconductor channel.

¹CMOS: complementary metal oxide semiconductor

As an evolution of this concept, J. Schliemann et al. proposed in 2003 a nonballistic spin-field-effect transistor based on both spin-orbit contributions [Sch03]. A special interplay with equal strengths of Rashba and Dresselhaus fields leads to a spin transport, which is tolerant against spin-independent scattering, and allows an operation in a diffusive regime. This promising prediction was reinforced three years later by the discovery of a new spin rotation symmetry for balanced Rashba and Dresselhaus coupling constants [Ber06]. A consequence of this symmetry is the already addressed lifetime enhancement of spin polarization and the emergence of a spin pattern called the persistent spin helix. Ever since then, numerous physicists are encouraged to an intense search for appropriate material compositions and qualified detection techniques.

A first verification of the persistent spin helix was reported in 2009 by transient spin-grating spectroscopy on GaAs² quantum wells [Kor09]. This method allows lifetime measurements of spin polarization waves and was used to demonstrate the expected suppression of spin relaxation for a certain wave vector. In the following years, other techniques like time- and spatially resolved Kerr microscopy [Wal12a] as well as photocurrent experiments [Koh12] contributed to the revelation of the persistent spin helix state and promoted a further understanding of this interesting phenomenon.

The motivation for this work was to verify the persistent spin helix based on a whole new characteristic, which was not exploited so far. Besides long spin lifetimes, a spin helix structure of a (001)-grown quantum well system is predicted to feature a spin splitting in the conduction band, which is highly anisotropic with a Fermi contour consisting of two shifted circles [Ber06]. A perfect tool to detect the spin splitting in a semiconductor nanostructure is inelastic light scattering. Early publications by A. Pinczuk [Pin71, Pin80] and G. Abstreiter [Abs79] established this technique, also known as electronic Raman scattering, as a standard method for an examination of the band structure of a semiconductor. An intense overview with fundamentals of inelastic light scattering can be found in Ref. [Sch06], where experimental results of semiconductor nanostructures are accompanied with theoretical and phenomenological descriptions. During the 90ths, various studies with GaAs quantum wells focused on the investigation of the spin splitting in the conduction band and revealed a small anisotropy concerning different crystal directions [Jus92, Ric93, Jus95, Ric96]. This anisotropy stems from an interplay between Rashba and Dresselhaus spin-orbit fields. With the theoretical proposals about the persistent spin helix [Sch03, Ber06] and the subsequent experimental search for appropriate verification techniques [Kor09, Wal12a, Koh12], an investigation of the spin splitting became attractive again, since a maximum anisotropy, which is only present for balanced spin-orbit fields, could not be observed so far.

The fabrication of a heterostructure with a two-dimensional electron system (2DES) characterized by equal Rashba and Dresselhaus fields is a very challenging task, even in times with excellent crystal purities achieved by molecular beam epitaxy. A sample growth with the desired ratio requires a difficult fine tuning

²GaAs: gallium arsenide

of sample parameters and involves quite often extensive procedures with numerous repetitions. During the last couple of years, gallium arsenide emerged as a suitable host material for a 2DES with a realized persistent spin helix state. In the main part of this work, we will consider two GaAs-based samples, while both feature a ratio between Rashba and Dresselhaus field quite close to one. Here, we could verify the persistent spin helix for the first time by means of the spin splitting detected with inelastic light scattering. Furthermore, we could demonstrate that an inversion of the Rashba field causes an interchange of anisotropic behavior concerning the crystal directions and leads to an inversed persistent spin helix state.

This work is not arranged with a categorical separation between theory and experimental results, each chapter rather provides the required background for the conducted measurements at its beginning. The main organization is as follows: Chapter 2, which comprises a basic overview, starts with an introduction of the investigated semiconductor material and elucidates the impact of a reduction to a two-dimensional electron system. Within the next few pages, characteristic properties and fundamental parameters of all samples used in this work will be presented. As already addressed above, the Rashba field may be tuned by means of an external electric field. A fabrication process for an electric gate on a sample is depicted at this point, while experimental results are shown later on. The chapter is then closed by the phenomenological introduction of inelastic light scattering and the description of the experimental setup used for this work.

In the first part of chapter 3, we elaborate on the electronic elementary excitations and discuss all key aspects of inelastic light scattering in a 2DES. Here, single-particle as well as collective excitations are introduced and the significance of a resonant intermediate state in the valence band for this measurement technique is emphasized. Afterwards we consider the scattering cross section, which directly leads to selection rules for the observation of electronic excitations. This first part is mainly based on corresponding chapters in Ref. [Sch06], but contains some deviations especially adapted for this work. In the second part of this chapter, we try to intensify the previously gained knowledge by means of experimental results on intersubband transitions in two different samples. This should contribute to a better understanding of elementary excitations and bridge the gap between measured spectra and theoretical background.

In chapter 4, spin-orbit coupling is introduced with a detailed depiction of spin splitting induced by Rashba and Dresselhaus fields. The special situation with a balanced ratio of coupling constants and an emerging persistent spin helix state is described subsequently, accompanied with the latest research results on this topic. From this point on, only intrasubband excitations with a transferred wave vector are regarded, since they provide a direct access to the spin splitting in the conduction band. In the following, we verify the persistent spin helix in two different samples and elucidate the impact of an external electric field on our experimental spectra. All measurements are vindicated by a consideration about the scattering

amplitude, which is generally introduced in chapter 3 and successively adjusted for each new experimental condition.

Besides a creation of excitations, which is known as Stokes process, inelastic light scattering may also probe an annihilation of already existing excitations. This effect is investigated in chapter 5, where the anti-Stokes component of measured spectra is depicted. The particular spectral shape of the signal allows some conclusions about the actual electron temperature during the measurement and reflects the Fermi-Dirac distribution of the 2DES.

In chapter 6, an impact of an external magnetic field perpendicular to the quantum well plane is discussed. It starts with a phenomenological overview of Landau quantization and the corresponding cyclotron resonance. The following experimental results reveal a smooth transition from a 2DES towards a Landau quantized system and represent an appropriate method to determine the effective electron mass. At very high magnetic fields, the fundamental behavior of Landau levels is depicted and characteristic properties like an oscillation of Fermi energy can be observed.

Afterwards, this work is closed with a final conclusion and a brief motivation for future experiments in chapter 7.

Chapter 2

Basics

The band structure of a crystalline semiconductor plays a central role in physical concepts, as it describes various fundamental properties like the effective mass of electrons and holes or optical emission and absorption. A well established tool to investigate the band structure is inelastic light scattering, since it allows the creation and annihilation of electronic excitations in the semiconductor. In this chapter, we will introduce the basic properties of the used material and discuss first techniques to characterize the investigated samples. Later on, we will elucidate the required background of inelastic light scattering and depict the experimental setup, whereby all presented measurements are carried out.

2.1 The material GaAs

All samples investigated in this work are based on gallium arsenide (GaAs), the most prominent representative of the III-V compound semiconductors. The crystal structure of GaAs is formed by covalent bonds arranged in a tetrahedral symmetry, as depicted in Fig. 2.1. Two interpenetrating face centered cubic (fcc) lattices, which are displaced by one quarter of the cubic space diagonal, coalesce to a zinc blende structure [Dre55]. This cubic lattice structure is described by the space group symmetry T_d^2 , which corresponds to a point group T_d of the lattice sites. T_d contains in total 24 symmetry operations and characterizes the symmetry of the regular tetrahedron. Figure 2.2 shows the first Brillouin zone in the reciprocal space together with some high symmetry points.

GaAs belongs to the direct gap semiconductors with both extrema of the band structure located in the center of the Brillouin zone. The energetic gap between the conduction and the valence band at this Γ -point is theoretically 1.519 eV for $T=0$ K. Since an exact calculation of the band structure entails a very complex theoretical treatment, the energy bands can be estimated and understood in simplified models as, e. g., the tight-binding picture. In this approximation, the many-body problem of the electron lattice interaction is reduced to a model of isolated atoms at each lattice site. The wave function of the neighboring atoms

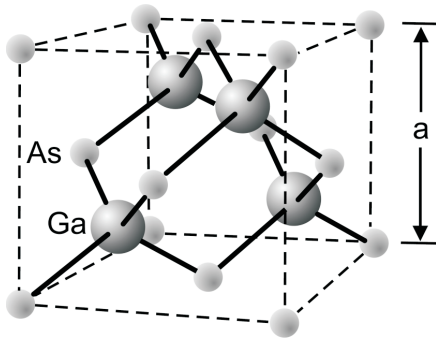


Figure 2.1: Crystal structure of gallium arsenide. Taken from [Sch06].

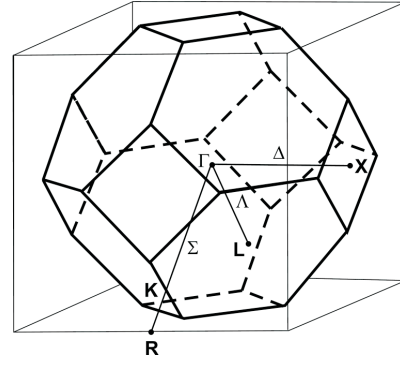


Figure 2.2: First Brillouin zone of a fcc lattice. Taken from [Sch06].

overlap and the eight electrons per unit cell, which contribute to the bonding, form new orbitals through sp^3 hybridization. Divided into a bonding and an anti-bonding type, these emerged orbitals broaden into bands due to the large number of unit cells in the crystal. The bonding orbitals constitute the valence band, where two electrons occupy the energetically lowest s orbital (angular momentum $l = 0$) and six electrons the three remaining p orbitals ($l = 1$). In contrast, the conduction band is formed by unoccupied antibonding orbitals, while the lowest s band, which is responsible for the size of the bandgap, features a two-fold spin degeneracy ($s = \pm 1/2$). Taking the spin-orbit interaction (SOI) into account, the six-fold degenerate p-like valence band splits into a four-fold degenerate band with Γ_8 symmetry (total angular momentum³ $j = 3/2$) and a two-fold degenerate band with Γ_7 symmetry ($j = 1/2$). The latter is the so called split-off band (SO) and is energetically lowered compared to the Γ_8 band with its heavy hole (HH) and light hole (LH) character (see Fig. 2.3). Since these states have different effective masses, the Γ_8 band is split up for finite wave vectors $k \neq 0$. The remaining spin degeneracy is lifted by the lack of inversion symmetry, which is distinctive for crystals with T_d symmetry or lower. This is known as Dresselhaus effect [Dre55] and will be depicted in more detail in Chap. 4.

In order to obtain a more profound description of the band structure (see Fig. 2.4), one has to solve the one-electron Schrödinger equation for electrons moving in a periodic potential $V(\mathbf{r})$:

$$\left[\frac{p^2}{2m_0} + V(\mathbf{r}) + \frac{\hbar}{4m_0^2c^2}(\boldsymbol{\sigma} \times \nabla V)\mathbf{p} \right] \psi(\mathbf{r}) = E\psi(\mathbf{r}) \quad (2.1)$$

The free electron mass is represented by m_0 and the term containing the vector $\boldsymbol{\sigma}$ of the Pauli spin matrices accounts for the SOI. Solutions of the equation are Bloch waves of the form

$$\psi_{n\mathbf{k}}(\mathbf{r}) = u_{n\mathbf{k}}(\mathbf{r})e^{i\mathbf{k}\mathbf{r}}, \quad (2.2)$$

³total angular momentum $\mathbf{j}=\mathbf{l}+\mathbf{s}$

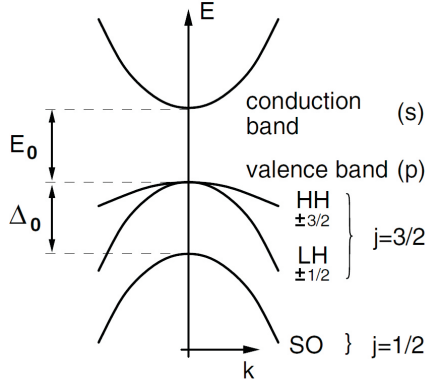


Figure 2.3: Sketch of the band structure of GaAs close to the Γ -point. Qualitative results according to effective mass approximation. Taken from [Win03].

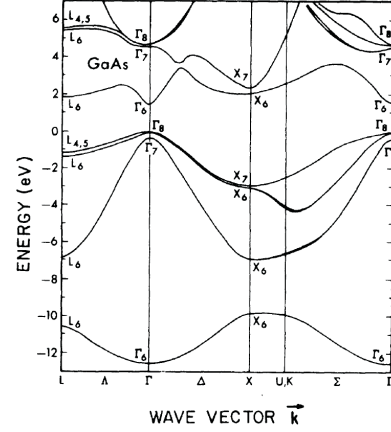


Figure 2.4: Band structure of bulk GaAs. Calculated with a nonlocal pseudopotential method. Taken from [Che76].

with the plane wave $e^{i\mathbf{k}\cdot\mathbf{r}}$ and the periodic function $u_{n\mathbf{k}}(\mathbf{r})$ of the crystal lattice [Ash13]. In many cases, a consideration of the band structure in the vicinity of the high-symmetry point k_0 (also known as Γ -point) is sufficient for the interpretation of experimental results. An appropriate approach for this situation is provided by the so called $k \cdot p$ method, where the Bloch ansatz yields a separation of the Schrödinger equation into a k -independent and a k -dependent term, which is treated as a perturbation. Hence, the electronic band structure can now be calculated for small wave vectors by means of perturbation theory. After a model proposed by Kane, an effective calculation is usually ensured by taking only the bands $\Gamma_7(2)$, $\Gamma_8(4)$ and $\Gamma_6(2)$ into account [Kan57]. Considering these eight bands⁴ and treating remote bands as a perturbation, the Hamiltonian results in an 8×8 matrix within the so called 8-band $k \cdot p$ model. The calculation may be extended by fully regarding two additional remote bands⁵. A detailed description of this extended Kane model and other theoretical approaches, like the effective mass approximation, can be found in Ref. [Win03].

2.2 Properties of GaAs-based quantum wells

The nearly defect-free growth of complex heterostructures with steadily improving features is a challenging task in nowadays physics research. These rising demands can be met by modern growth techniques like the MBE (molecular beam epitaxy) method, which allows the production of structures within an accuracy of single atomic layers. In this work, only heterostructures with compounds of GaAs and

⁴for lifted spin degeneracy

⁵the Γ_7 and Γ_8 conduction bands

AlGaAs are investigated⁶. Replacing a fraction x of Ga atoms with Al atoms leads to the ternary alloy semiconductor $\text{Al}_x\text{Ga}_{1-x}\text{As}$ with a different lattice constant a [Ada85]:

$$a = 5.6533 + 0.0078 \cdot x \text{ [\AA]} \quad (2.3)$$

However, this lattice constant differs only slightly from the one of GaAs and provides therefore nearly perfect conditions for a strain free growth of GaAs/AlGaAs heterostructures. The band gap of the alloy may also be tuned by the fraction x and is given for low temperatures by

$$E_g^{\text{AlGaAs}} = 1.519 + 1.155 \cdot x + 0.37 \cdot x^2 \text{ [eV]} , \quad (2.4)$$

whereas the gap remains direct only for an aluminum concentration below 45% [Lev99]. Above this value, the conduction band minimum moves to the X-point, yielding an indirect band gap. But this is not of further interest here, since all investigated samples in this work feature a direct band gap at the Γ -point.

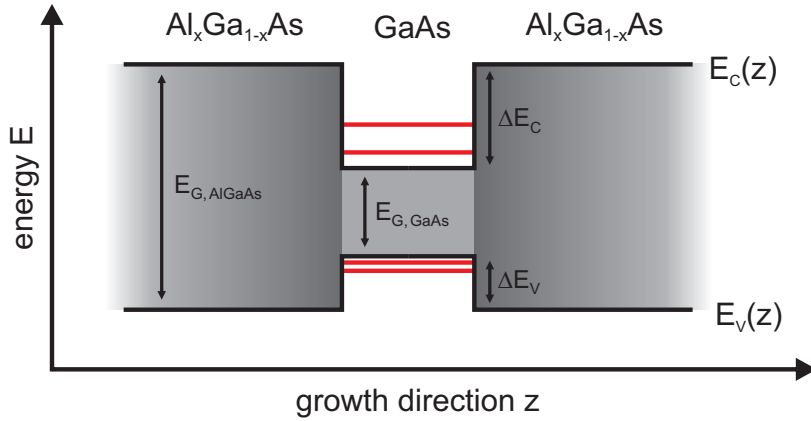


Figure 2.5: *Band-edge profile of a GaAs/AlGaAs heterostructure.*

A schematic picture of an AlGaAs/GaAs/AlGaAs heterostructure is illustrated in Fig. 2.5. The material with a comparatively low band gap (here: GaAs) is surrounded by a material with a larger band gap (AlGaAs), designating a type-I heterostructure. Such a composition is well described by the textbook example of a single particle in a box-like potential. Again, we start with the one-electron Schrödinger equation

$$\left[\frac{\hbar^2 k^2}{2m^*} + V(\mathbf{r}) \right] \psi_k(\mathbf{r}) = E_k \psi_k(\mathbf{r}) , \quad (2.5)$$

where $V(\mathbf{r})$ is the rectangular potential of the heterostructure and m^* is the effective mass of the electrons and holes, respectively. Since the movement of

⁶In the critical region of interest. Actually, the sample contains more components.

the particles is limited to the (x, y) -plane, the energy of the electron and hole states are quantized along the z direction. However, the emergence⁷ as well as the distance of such discretized subbands strongly depends on the layer thickness of the embedded semiconductor. If the quantum well (qw) has only a small extension along the growth direction, the system is called quasi⁸ two-dimensional and the confinement energy is then given by

$$E_{n,k} = E_{n,k_z} + E_{k_{\parallel}} = \frac{\hbar^2}{2m^*} \left(\frac{n\pi}{d} \right)^2 + \frac{\hbar^2 k_{\parallel}^2}{2m^*}, \quad (2.6)$$

with the subband index n , the in-plane component $k_{\parallel} = (k_x, k_y, 0)$ and the quantum well width d . The effective mass m^* , which reflects the curvature of the subbands in the center of the Brillouin zone, is often assumed to be isotropic and with parabolic behavior. Strictly speaking, the parabolic approximation is valid only for electronic and not for hole states. Therefore, a nearly constant density of states ($n_{2D}(E)$) within a subband is solely given for the conduction bands:

$$n_{2D}(E) = \frac{m^*}{2\pi\hbar^2} \quad (2.7)$$

A standard model for calculating the electronic ground state of nanostructures is the envelope function approximation (EFA, [Bas81]), which is well appropriate for compositions with the same band extrema. The calculation is derived from the Bloch ansatz (see Eq. (2.2)), with the fast oscillating Bloch function and the slowly varying plane wave. Based on the $k \cdot p$ method, the wave function is expanded around $k = 0$ for each layer and a consistent periodicity for the Bloch function across the heterostructure is assumed. Consequently, the wave function is a sum of products and reads

$$\psi(\mathbf{r}) = \sum_l f_l^{A,B}(\mathbf{r}) u_{l,0}(\mathbf{r}), \quad (2.8)$$

where $u_{l,0}$ is the fast oscillating function, implying the periodicity of the bulk crystals. Moreover, the slowly oscillating envelope functions f_l have to satisfy the boundary conditions at the interfaces ($f^A(z_0) = f^B(z_0)$). Because the z -axis is defined as the growth direction in all investigated samples, the (x, y) -plane appears to be invariant for lateral translations and the envelope function can be factorized as

$$f_l^{A,B}(\mathbf{r}_{\parallel}, z) = \frac{1}{\sqrt{S}} e^{i\mathbf{k}_{\parallel} \mathbf{r}_{\parallel}} \chi_l^{A,B}(z), \quad (2.9)$$

with the sample area S and the two-component vectors \mathbf{k}_{\parallel} and \mathbf{r}_{\parallel} in the (x, y) -plane.

The calculation of the band structure of vertical nanostructures is now applicable by means of the previously introduced 8-band $k \cdot p$ model. Since the states are

⁷Quantum mechanical effects occur if the layer thickness $d \leq \lambda_{dB}$ (de Broglie wavelength). For all samples in this work: $d \ll \lambda_{dB}$

⁸Quasi, because the qw has actually a finite extension along the growth direction. However, this will be neglected in the following.

quantized along the growth direction, k_z is replaced by $-i\partial/\partial z$ in the $H_{8\times 8}$ Hamiltonian. Furthermore, an additional potential $V_{ext}(z)$, representing the square well potential of the conduction and the valence band, respectively, has to be included. The resulting Schrödinger equation

$$\left[H_{8\times 8}(\mathbf{k}_{\parallel}, -i\frac{\partial}{\partial z}) + V_{ext}(z) \right] \psi(\mathbf{r}) = \epsilon_n(\mathbf{k}_{\parallel}) \psi(\mathbf{r}) \quad (2.10)$$

reflects a system with a set of eight coupled differential equations, which especially affect the character of the Γ_8 valence band:

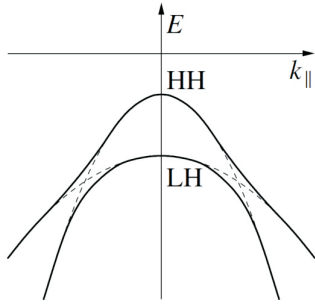


Figure 2.6: *Schematic sketch of a HH-LH anticrossing. Taken from [Win03].*

The fourfold degeneracy at the Γ -point is lifted by the size quantization of the 2D system and the states along the growth direction z can be divided into light holes, with a small effective mass, and heavy holes, with a large effective mass. However, this relation is reversed for a motion in the quantum well plane, which would lead to a crossing of HH and LH states for $k \gg 0$. After all, the coupling in the Hamiltonian yields a mixing of the states and causes therefore the so called HH-LH anticrossing, a repulsive behavior of the bands combined with an exchange of light-hole and heavy-hole character [Win03].

So far, our considerations depend only on single particles, while many body problems were neglected. In order to satisfy interaction effects of charge carriers among each other or with ionized donors, as given by a modulation doping, the band structure may be calculated by solving the effective single-particle Schrödinger equation and the Poisson equation self-consistently [Sch06]. The Poisson equation for electrostatic matters is given by

$$\Delta\Phi(\mathbf{r}) = -\frac{\rho(\mathbf{r})}{\epsilon}, \quad (2.11)$$

where $\Phi(\mathbf{r})$ is the electrostatic potential, $\rho(\mathbf{r})$ the distribution of the carrier density and ϵ the absolute permittivity of the medium [Ash13]. A very sophisticated simulation program⁹ to meet these requirements is nextnano³, which approaches the issue of the modulation doping by a Hartree potential. Detailed information about the structure of nextnano³ may be found in Ref. [Zib07], and for some applications of these band structure calculations it will be referred to [Hir12].

⁹A similar program is nextnano⁺⁺, which differs only in some aspects from nextnano³. For more information, see [Zib07, Hir12].

Modulation doping

The subband states in a quantum well structure are occupied up to the Fermi energy E_F , which is located midway between the valence and the conduction band for an undoped system (at $T = 0$). By intentionally introducing impurities, the number of charge carriers (electrons or holes) and therefore the location of the Fermi energy may be altered. Usually III-V semiconductors like GaAs/AlGaAs are doped with silicon (Si; n-doped) or carbon (C; p-doped), resulting in a two-dimensional electron system (2DES) and a two-dimensional hole system¹⁰ (2DHS), respectively. A common technique to improve electrical properties of nanostructures, such as the mobility of carriers, is modulation doping [Dru81]. In this context, a very thin layer of dopant atoms is usually denoted as δ -doping. In a modulation doped system, impurity atoms are spatially separated from the quantum well by an undoped spacer layer. The carriers provided by the dopant atoms are dragged into the energetically favored quantum well, entailing a distinct reduction of scattering between the carriers and the ionized atoms. Additionally, the electric field ($E_z = -\nabla\Phi$), established by the spatial separation of the carriers, yields a distortion of the band curvature in the barrier as well as in the quantum well. A further impact of the built-in electric field becomes apparent by considering a single-sided doped (ssd) heterostructure: The electron wave function is shifted asymmetrically towards the doping layer, causing a partial penetration into the barrier material and therefore a reduction of the total mobility. This disadvantage can be avoided by introducing a second doping on the opposite side of the quantum well (dsd: double-sided doped), centering the wave function and hence, reducing the scattering at the interfaces. For a further enhancement of the electron mobility, novel growth schemes with additional doping layers may be utilized [Uma09], as discussed in the next section for sample D.

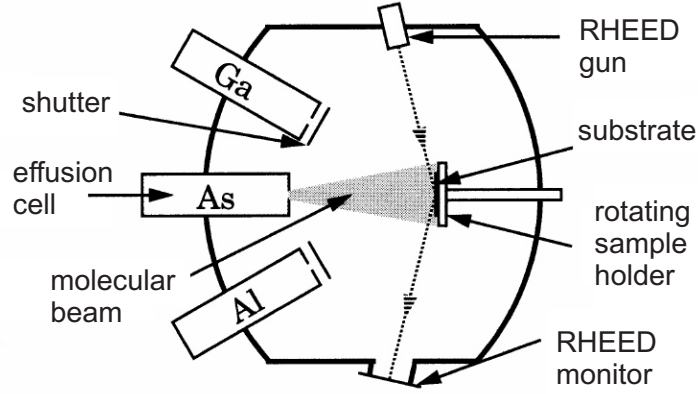
2.3 Investigated samples

All investigated samples in this work are grown by molecular beam epitaxy and designed to fulfill certain purposes. To meet the delicate requirements of these sample structures (see, e.g., sample A and B), not only an accurate control of growth parameters is indispensable, but also a sophisticated optimization and repetition in terms of layer composition and growth process may become necessary. The MBE technique is able to produce such samples with a remarkably high crystal purity in combination with excellent optical properties, which is crucial for experiments on inelastic light scattering.

Epitaxial growth of heterostructures is realized by a radiation of the substrate with molecular beams from heated effusion cells (see Fig. 2.7). The released amount of extra-clean material deposits on the heated GaAs substrate, which is mounted on a rotating sample holder to provide a uniform layer thickness. To avoid any incorporation of random defect atoms, the growth process is enclosed by

¹⁰In this work, only 2DES are discussed.

Figure 2.7: *Schematic setup of a MBE chamber: The evaporated material of the effusion cells is deposited on the substrate, which is mounted on a rotating sample holder to provide a uniform growth process. Taken from [Dav98].*



an ultra-high vacuum chamber supported by a cryogenic cooling shield to freeze out any impurity atoms left. Mechanical shutters in front of the effusion cells ensure the right procedure of epitaxial growth and the performance is simultaneously controlled by RHEED¹¹ measurements. As a result, the MBE technique is capable of producing samples with an ideal accuracy in the range of single atomic layers and provides therefore the perfect tool to grow ambitious heterostructures.

2.3.1 Sample structure

The whole work is based upon n-doped GaAs/AlGaAs quantum well structures, grown either on a (001)- or a (110)-GaAs substrate. An overview together with some important parameters is given in Tab. 2.1.

sample name	waver number	growth axis	width qw (nm)	doping style	density N_s (10^{11} cm^{-2})	mobility μ ($10^6 \text{ cm}^2/\text{Vs}$)
A	D110831A	(001)	12	dsd	5.0	0.22
B	C130117A	(001)	12	ssd	5.9	0.84
C	7-5-96.1	(001)	25	ssd	2.1	3.37
D	D081205A	(110)	30	2dsd	3.4	5.10
B* (gated)	C130117A	(001)	12	ssd		

Table 2.1: *Investigated samples: The values for the carrier density and the mobility in the 2DES were obtained by magneto transport measurements.*

The presented values for the electron density and the mobility were determined shortly after the growth process by magneto transport measurements at $T = 4.2 \text{ K}$. However, these values may vary to some extent from the one obtained during the Raman measurements. Such an inconsistency may easily be explained by different experimental conditions and will be addressed again throughout the next chapters. In the following, the particular structure of the samples as well as their purpose concerning this work will be elucidated in more detail:

¹¹RHEED: reflection high energy electron diffraction

Sample A

Sample A was manufactured in the group of Prof. Dr. W. Wegscheider at the ETH Zurich and was designed to satisfy certain conditions in terms of spin-orbit coupling [Wal12a]. The aim was to achieve a balanced ratio between both contributions of the spin-orbit field, yielding a special symmetry called the persistent spin helix. The formation of this interesting phenomenon and the impact on Raman scattering will be clarified in detail in Chap. 4. At this point, we will focus mainly on the composition and the basic parameters of the sample.

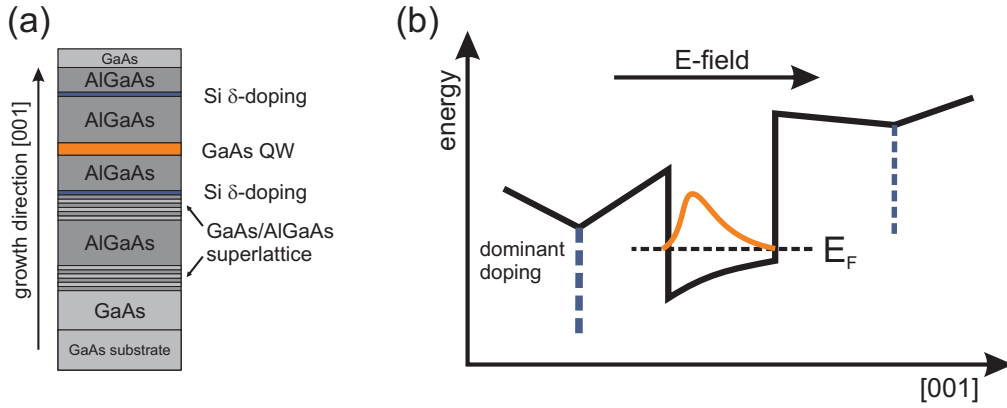


Figure 2.8: *Sample A: (a) Layer composition, not to scale. (b) Asymmetric band profile with a built-in electric field parallel to the growth direction (schematic picture).*

The sample is grown on a (001)-GaAs substrate and features a 12 nm-wide single quantum well. A schematic picture with the layer composition and the corresponding band profile is shown in Fig. 2.8. Two sequences with GaAs/AlGaAs superlattices ensure the incorporation of impurity atoms in deeper layers far away from the optical region of interest. Although the structure contains two Si δ -dopings, the band edge profile is not symmetric due to different doping concentrations. The doping layer on the substrate side dominates the curvature and causes an internal electric field, which pulls the wave function towards the deeper situated interface. A comparatively low electron mobility of $\mu = 2.2 \times 10^5 \text{ cm}^2/\text{Vs}$ can be explained by the penetration of the wave function into the barrier material and additionally by the location of this dominant doping layer: The epitaxial growth of doping atoms previous to the quantum well may cause a segregation of donor atoms towards the well region, giving rise to an enhanced scattering and hence a low electron mobility in the 2DES [Liu93].

Sample B and B*

This sample was grown by Dieter Schuh in the group of Prof. Dr. D. Bougeard (University of Regensburg) and was basically intended to provide similar con-

ditions concerning spin-orbit fields as sample A. Therefore, again a 12 nm-wide GaAs quantum well, surrounded by AlGaAs barriers, is grown on a (001)-oriented substrate (see Fig. 2.9). The significant difference between these two samples is the reduction to a single δ -doping, located between the quantum well and the surface. This doping layer establishes an electric field pointing towards the substrate, causing a kind of mirrored band edge profile with respect to sample A. The nominal electron density of $N_s = 5.0 \times 10^{11} \text{ cm}^{-2}$ is just slightly higher than the one for the dsd quantum well. However, the mobility is increased by almost a factor of 4, probably favored by the single-sided doping. This difference will play a significant role in Chap. 6, where the cyclotron motion in an external magnetic field is of great importance.

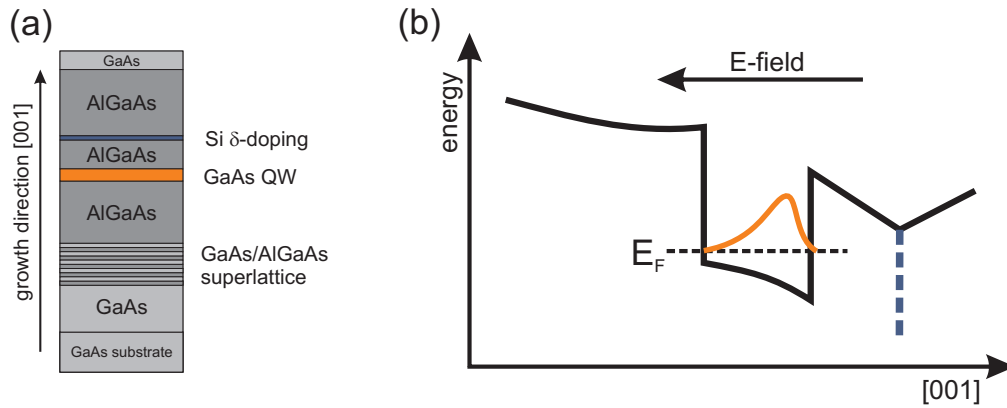


Figure 2.9: *Sample B: (a) Layer composition, not to scale. (b) Asymmetric band profile with a built-in electric field antiparallel to the growth direction (schematic picture).*

Sample B* stems from the same wafer as sample B, but was provided with a semi-transparent top gate to investigate the influence of an external electric field on the band structure. A detailed description of the gating process is given at the end of this section, while the experimental results are presented in Chap. 3.2.2 and Chap. 4.2.6.

Sample C

This heterostructure is also grown on a (001)-substrate, but contains a single qw with a well width of 25 nm. Since the doping layer is integrated in the barrier on the surface side of the 2DES, the band edge profile can be pictured similar to sample B. The larger quantum well causes a distinct reduction of the spacing between the subbands in the electron gas. Therefore, this sample is employed to clarify the fundamental concepts of intersubband excitations in a quantum well structure and to elaborate on the distinctions between different well sizes, which is discussed in Chap. 3.2.

Sample D

Modern growth schemes, like the one proposed in [Uma09], paved the way to extremely high electron mobilities in semiconductor heterostructures. A crucial impact is given by the shape of the band edge profile, which is depicted for sample D in Fig. 2.10. This heterostructure features a 30 nm-wide quantum well, oriented in (110)-direction. Four symmetrically arranged doping layers cause the electron wave function to center in the middle of the quantum well, minimizing the penetration into the low-mobility material and mostly preventing the scattering due to interface roughness. A further feature of the depicted structure is the distribution of the doping amount: The flat band profile within the barriers is realized by a fairly high sheet density of silicon in the far-off dopings, while the doping layers close to the quantum well are responsible for the carrier concentration in the 2DES. A high mobility is additionally facilitated by the lower growth temperature compared to (001)-structures, preventing the doping atoms to segregate into the quantum well region [Bel08]. However, not the mobility, but the vanishing internal electric field, caused by the symmetric doping arrangement, is of great interest for this work. To this end, Chap. 4.3 is dedicated to reveal the effect on the band structure.

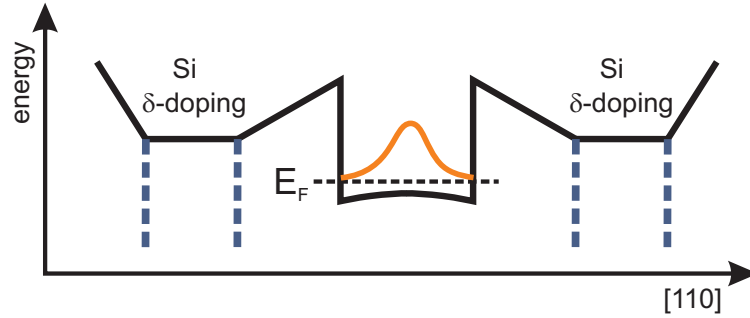


Figure 2.10: *Sample D: Symmetric band profile with vanishing electric field due to four symmetric doping layers (schematic picture).*

2.3.2 First characterization: PL and PLE

The size of the band gap is an important quantity in the spectroscopy of semiconductors, providing a first approximation how much energy is needed to lift an electron from the valence band to the conduction band. An experimental approach is given by photoluminescence (PL) spectroscopy, where electron-hole pairs are generated by an excitation with a laser energy above the band gap (see Fig. 2.11). Due to intrasubband scattering events, the generated charge carriers relax on a very fast timescale towards the band extrema, where they recombine irradiantly under the conservation of energy and momentum. The excitation and recombination processes in the $E(k)$ diagram are assumed to be vertical, since the k -vector of photons is negligible. Considering doped systems, transitions from

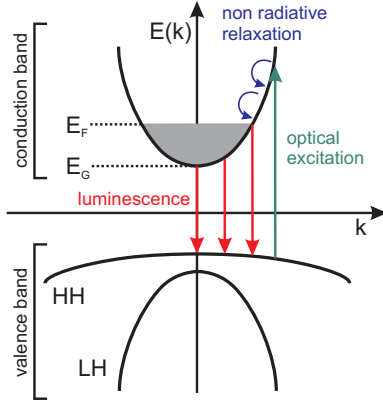


Figure 2.11: Schematic picture of the photoluminescence in k -space.

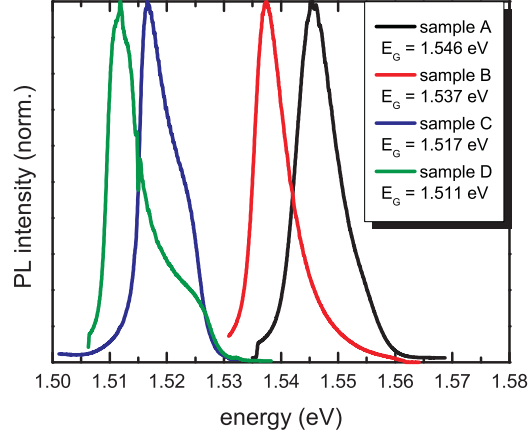


Figure 2.12: PL spectra for all investigated samples.

$k = 0$ to $k = k_F$ (Fermi wave vector) contribute to photoluminescence, resulting in a typical shark-fin like shape of the spectra (see, e.g., sample C in Fig. 2.12). Because the heavy hole states in the valence band feature a large effective mass, the curvature of this band is very flat and hence, the dispersion of the conduction band mainly determines the spectral width of a PL trace.

The measured photoluminescence of each sample at $T = 5.5$ K is plotted in Fig. 2.12 and the extracted values for the size of the band gap can be found in the inset. A first tendency is rapidly perceived, saying a larger quantum well width results in a lower band gap energy. Comparing sample A and B, which contain nominally the same qw width of 12 nm, one would expect a very similar transition energy in the first place. The given discrepancy may be explained by different band bendings or the variation of the actual quantum well size throughout the wafer, manifesting itself in a huge deviation up to ≈ 4 meV in the transition energy for different samples of the same wafer. In consequence, all measurements were carried out on the same samples to provide a comparability of results¹². A further origin of the redshift in sample B may be attributed to the band gap renormalization (BGR), which denotes a reduction of the gap size scaling with increasing carrier density and decreasing quantum well width [Kle85, DS90, Haa92]. Assuming a similar qw width, a lower transition energy of sample B would therefore be governed by the higher carrier density in the 2DES. However, this effect is probably very small since both carrier densities are of comparable magnitude. A vague indication of the carrier density is already provided by the linewidth $\Delta E = E_F - E_G$ of the PL trace [Gri12a], but a further approximation is spared here for the following reasons: Although the shark-fin shape is clearly visible for sample C and D, the Fermi edge is hardly recognizable for the samples with a higher carrier density (sample A and B). The contrast may be increased by choosing a logarithmic scale (not shown), however, this estimation would still contain

¹²Sample B* is from the same wafer as sample B, but a different fraction. Otherwise the results of sample B would not be reproducible. Therefore, a slight deviation of these two samples in the main parameters may be present.

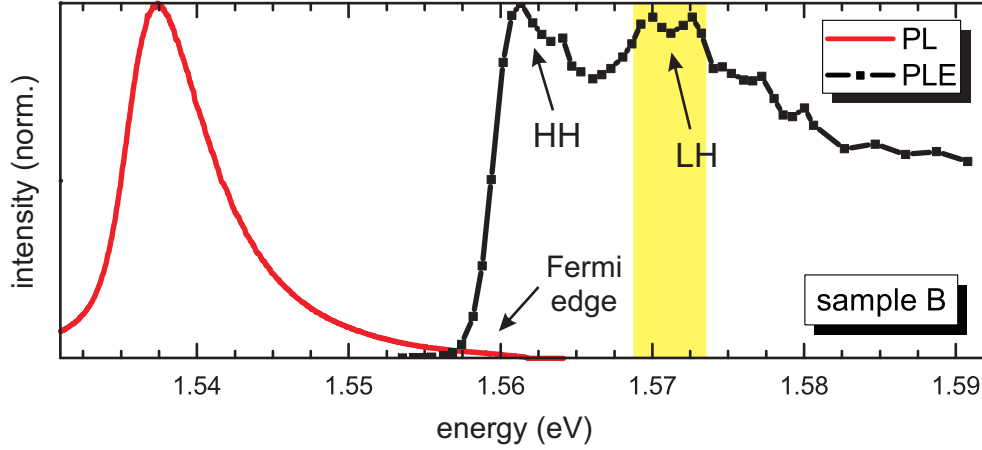


Figure 2.13: *PL and PLE measurement of sample B. The absorption of the 2DES starts in the vicinity of the Fermi edge. The yellow shaded region represents the mainly used excitation energy for measurements on intrasubband transitions.*

a huge inaccuracy. Furthermore, the carrier density of the 2DES can be extracted directly from the results on Raman scattering in this work, yielding a more precise approach of the actual value during the measurements.

So far we only considered the fundamental band gap and the impact of the Fermi energy, but for inelastic light scattering in a 2DES, also the subband structure of the valence band plays an important role due to resonance effects. A common way to probe the absorption of a quantum well system is the photoluminescence excitation spectroscopy (PLE), where PL traces are measured for different excitation energies. The amplitude of the single spectra can be extracted and provides an indication of the absorption in the quantum well. Figure 2.13 exemplarily shows the PLE spectrum of sample B together with its photoluminescence. An absorption of light does not start until the laser energy overcomes the band gap as well as the Fermi energy. For higher excitation wavelengths, the quantum well remains transparent. The absorption line in the vicinity of the Fermi edge can be attributed to the transition from the HH band, while the resonance with the LH states is blue shifted by ≈ 10 meV. Usually, Raman excitations aspire a resonant intermediate state. Hence, most measurements of this work, especially concerning intrasubband transitions, are carried out with an excitation energy in the yellow shaded region and exploit the resonance with the LH valence band.

2.3.3 Fabrication of an electrical gate

As we already discussed in this chapter, the band edge profile in the vicinity of the quantum well is mainly influenced by the electric field. The internal field is basically determined by the incorporation of the modulation doping, but now we introduce a way to apply an additional field by means of an external gate, which allows us to manipulate the total electric field strength of the 2DES to some degree.

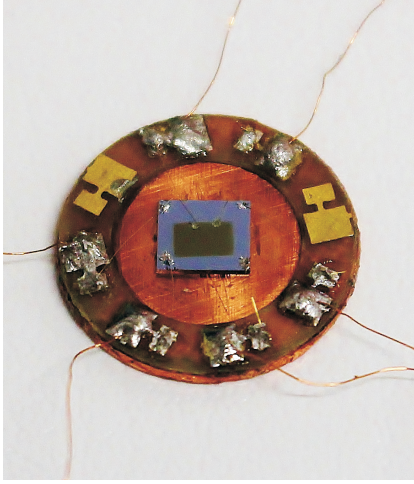


Figure 2.14: Sample with a semi-transparent top gate. Thin gold wires are used to connect the 2DES and the gate contact with the contact pads of the sample holder.

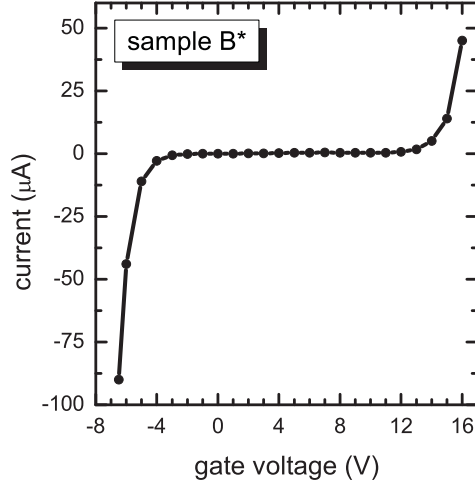


Figure 2.15: I - V characteristic of sample B^* with a typical diode like behavior. Setting a limit of $\pm 100 \mu\text{A}$, the gate voltage can be tuned between -6 V and $+16 \text{ V}$.

At the beginning of the fabrication process, the sample is cleaned by sonication in acetone, ensuring a deposit-free surface. Afterwards, a diamond tip scratcher is used to implement a small scratch in each corner of the surface, where a small amount of indium is deposited with a clean soldering rod. To conclude this step, the indium has to be alloyed into the crystal, building an electric contact between the drop at the surface and the 2DES. For that reason, the sample is enclosed in forming gas atmosphere and heated within 60 s to 350° , where it remains for additional 60 s.

After the sample is cooled down, it is equipped with an appropriate mask and mounted in the high vacuum evaporation chamber. For all-optical measurements like inelastic light scattering, the semi-transparency of the top gate is of crucial interest. Therefore, a nickel-chromium (NiCr) alloy is used, yielding a transmission of about 70% for a nominal 6 nm thick layer (see Fig. 2.14).

In the next step, the sample is glued by conductive silver to a previously prepared sample holder, where contact pads are equipped by enameled copper wires with plug-in IC pins. Finally, all alloyed contacts in the corners as well as the top gate, where tiny drops of conductive silver are used, are connected by thin gold wires to the contacts pads. The functionality of the contacts is subsequently checked by simple resistance measurements between each contact.

Typical values for sample B^* at room temperature were about 3-5 k Ω between contacts of the 2DES and about 50 k Ω between both top gate contacts. Figure 2.15 shows the determined I - V characteristic for sample B^* at liquid helium temperature. Since the shape of the curve has a diode-like behavior, the current was restricted to $\pm 100 \mu\text{A}$ in order to prevent the sample from suffering any damage. This limited the operating voltage of the gate to a range of -6 V to $+16 \text{ V}$.

2.4 Inelastic light scattering

The inelastic light scattering was experimentally invented by the Indian physicist Chandrasekhara Venkata Raman, who was awarded for his discovery in 1930 the Nobel price in physics. Ever since then, the so called Raman scattering is employed in wide fields of chemistry and physics as a non-destructive method to investigate fundamental excitations in materials. From a historical point of view, the Brillouin scattering, where acoustic phonons are excited, can be distinguished from the classical Raman scattering, where only optical phonons or internal vibrations of molecules contribute to the scattering [Sch06]. Nowadays, this technique is indispensable for the characterization of modern layered crystal structures as graphene [Fer06, Hey10] or MoS₂ [Lee10, Ple12]. But the application of Raman scattering is not limited to phonons in a medium. Electronic excitations of semiconductors, as depicted in this work, are also covered by this technique, which is often called inelastic light scattering in that context. This makes Raman scattering a timeless tool with various applications in the latest research fields.

2.4.1 General concept

The basic principle of Raman scattering can be understood in a simple picture as follows: An incoming photon with the energy $\hbar\omega_I$ and the momentum \mathbf{k}_I causes either a creation (Stokes process) or an annihilation (anti-Stokes process) of an elementary excitation with the energy $\hbar\omega$ and the momentum \mathbf{q} . According to the conservation law, the energy of the scattered photon is given by

$$\hbar\omega_S = \hbar\omega_I \pm \hbar\omega , \quad (2.12)$$

where the plus (minus) sign is for the anti-Stokes (Stokes) process. As a consequence, the scattered photon is shifted to higher and lower energies, respectively. Moreover, the conservation of momentum determines

$$\mathbf{k}_S = \mathbf{k}_I \pm \mathbf{q} , \quad (2.13)$$

with the same correlation of signs. A schematic picture of these scattering events is depicted in Fig. 2.16. The detection of the scattered photons yields important information about the energy and the momentum of the investigated excitations in the medium.

Figure 2.17 illustrates a typical Raman spectrum with an excitation energy of $\hbar\omega_I$. The elastically scattered light, which stems for instance from the sample surface, is visualized as the dominant contribution in the center of the spectrum. Since all measurements in this work are carried out at very low temperatures (≈ 5.5 K), there hardly exist any excitations in the semiconductor system and hence, only the Stokes process plays an important role. However, Chap. 5 is dedicated to discuss briefly the occurrence of the anti-Stokes component in the examined heterostructures.

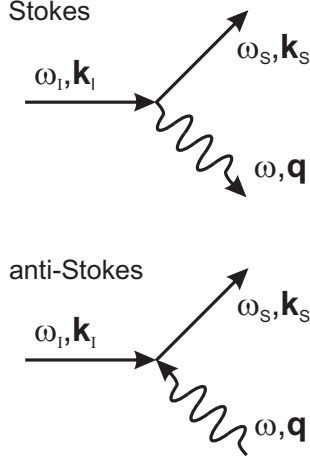


Figure 2.16: Schematic picture of the Stokes and the anti-Stokes process.

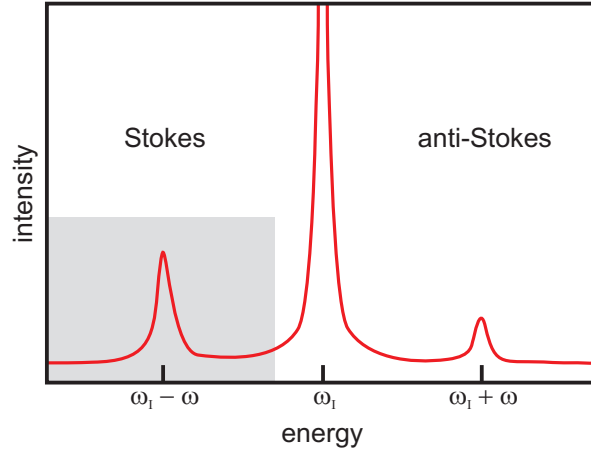


Figure 2.17: Schematic picture of a Raman spectrum. The Stokes process is shifted to lower, the anti-Stokes to higher energies.

In experimental spectra, the energy of elastically scattered light is usually set as the zero point and the Stokes component covers the positive side of the x -axis. This convention will be kept throughout the work. Furthermore it is mentioned that the Raman scattering amplitude is exceeded by the signal of the elastically scattered light by far.

One of the striking benefits of Raman scattering, and also a crucial element for this work, is the ability to transfer a particular wave vector \mathbf{q} to the excitation. An exact backscattering geometry, where the directions of incoming and scattered light are antiparallel and perpendicular to the sample surface, yields the maximum value for the transferred wave vector [Sch06]:

$$q_{max} = \frac{4\pi}{\lambda_I} \quad (2.14)$$

Here, the assumption of approximately equal incoming and scattered wavelengths ($\lambda_I \approx \lambda_S$) is thoroughly valid, considering the small energy of the excitation compared to the incident laser energy.

For quantum well structures, a further discussion on the momentum transfer is necessary: Since the translational symmetry is not conserved in the growth direction, the momentum can only be transferred in lateral directions of the 2DES. Consequently, the wave vector parallel to the quantum well plane may be adjusted continuously by

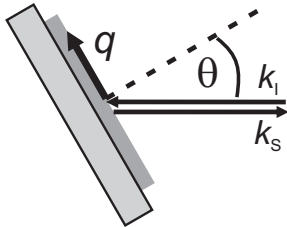


Figure 2.18: Backscattering geometry with a transferred wave vector \mathbf{q} .

$$q = \frac{4\pi}{\lambda_I} \sin(\theta) , \quad (2.15)$$

while an equal angle θ for incident and scattered light is assumed (see Fig. 2.18). Because such a configuration is used in numerous measurements of this work, the formula is of great interest and will be used throughout the following chapters.

2.4.2 Experimental setup

All experimental data presented in this work are obtained with a typical Raman setup, which allows photoluminescence and Raman measurements in backscattering geometry. A schematical picture of this setup is illustrated in Fig. 2.19.

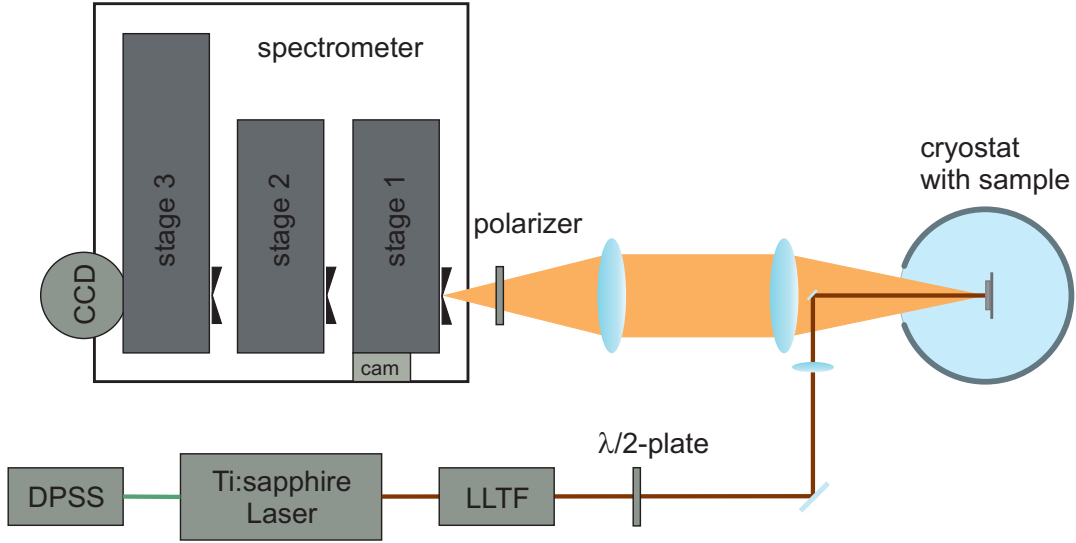


Figure 2.19: *Experimental setup of the Raman lab used in this work.*

The laser light is provided by a continuous wave (cw) titanium-sapphire laser (TiSa), which is pumped by a diode-pumped solid state laser (DPSS). Although the possible tuning range of the TiSa covers 620 to 1000 nm, all presented measurements were conducted with a wavelength between 730 and 820 nm. After the laser beam is emitted, it is guided into a laser line tunable filter (LLTF). This device is based on the Bragg filter technology and allows a laser line selection with a quite narrow bandwidth (FWHM ≈ 0.3 nm), enabling a detection of Raman excitations with energies as low as 0.3 meV. Before the beam is coupled into the cryostat, the polarization can be varied by a $\lambda/2$ plate. The linearly polarized laser light is then focused onto the sample with a spot size diameter of about $100 \mu\text{m}$ and a power density attenuated to about 80 W/cm^2 . Two sizable achromatic lenses are functionalized to gather and focus the scattered light into the triple stage Raman spectrometer. A polarizer in front of the entrance slit may select the requested polarization of the scattered light. The spectrometer consists of three individually adjustable stages, assembled to separate the elastically scattered laser light from the low-intensive Raman signal. For this purpose, the first two stages are utilized as a tunable bandpass¹³, while the third stage yields the

¹³For a fixed laser wavelength, the first two stages may be substituted by filter foils. However, a tunable bandpass is indispensable for a tunable laser system as used in this setup.

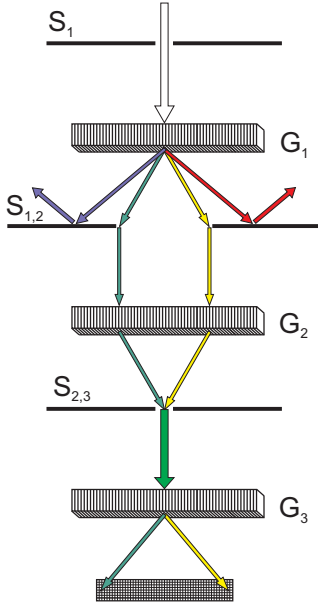


Figure 2.20: *Subtractive mode of the triple stage Raman spectrometer: The first two stages act as a variable band-pass to filter the interfering stray light from the Raman signal. The spectral resolution is afterwards gained by the grating in the third stage, projecting the scattered light on a CCD-chip which is read out by a computer.*

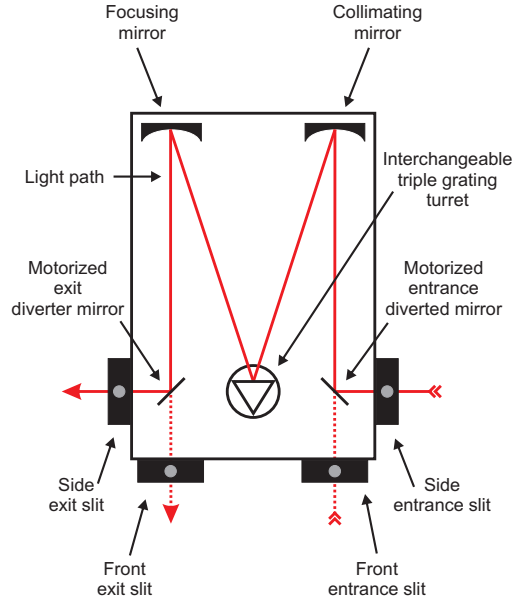


Figure 2.21: *Schematical composition of a single stage: The beam is guided through the entrance slit and mirrored onto a changeable grating, where the light is spectrally split and merged, respectively, before it is decoupled by the exit slit. Additional front slits allow the operation of assistant devices like video cameras or adjustment lasers.*

actual spectral resolution (see Fig. 2.20 and Fig. 2.21), which was about $34 \mu\text{eV}$ in all measurements. The spectra of the scattered light was finally detected by a liquid-nitrogen-cooled CCD¹⁴-chip and sent to a computer.

According to the aim of the measurement, two different cryostats could be integrated into the experimental setup: In the flow cryostat, depicted in Fig. 2.22, the sample is surrounded by helium gas, ensuring an ideal cooling efficiency of the 2DES. In fact, the temperature could be cooled down to liquid helium temperature ($T \leq 4.2 \text{ K}$), however, a slightly increased temperature of 5.5 K was constantly selected to prevent the light from scattering on occasionally appearing air bubbles in the liquid phase. The sample is here mounted on a rotatable sample holder, giving rise to a quasi continuously tunable wave-vector transfer to the 2DES. This configuration allows measurements with a tilt angle θ up to $\approx 60^\circ$, corresponding to $q_{\text{max}} \approx 13.8 \times 10^6 \text{ m}^{-1}$ for an excitation wavelength of 790 nm . Additionally, an aperture was used to restrict the inaccuracy of the scattering angle to $\pm 4^\circ$.

For measurements with an external magnetic field, the cryostat sketched in Fig. 2.23 was used. Herein, the sample was mounted on a coldfinger, which is coupled by a heat exchanger to the liquid helium. Although the nominal sample temperature displayed $\approx 4 \text{ K}$, the actual temperature of the 2DES was consid-

¹⁴CCD: charge-coupled device

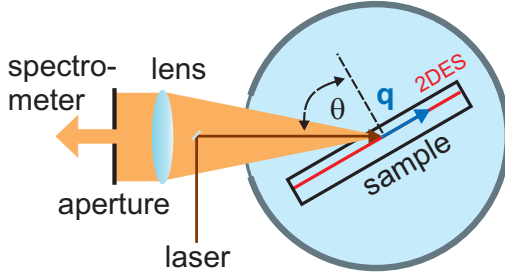


Figure 2.22: Top view of the flow cryostat: A rotatable sample holder enables a quasi continuously-tunable wave-vector transfer to the 2DES. The surrounding helium gas ensures a decent and constant cooling of the electrons in the quantum well.

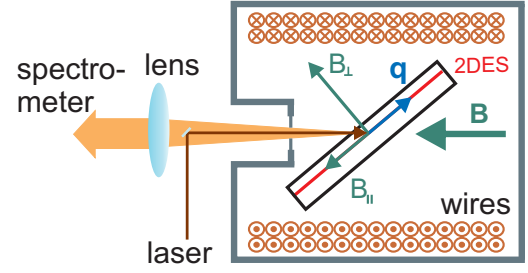


Figure 2.23: Top view of the magnetic field cryostat: The sample is mounted on a fixed coldfinger, providing a certain wave-vector transfer. The encasing solenoid establishes a magnetic field with a component parallel and perpendicular to the qw plane.

erably higher (up to ≈ 20 K) due to the weak cooling power of the system. To provide a certain wave vector in the quantum well plane, small attachments with a fixed slope could be incorporated to the sample holder. The magnetic field is provided by a superconducting solenoid, capable of field strengths up to 5 T. Since the sample is mounted in a certain tilt angle, the total magnetic field splits up into a component parallel and a component perpendicular to the quantum well plane. An additional restriction of the scattered light is not needed due to the low built-in aperture angle of this cryostat.

Chapter 3

GaAs/AlGaAs quantum wells: Fundamental concepts

3.1 Electronic elementary excitations

Inelastic light scattering is a powerful tool to investigate the electronic elementary excitations in semiconductor nanostructures. Those excitations can be categorized into three different groups: Charge- (CDE) and spin-density excitations (SDE), which count among the collective electron modes, and the historically labeled single-particle excitations (SPE). While SPE reflect only discrete transitions in a non-interacting single-particle picture, collective excitations take direct- and exchange-Coulomb interactions into account and hence are shifted to higher and lower energies, respectively. In the following, these elementary excitations will be introduced in detail.

3.1.1 Single-particle continua

The nature of the single-particle excitations was for a long time thought to be not affected by Coulomb interactions, but has been controversially discussed over years. In fact, these excitations are subjected to a collective nature as well [DS99, Sch06], but since their energies are close to single-particle transitions, the excitations are treated and labeled as SPE further on.

Considering a simplified picture of non-interacting particles in a 2DES, the possible excitations from the Fermi sea include intersubband transitions between different energy subbands and intrasubband transitions within an occupied subband. Such a situation with selected excitations is illustrated in Fig. 3.1. While intersubband transitions, represented by solid arrows, occur either vertically ($q=0$) or tilted ($q\neq 0$) in the dispersion relation, a finite wave-vector transfer is indispensable for transitions within a single subband (dotted arrow). A so called single-particle continuum is then formed by regarding all possible SPE for every transferred wave vector q . Figure 3.2 shows the continua for the first two sub-

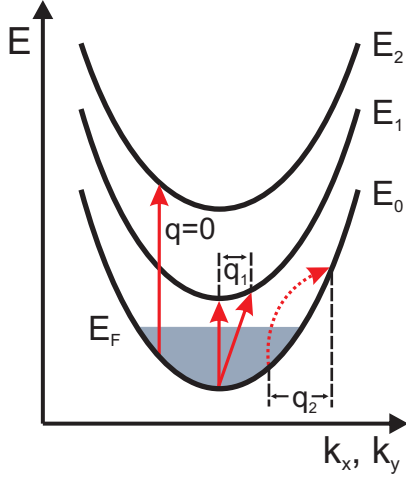


Figure 3.1: Schematic picture of single-particle excitations in a 2DES. Intersubband and intrasubband transitions are indicated by solid and dotted arrows, respectively. The subbands are described by a paraboloid in the k_x - k_y plane.

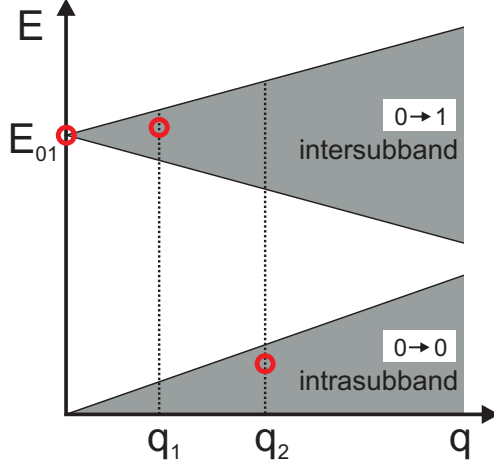


Figure 3.2: Single-particle continua formed by the parabolic behavior of the conduction bands. Selected intra- and intersubband transitions of the first two subbands are marked. The continuum for transitions to the E_2 subband is not shown here.

bands¹⁵ together with a qualitative localization of the excitations from Fig. 3.1. The upper edge of the intrasubband continuum can be determined in a parabolic approximation of the conduction bands as

$$E(k_F + q) - E(k_F) = \frac{\hbar^2(k_F + q)^2}{2m^*} - \frac{\hbar^2 k_F^2}{2m^*} = \frac{\hbar^2 q k_F}{m^*} + \frac{\hbar^2 q^2}{2m^*} \approx \frac{\hbar^2 q k_F}{m^*}, \quad (3.1)$$

assuming a rather large Fermi wave vector k_F compared to the transferred wave vector q [Sch06]. As indicated in the schematic picture, the two-dimensional subbands are described by rotational paraboloids in the k_x - k_y -plane, giving rise to intrasubband transitions with infinitesimally small energies starting at the Fermi edge up to any point of the paraboloid. Consequently, the lower edge of this continuum is approximately zero for all $q < 2k_F$. For intersubband transitions (here: $E_0 \rightarrow E_1$), the edges of the continuum are given by

$$E_{01} + E(k_F \pm q) - E(k_F) = E_{01} \pm \frac{\hbar^2 q k_F}{m^*} + \frac{\hbar^2 q^2}{2m^*}, \quad (3.2)$$

with the subband spacing $E_{01} = E_1 - E_0$ for each selected inplane wave vector $\mathbf{k}_{\parallel} = (k_x, k_y)$. Considering only vertical transitions, a discrete spectrum of intersubband excitations with equal energy spacing is obtained. However, transferring a certain wave vector q to the system, the carrier density N_s of the Fermi sea may be derived from intrasubband transitions by means of Eq. (3.1) and the relation

$$k_F = \sqrt{2\pi N_s}. \quad (3.3)$$

¹⁵The intersubband transition from E_0 to E_2 is therefore not shown in Fig. 3.2.

An application of this carrier-density determination will be presented in Chap. 4, where we focus on the intrasubband excitations of the investigated samples.

3.1.2 Collective charge- and spin-density excitations

The above introduced SPE are based on the principle of non-interacting particles, but collective effects may not be neglected in a 2DES. A response of the Fermi sea to a single electron transition can cause an energetic shift of the excitation according to interaction effects of the charge carriers. We will continue this discussion by means of an actual Raman spectrum, obtained without a transferred wave vector ($q \cong 0$).

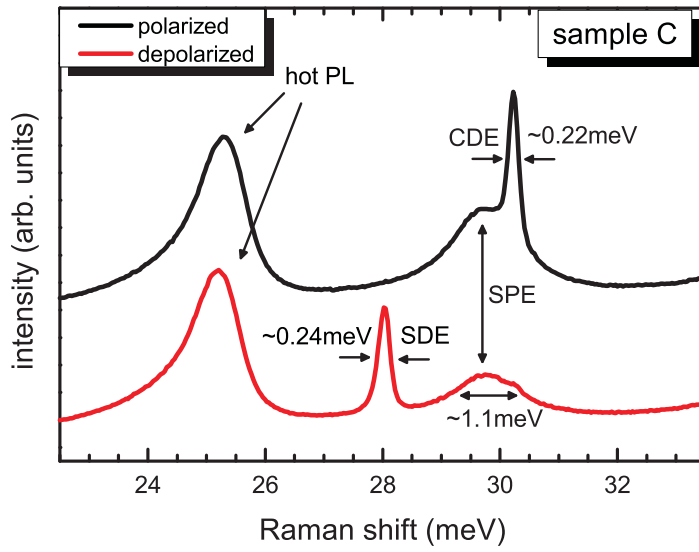


Figure 3.3: Raman spectra of intersubband transitions in sample C for a laser energy of 1.57 eV. Collective excitations (SDE and CDE) are characterized by sharp lines, while the SPE features a broad FWHM. Additionally, a hot photoluminescence can be identified at lower energies.

Figure 3.3 shows the intersubband transitions of sample C and is obviously more complex as expected from the considerations in the previous section. The SPE at the bare subband spacing E_{01} was supposed to exhibit a sharp transition energy, but manifests itself as a broad feature in the excitation spectra. Furthermore, the SPE is enclosed by narrow peaks which can be ascribed to collective modes of the Fermi sea. Those charge- and spin-density excitations appear only in polarized and depolarized spectra, respectively, and are asymmetrically shifted against the energy of the single-particle transition. Here, we already make use of the polarization selection rules, which will be introduced in Chap. 3.1.4 in more detail. Additionally, a photoluminescence from a higher subband, so called hot PL, is detected at lower energies.

A phenomenological description of the collective modes is presented in Fig. 3.4. Macroscopically, an intersubband CDE of a 2DES is an in-phase oscillation of electrons perpendicular to the quantum well plane. The motion of the oscillating charge carriers is restricted by the interfaces of the quantum well. Going to microscopic scales, the intersubband CDE is a spin-conserving single-particle transition, which is subjected to the full quantum-mechanical Coulomb interaction [Sch06]. By contrast, the intersubband SDE embodies an opposite phase oscillation for

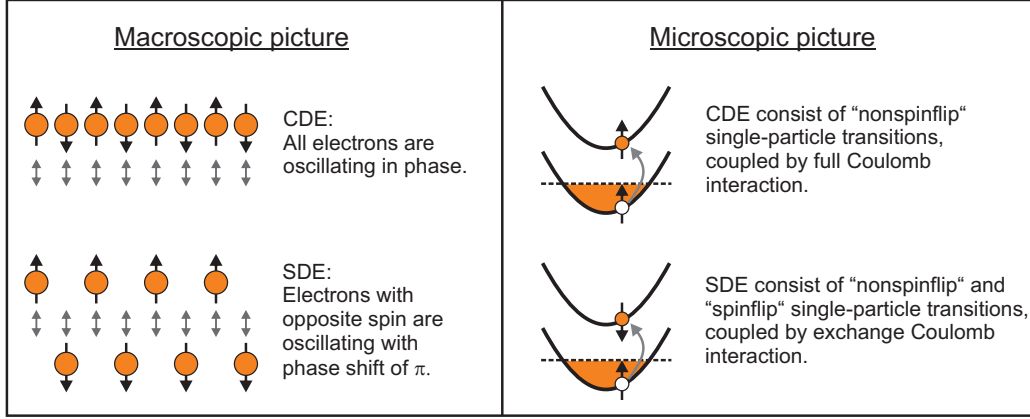


Figure 3.4: *Macroscopic and microscopic picture for collective intersubband excitations. Adapted from [Sch06].*

electrons with different spins. Since the center of mass of the charge remains motionless in this configuration, all depolarization field effects vanish and hence, the SDE are only coupled by the exchange part of the Coulomb interaction. Here, the transition microscopically includes spin-flip as well as non spin-flip processes.

On a theoretical point of view, an excitation spectrum of an interacting system can be calculated in random-phase approximation (RPA) [Ste67, Jai87]. This approach incorporates dynamical processes by a time-dependent Hartree approximation, treating the Coulomb interaction as a classical effect. A further improvement may be achieved by including exchange correlation effects via a LDA potential, accordingly denoted as time-dependent local density approximation (TDLDA) [And82, Tse84]. A detailed description of the method can be found in Ref. [Sch06], here, only the basic outline of the calculation is presented:

If the local charge and spin density is perturbed by an electromagnetic dipole field $\mathbf{E}(t) = \mathbf{e}_z E_{ext} e^{-i\omega t}$, the Hamiltonian of the electronic ground state H_0 has to be extended by a perturbation term to $H = H_0 + H_1(t)$. The corresponding equation of motion for the density operator $\rho = \rho_0 + \rho_1(t)$ is given by the von Neumann equation:

$$\frac{d}{dt}\rho = -\frac{i}{\hbar} [H, \rho] \quad (3.4)$$

Assuming a coupled temporal dependence of external perturbation and response of the system, we can write

$$H_1(t) = H_1 e^{-i\omega t} \quad \text{and} \quad \rho_1(t) = \rho_1 e^{-i\omega t} . \quad (3.5)$$

For the simplified picture of a two-subband system in a quantum well structure, the perturbation operator H_1 in the considered z direction is represented by

$$H_1 = V_{ext} + \Delta V_{Coul} + \Delta V_{XC} , \quad (3.6)$$

with the direct part ΔV_{Coul} (Hartree term) and the exchange part ΔV_{XC} of the Coulomb interaction. Considering vertical transitions ($q = 0$) between both

subbands, while only the lower one is occupied with a carrier density N_s , the perturbation-induced density change follows as

$$\delta n(z) = 2N_s \frac{E_{01}}{(\hbar\omega)^2 + E_{01}^2} \chi_0(z) \chi_1(z) \langle 1 | H_1 | 0 \rangle , \quad (3.7)$$

where $\chi_i(z)$ is the envelope function and E_{01} the subband spacing. This induced density entails a dynamical modification of the Hartree and the exchange-correlation potential, which can be calculated by inserting $\delta n(z)$ into Eq. (3.6). If the external perturbation is assumed to be zero ($V_{ext} = 0$), the excitation energies for collective intersubband transitions are given by

$$E_{CDE_{01}}^2 = E_{01}^2 (1 + \alpha_{11} + \beta_{11}) \quad (3.8)$$

$$E_{SDE_{01}}^2 = E_{01}^2 (1 + \beta_{11}) , \quad (3.9)$$

with α_{11} and β_{11} as the direct and the exchange part of Coulomb interaction, respectively¹⁶:

$$\alpha_{11} = -\frac{2e^2 N_s}{\epsilon_\infty \epsilon_0 E_{01}} \int_{-\infty}^z dz' \int_{-\infty}^{z'} dz'' \chi_1(z'') \chi_0(z'') \quad (3.10)$$

$$\beta_{11} = \frac{2N_s}{E_{01}} \int_{-\infty}^{\infty} dz \frac{\partial V_{XC}}{\partial n} \chi_1^2(z) \chi_0^2(z) \quad (3.11)$$

The classical Coulomb potential represents the influence of depolarization field effects and causes a blueshift ($\alpha_{11} > 0$) of the collective mode, whereas a reversed tendency ($\beta_{11} < 0$) appears for the excitonic shift induced by the exchange correlation. Since the relation $|\alpha_{11}| > |\beta_{11}|$ holds for 2DES with moderate carrier densities in the range of 10^{11} cm^{-2} [Sch06], the CDE_{01} is blueshifted and the SDE_{01} is redshifted with respect to the corresponding single-particle transition (see Fig. 3.3). Another interesting phenomenon concerning intersubband CDEs is the ability to couple with LO phonons. However, the appearance of this effect is limited to polar semiconductors like GaAs, since the coupling mechanism is based on the macroscopic electric field of the CDE. As a consequence, the high-frequency dielectric constant ϵ_∞ in Eq. (3.8) has to be substituted by the frequency-dependent dielectric function of the host lattice [Sch06]:

$$\epsilon(\omega) = \epsilon_\infty \frac{E_{LO}^2 - (\hbar\omega)^2}{E_{TO}^2 - (\hbar\omega)^2} \quad (3.12)$$

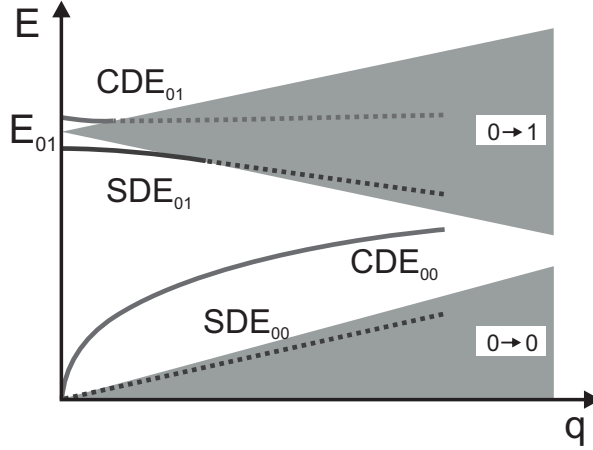
This coupling is rather weak for a reasonably large separation of plasmon and phonon energy, but reducing the energetic distance would yield two coupled plasmon-phonon modes with energies above and below the LO phonon mode:

¹⁶The Coulomb parameters α_{11} and β_{11} may not to be confused with the Rashba (α) and the Dresselhaus (β) parameter of the SOI, which will be introduced in Chap. 4.

$$E_{\pm} = \left\{ \frac{1}{2} [E_{LO}^2 + E_{01}^2(1 + \alpha_{11})] \pm \frac{1}{2} \sqrt{[E_{LO}^2 + E_{01}^2(1 + \alpha_{11})]^2 - 4E_{01}^2[E_{LO}^2 + E_{TO}^2\alpha_{11}]} \right\}^{1/2} \quad (3.13)$$

An experimental observation of this coupling is presented in the second part of this chapter, where we focus on the results of a 25 nm-wide quantum well structure.

Figure 3.5: *Schematic picture of the dispersion of electronic excitations within the first two subbands of a 2DES. Collective modes are only defined eigenmodes of the system outside the single-particle continua, inside they are Landau damped.*



We will now conclude these theoretical considerations and come back to the phenomenological treatment introduced in the previous section. Figure 3.5 shows the single-particle continua for the first two subbands together with the dispersions of the collective modes. Strictly speaking, these excitations are only defined eigenmodes of the system for states outside the continua, while a single-particle character appears once their dispersion enters the corresponding continuum. Such a decay into uncorrelated electron-hole pairs is called Landau damping [Lan46]. But collective modes are not restricted to transitions between subbands, because intrasubband excitations might occur as well in a 2DES. Macroscopically, these excitations can be regarded similar to the intersubband transitions, but now with an oscillation parallel to the quantum well plane. The energy of the intrasubband CDE_{00} has a square-root dependency on the in-plane wave vector q_{\parallel} and is given by [Ste67]

$$E_{CDE_{00}}^2 = \frac{N_s \hbar^2 e^2}{2 \epsilon_{\infty} \epsilon_0 m^*} q_{\parallel} \quad (3.14)$$

On the contrary, the intrasubband SDE_{00} is Landau damped for every possible wave vector, as Fig. 3.5 assumes. Consequently, the dispersion is essentially determined by the upper edge of the intrasubband continuum:

$$E_{SDE_{00}}^2 = \frac{2\pi N_s \hbar^4}{m^{*2}} q_{\parallel}^2 \quad (3.15)$$

In Chap. 4, we will investigate the intrasubband transitions of the studied samples, while the main focus is on the SDE_{00} . Hence, we will probe these equations in terms of validity and comparability concerning real systems.

3.1.3 Scattering process

In the following, the microscopic scattering mechanism of electronic excitations in semiconductor nanostructures is elucidated. Although a lot of theoretical work has been performed on dynamic Raman response without resonant conditions (see, e. g., Ref. [Jai85, DS98]), the scattering process in a 2DES appears to be strongly influenced by an intermediate state of the valence band [DS99]. Therefore, we will only elaborate on the dominant scattering mechanism involving interband resonance conditions between valence and conduction band.

A quantum mechanical description of the scattering process is based on the interaction between the state of the incident $(\omega_I, \mathbf{k}_I, \mathbf{e}_I)$ and the state of the scattered $(\omega_S, \mathbf{k}_S, \mathbf{e}_S)$ light. Here, $\mathbf{e}_{I,S}$ represents the polarization vector for the corresponding photons. The Hamiltonian for the perturbed system reads [Sch06]

$$H = \sum_i \left[\frac{1}{2m} (\mathbf{p}_i + e\mathbf{A}(\mathbf{r}_i))^2 + U(\mathbf{r}_i) \right] + V_{e-e} + V_{e-ph} =$$

$$H_0 + \underbrace{\frac{e^2}{2m} \sum_i (\mathbf{A}(\mathbf{r}_i))^2}_{H_p^{(1)}} + \underbrace{\frac{e}{2m} \sum_i [\mathbf{p}_i \mathbf{A}(\mathbf{r}_i) + \mathbf{A}(\mathbf{r}_i) \mathbf{p}_i]}_{H_p^{(2)}} , \quad (3.16)$$

while the spin-orbit coupling is neglected for simplicity. The light-matter interaction is introduced by replacing the momentum \mathbf{p} of the electron by $\mathbf{p} + e\mathbf{A}$, where \mathbf{A} is the vector potential of the light. The Coulomb and the electron-phonon interaction are given by V_{e-e} and V_{e-ph} , respectively, and $U(\mathbf{r}_i)$ describes the sum of all external and lattice periodic potentials. Considering the perturbation, $H_p^{(1)}$ represents first-order terms which do not contribute to the resonant scattering mechanism, while $H_p^{(2)}$ is treated by second-order perturbation theory. If $H_p^{(2)}$ is additionally extended by the Coulomb or the electron-phonon interaction, third-order terms arise and need to be taken into account. Since this work is focused on scattering by electronic excitations, the potential fluctuation involving phonons is not of further interest here. The dominant contribution to electronic Raman scattering is provided by second-order (SOP) and third-order (TOP) scattering processes due to their resonant behavior with the valence band states.

A first microscopic model for electronic scattering events was proposed by Burstein et al. in 1980 [Bur80]. They described single-particle and collective excitations for intersubband transitions in a 2DES. Figure 3.6 (a) and (b) show the adapted models for intrasubband excitations, which are more relevant for this work. In a first step, an electron is excited from the valence band to the conduction band, followed by a recombination of the created hole with an electron from the Fermi sea. Depending on the spin orientation of both electrons, the spin state

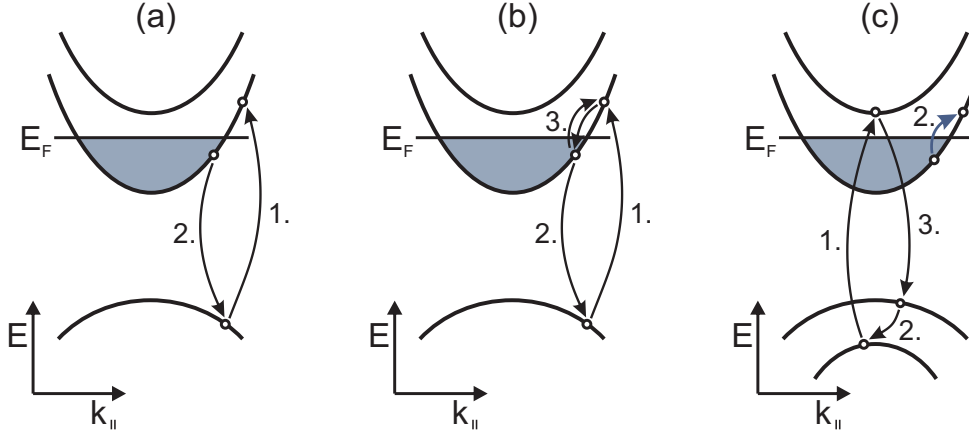


Figure 3.6: Schematic picture of different scattering mechanisms for intrasubband transitions in a quantum well system. The two-step (a) second-order scattering process describes a single-particle excitation, while the three-step process (b) represents an obsolete concept of a collective excitation (both adapted from [Bur80]). Under experimental conditions, the third-order excitonic scattering mechanism (c) appears to be dominant for collective plasmon excitations (adapted from [Jus00]).

is either conserved or flipped during the scattering process. At this point, the two step SOP (a) is completed and describes a single-particle transition, while the three-step SOP (b) involves an additional process. In this third step, the Coulomb interaction is taken into account and leads to a screening of the electron system, where a SPE is created at the expense of another SPE. As a consequence, collective CDEs and SDEs are formed by direct and exchange Coulomb coupling [Sch06]. Under experimental conditions, however, another process has appeared to be dominant for collective modes. The first approach for intersubband excitations was published by Danan et al. in 1989 [Dan89], followed a few years later by a model for transitions within a single subband, proposed by Jusserand et al. [Jus00]. In the first step of such a TOP (see Fig. 3.6 (c)), an exciton with a hole in a deeper valence band and an electron in a higher conduction band is created by an incident photon. This exciton is scattered by interaction effects with the Fermi sea and creates a collective excitation in the conduction band, while at the same time an electron from a higher valence band relaxes into the vacant deeper-situated valence band state to ensure energy and momentum conservation. As a last step, the scattered exciton recombines.

This leaves us with two relevant mechanisms, the two step SOP for single-particle excitations (a) and the TOP for collective plasmon excitations (c). The resonance of these mechanisms appears to be strongly dependent on the specific wave vector of the excitation [Jus00]. While the SPE resonate at the Fermi edge (see Fig. 3.6 (a)), plasmons are associated to excitons at the zone center (see Fig. 3.6 (c)) and hence, both excitations are enhanced at different incident energies. Furthermore, the energetic region of the plasmon resonance was found to be fairly sharp (≈ 2 meV) compared to the broad resonance of the SPE (≈ 25 meV). An explanation for the SPE resonance close the Fermi edge may be given by

means of an electron density fluctuation mechanism proposed in Ref. [DS99], which describes the direct coupling of the incident photon to the Fermi sea. On the other hand, the sharp resonance region of the plasmon originates from the double-resonance behavior of the TOP scattering mechanism. Consequently, the plasmon intensity decreases rapidly if the laser energy is detuned from this critical point [Jus00]. Although a doubly-resonant Raman scattering was already reported for optical phonons [Kle87, Sch91] and intersubband excitations [Dan89], the impact of this mechanism on collective intrasubband electronic excitations was underestimated for a long time.

3.1.4 Scattering cross section and selection rules

After the microscopic models for inelastic light scattering have been introduced, we will now elaborate on the scattering cross section for an excitation in an electronic system. Following a work of Hamilton and McWhorter [Ham69], the differential cross section is given by

$$\frac{d^2\sigma}{d\Omega d\omega} = \frac{\omega_S}{\omega_I} \frac{e^4}{m^2 c^4} S(\omega) , \quad (3.17)$$

where the structure factor $S(\omega)$ determines the transition rate between the incident $(\omega_I, \mathbf{k}_I, \mathbf{e}_I)$ and the scattered photon $(\omega_S, \mathbf{k}_S, \mathbf{e}_S)$:

$$S(\omega) = \left\langle \sum_S |\langle S | \hat{V}_{eff} | I \rangle|^2 \delta(E_I - E_S - \hbar\omega) \right\rangle \quad (3.18)$$

The effective operator \hat{V}_{eff} describes a transition of the many-particle system from the initial state $|I\rangle$ with energy E_I to the scattered state $\langle S|$ with energy E_S , where an energy $\hbar\omega$ is transferred to the system. In such a many-particle system, the operator for the light scattering can be expanded using second quantization [Gov97]:

$$\hat{V}_{eff} = \sum_{\alpha, \beta} \gamma_{\alpha\beta} \hat{c}_\beta^\dagger \hat{c}_\alpha \quad (3.19)$$

Here, \hat{c}^\dagger and \hat{c} denote the creation and annihilation operator, respectively, while α and β represent sets of quantum numbers, which characterize the corresponding single-particle states. Assuming a simplified picture with noninteracting electron-hole pairs instead of excitons, the scattering amplitude $\gamma_{\alpha\beta}$ can be written as [Blu70, Gov97]

$$\begin{aligned} \gamma_{\alpha\beta} \sim & \langle \alpha | e^{i\mathbf{q}\cdot\mathbf{r}} | \beta \rangle \mathbf{e}_I \mathbf{e}_S + \frac{1}{m} \sum_{\beta'} \frac{\langle \alpha | \mathbf{p} \mathbf{A}_S | \beta' \rangle \langle \beta' | \mathbf{p} \mathbf{A}_I | \beta \rangle}{E_\beta - E_{\beta'} - \hbar\omega_I} + \\ & \sum_{\nu\nu'} \frac{\langle \beta | \mathbf{p} \mathbf{A}_S | \nu' \rangle \langle \nu' | \hat{V}_{e-e} | \nu \rangle \langle \nu | \mathbf{p} \mathbf{A}_I | \alpha \rangle}{(E_\beta - E_{\nu'} - \hbar\omega_S)(E_\alpha - E_\nu - \hbar\omega_I)} , \end{aligned} \quad (3.20)$$

where only the dominant terms for the resonant light scattering are regarded. Nonresonant contributions from first-order perturbation theory are caused by the

first term of Eq. (3.20). However, the scalar product of the polarization vectors $\mathbf{e}_{I,S}$ restricts the nonresonant process to light scattering on plasmons (CDEs), while spinflip processes, which occur in SDEs, are only allowed under resonant conditions. The intermediate term corresponds to the second order process and yields under extreme resonance the contribution of scattering by single-particle excitations, as sketched in Fig. 3.6 (a). We will come back to this term extensively in Chap. 4, where the scattering amplitude for spin-flip intrasubband transitions will be of further interest. The last term in Eq. (3.20) describes the contribution of the excitonic scattering, treated in third-order perturbation theory. Considering the denominators, the resonance effects for single-particle transitions as well as the double resonance for excitonic scattering by collective excitations are clearly visible.

Selection rules

As a direct consequence from the scattering cross section, the polarization selection rules, which have been taken for granted so far, may be derived. Equation (3.20) contains in each term of the scattering amplitude $\gamma_{\alpha\beta}$ not only the participating conduction- and valence-band states, but also the polarizations of incident and scattered photons¹⁷. It follows from the Bloch part of the wave functions that the scattering by charge-density waves varies with the scalar product ($\mathbf{e}_I \cdot \mathbf{e}_S$), while the scattering amplitude for spin-density scattering is proportional to $\boldsymbol{\sigma}(\mathbf{e}_I \times \mathbf{e}_S)$ [Ham69]. These expressions are valid for zinc-blende based semiconductors with a band structure, which can be treated by the 8-band band edge Bloch functions within the Kane model. Hence, the selection rules read

$$\mathbf{e}_I \parallel \mathbf{e}_S \quad (3.21)$$

for charge-density excitations in a *polarized* scattering configuration, and

$$\mathbf{e}_I \perp \mathbf{e}_S \quad (3.22)$$

for spin-density excitations in a *depolarized* scattering configuration. This allows an experimental selection between CDE and SDE by adjusting the polarization parallel and crossed, respectively. A more detailed derivation of the selection rules can be found in Ref. [Sch06]. Since both deduced expressions are based on the Bloch part of the wave function, the polarization selection rules hold for any given dimensionality of the system. Considering semiconductor nanostructures, however, an additional aspect needs to be taken into account. In a 2DES, the states are characterized by Bloch and envelope wave functions, which emerge from the confinement potential in the growth direction. The corresponding overlap integrals of these envelope functions give rise to the parity selection rules in

¹⁷For second and third order processes, the polarization vectors are incorporated in the vector potential \mathbf{A} .

a quantized system. For a Raman spectrum it follows that only excitations with even parity are allowed, since Raman scattering is subjected to a two-photon process. Strictly speaking, these parity selection rules hold for symmetric potentials, mainly, whereas they are softened for excitations in asymmetric quantum wells. As a consequence, an impact on the actual spectrum is expected only for sample D, which was designed to provide a symmetric structure.

3.2 Scattering from intersubband excitations

Within the current chapter, we learned about the significance of the resonant intermediate state in the valence band. For GaAs, the first single-particle excitations under extreme resonance were reported in 1971 for intrasubband transitions in bulk material [Pin71]. Throughout the following years, Pinczuk and Abstreiter strongly impelled the research by inelastic light scattering and observed the first collective modes for intersubband excitations in a 2DES [Abs79, Pin80]. Further studies revealed the important role of the direct and exchange Coulomb interaction for the scattering process of collective modes and compared the experimental findings with prevalent RPA-based theories [Pin89, Gam90, Gam92]. But electronic Raman scattering is not only limited to bulk or quantum well systems, and thus modern advances in sample preparation paved the way to extensive investigations on quasi one- or even zero-dimensional structures [Ege90, Str94, Sch96, Sch98].

More recent publications on light scattering from intersubband excitations in a 2DES have shown a strong dependency of the electronic Raman modes on the quantum well width [Unu04, Unu06]. We will capture this statement and present in the following our results on intersubband transitions. By comparing two quantum well structures with a considerable difference in the well width, we can draw some conclusions about the subband spacing and its impact on particular excitations.

3.2.1 25 nm-wide quantum well

Before we move on to the main part of this work, which addresses the intrasubband transitions in our samples, we dedicate some attention to our experimental findings on intersubband excitations. This serves to intensify the gained knowledge about the scattering process and to develop a sense for the proportions in a quantum well system.

Figure 3.7 shows for both scattering configurations a waterfall plot of Raman spectra of sample C, a two-dimensional structure with a rather high quantum well width of 25 nm. A variation of excitation energy between 1.58 and 1.61 eV allows a detection of resonance effects with the valence band by scanning over different $k_{||}$ -points in the reciprocal space. All spectra, except the bottom ones, have been shifted successively to larger Raman shifts to provide a clearer depiction of excitations. The polarization selection rules distribute CDE and SDE to polarized and depolarized geometry, respectively, while SPE are visible in each configuration.

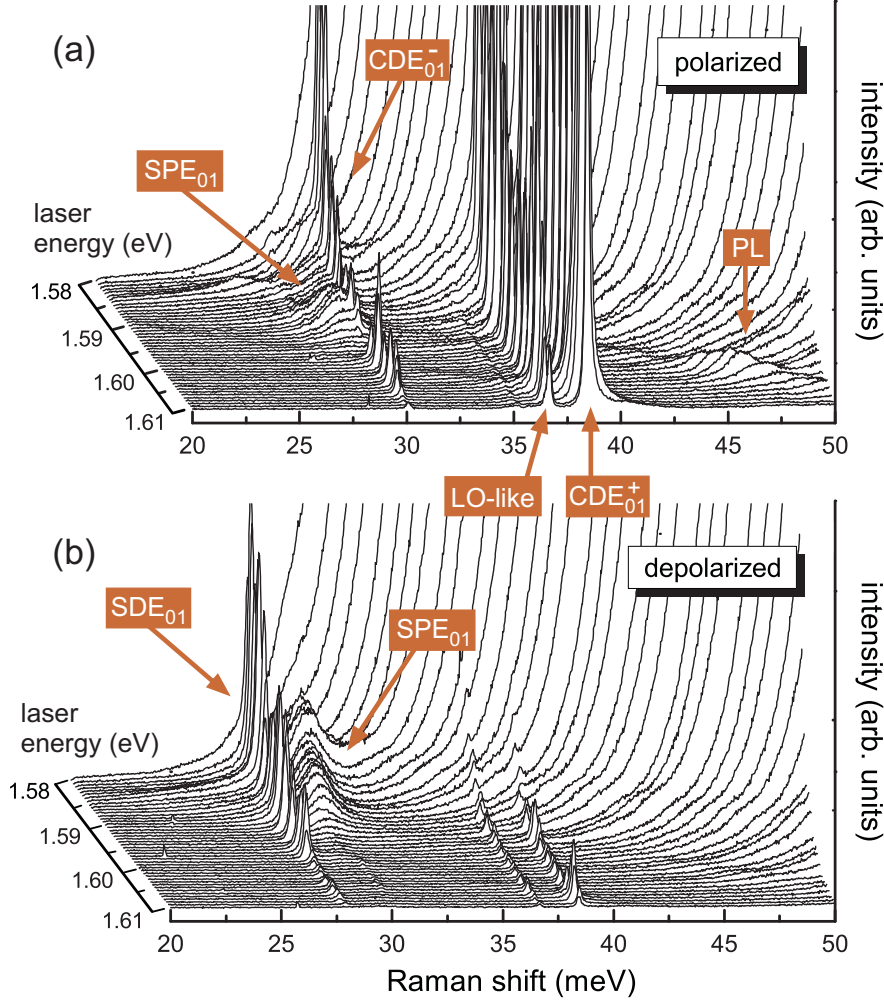


Figure 3.7: Waterfall plot for sample *C* in polarized (a) and depolarized (b) scattering geometry, measured at $T = 5.5$ K. Since no wave vector is transferred ($q = 0$), all depicted excitations reflect intersubband transitions, which occur vertically in the k -space. By tuning the laser energy between 1.58 and 1.61 eV, various resonances with different valence bands may be approached.

A strong phonon-plasmon coupling in this sample results in a distinct plasmon-like CDE_{01}^- mode and a very powerful CDE_{01}^+ mode, which features a phonon-like characteristic. The additional excitation at ≈ 37 meV stems most likely from a coupled mode of a transition to a higher subband is strongly enhanced due to its close proximity to the phonon energy (≈ 36.5 meV). These two coupled modes between 35 and 40 meV are dominant enough for a perceptible residue in the depolarized spectra, even though they are not allowed by the selection rules. The tiny spike on the low-energy side of the phonon at about 35 meV in the polarized spectra might be also ascribed to a transition involving a higher subband, but this excitation is very weak pronounced only. Because no other hints of excitations involving higher subbands are identifiable, we suppose an unoccupied or at least a rather low occupied second subband. Despite that, the increasing background in both plots can be attributed to a hot photoluminescence from this second sub-

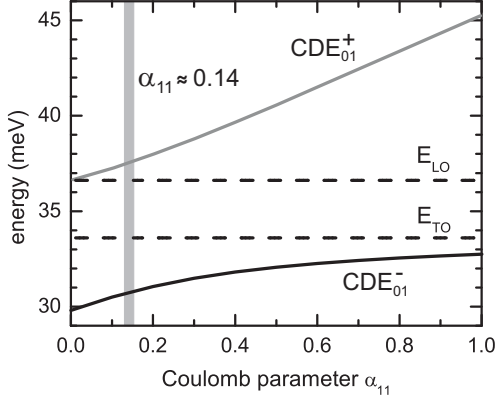


Figure 3.8: Coupled plasmon-phonon modes for a subband spacing $E_{01} = 29.8 \text{ meV}$, calculated with Eq. (3.13).

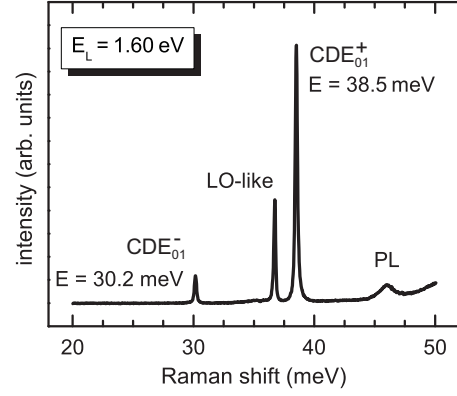


Figure 3.9: Experimental Raman spectrum of sample C in polarized scattering geometry.

band. In general, a luminescence can be distinguished from a Raman signal by the tilted progression in such waterfall plots, while excitations from Raman scattering keep their energy for different laser wavelengths. This is a direct consequence of the relative manner of representation with respect to the excitation wavelength. However, the consistent energy of Raman modes is only valid for an equidistant subband spacing in the k -space. Since all Raman modes here feature a constant energy, this assumption holds for excitations in the vicinity of the Γ -point.

An additional hot photoluminescence (labeled PL) from a higher subband can be seen especially in the polarized spectra and triggers a resonant enhancement of the single-particle excitation during the crossing. This SPE from the lowest to the first subband exhibits a fairly broad linewidth ($\approx 1.2 \text{ meV}$) compared to the sharp lines of both collective modes ($\approx 0.2 \text{ meV}$). Usually, a similar strength of depolarization and excitonic shift is expected, but this structure reveals a strong anisotropy in the energetic shift of CDE ($+0.4 \text{ meV}$) and SDE (-1.8 meV) concerning the single-particle transition. Such a comparatively low value for the charge wave can be ascribed to the strong coupling with the LO phonon (at $\approx 36.5 \text{ meV}$), which results in a redshifted CDE_{01}^- mode.

If we extract the energies of single-particle and collective excitations from the measurement, we can deduce with Eq. (3.8) and (3.9) $\alpha_{11} \approx 0.14$ as the direct and $\beta_{11} \approx -0.12$ as the exchange part of Coulomb interaction. This allows a calculation of coupled plasmon-phonon modes after Eq. (3.13), which is illustrated in Fig. 3.8. The crossing points of the grey shaded area around $\alpha_{11} = 0.14$ with the plasmon-phonon modes mark the expected energies for charge-density waves of the first two subbands in our sample. Comparing these values with an experimental spectrum, exemplarily depicted in Fig. 3.9 for a laser energy of 1.60 eV , we can find a reasonable accordance. Furthermore, the attenuated intensity of the SPE with respect to CDE and SDE confirms the claim of a dominating characteristic of collective modes in large quantum wells [Unu04, Unu06]. How and if this emphasis is shifted for a narrowed well width will be clarified in the subsequent section, for

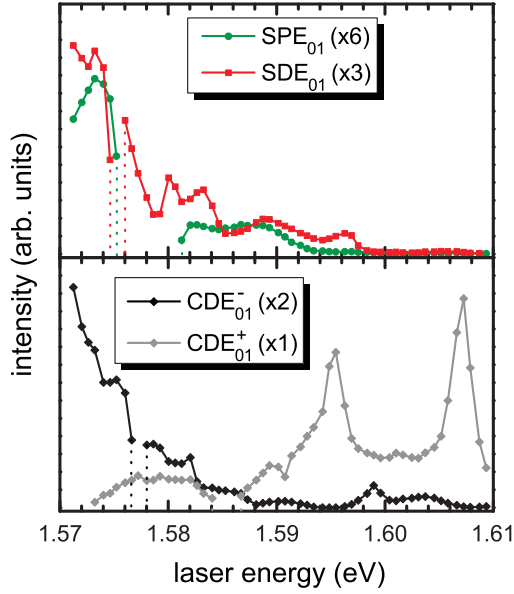


Figure 3.10: *Resonance profile of sample C for collective and single-particle modes. The intensities are scaled to provide a better comparability.*

reveal mainly sharp lines, which are very well expected for the doubly resonant excitonic scattering process. On the contrary, the SPE shows a wide resonance profile, which is already clearly visible in the previous depicted waterfall plots.

now we consider the intensities of the participating Raman modes in a little bit more detail.

Figure 3.10 depicts the resonance profiles for the investigated intersubband transitions in sample C. The background from the photoluminescence is eliminated as far as possible, however, the hot luminescence from the first subband, visible as the background in Fig. 3.7, yields a huge intensity and overlays the excitations completely by its crossing. This is marked as a small (or in the case of the SPE as a large) interruption in the resonance profile. Additionally, the integrated intensities are scaled to provide a better comparability. Considering the collective modes, several resonances with different valence subbands are visible. These resonances are energetically close due to the large quantum well width and

Intersubband transitions with a transferred wave vector q

So far we considered only intersubband transitions which occur vertically in the k -space. In the following, we will elucidate what happens for a finite wave-vector transfer of q and try to verify the schematic picture of the dispersion of electronic excitations in a 2DES (see Fig. 3.5). For that, we keep the excitation energy fixed at a good resonance with the valence band and vary the incident angle θ of the laser light in small steps.

Selected spectra for polarized and depolarized geometry are shown in Fig. 3.11 (a) and (b), respectively. The shape of the spectra without a transferred wave vector is basically familiar from previous figures. In the parallel scattering configuration, the CDE has a dominating intensity with a sharp linewidth and is located close to the broad single-particle transition, since it is downshifted in energy due to the coupling with the LO phonon. The crossed configuration exhibits a larger distance of the sharp SDE to the bare subband spacing. By increasing the transferred wave vector, the shape of the excitations seems to soften and the intensity drops. To provide a more detailed evaluation, the values for the Raman shift and the FWHM are extracted from all measured spectra and plotted in Fig. 3.11 (c)

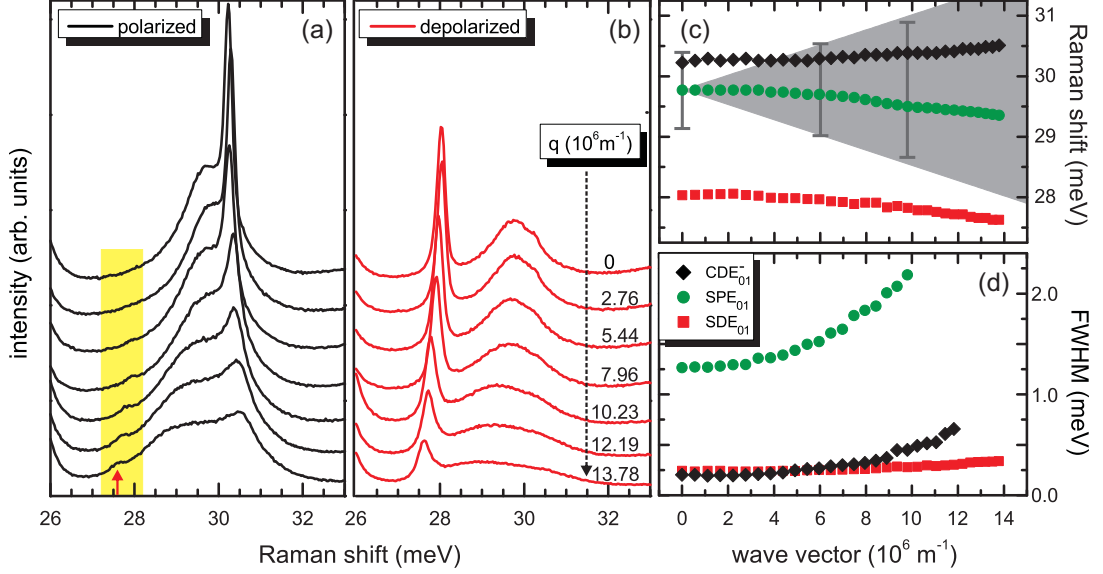


Figure 3.11: Selected spectra for intersubband transitions between the first two subbands in sample C for polarized (a) and depolarized (b) scattering geometry, measured at $T = 5.5\text{ K}$. The laser energy was fixed at $E_L = 1.571\text{ eV}$ and the transferred wave vector was varied up to $q = 13.78 \times 10^6\text{ m}^{-1}$, which corresponds to an incident angle of $\theta = 60^\circ$. All intensities are successively shifted for a clearer presentation. Additionally, the extracted values for Raman shift (c) and FWHM (d) are plotted with respect to the transferred wave vector. The grey shaded area in (c) symbolizes the single-particle continuum calculated after Eq. (3.2), while the size of the error bars stems from the FWHM of the corresponding SPE.

and (d) against the transferred wave vector. Since the shape of the single-particle transition is superimposed by the strong CDE, the analysis of the SPE is based only on the depolarized spectra. Nevertheless, qualitative claims about its behavior should not be affected. To bridge the gap between experimental values and theoretical treatment (see Fig. 3.5), the single-particle continuum for the first two subbands is calculated after Eq. (3.2) and implemented in subframe (c) as a grey shaded area, using the bare subband spacing obtained from the measurement and a carrier density of $N_s = 2.1 \times 10^{11}\text{ cm}^{-2}$. Considering the Raman shift, we can identify almost constant values for $q \leq 7 \times 10^6\text{ m}^{-1}$, whereas all excitations start to shift their energy for higher wave vectors. For the sake of completeness it must be stated, that the energy of the SPE contains a considerable uncertainty due to its broad shape, especially for very high q . The phenomenological background of the behavior becomes clearer by regarding the linewidth of each transition. At $q = 0$, we detect the sharp line of CDE and SDE with a $\text{FWHM} \approx 0.25\text{ meV}$, while the linewidth of the SPE is enhanced by more than a factor of 4. This represents the common expectation for scattering processes in a fairly large quantum well system. For finite wave vectors, a sharp rise of the SPE linewidth appears, which reflects the uniform broadening of the single-particle continuum for an increasing q . If we plot these values as error bars in subframe (c), which is exemplarily

shown for three selected wave vectors, we can find a great accordance with the borders of the calculated single-particle continuum for large q . However, there is a huge deviation for small wave vectors due to the natural broadening of the single-particle excitation. Regarding the FWHM again, we can observe for the charge wave a similar behavior as for the single-particle transition, but with an attenuated slope. On the contrary, the linewidth of the SDE remains almost unchanged for the whole range, a slight increase is visible only towards the end of the plot. This broadening of the collective modes can be directly attributed to the penetration of the dispersion into the single-particle continuum. Consequently, these modes are no longer defined eigenmodes of the system and decay into uncorrelated electron-hole pairs. The faster increase in linewidth of the CDE compared to the SDE may be explained by the energetic distance of the excitations regarding the SPE. For the charge wave, the small distance encourages a quick penetration into the continuum, whereas the SDE is Landau damped only towards higher wave vectors.

An additional hint, which reinforces this interpretation is illustrated in the yellow shaded box in Fig. 3.11 (a). Considering high wave vectors, a tiny peak at the energy of the SDE appears in the polarized spectra, although no hint of this peak is observable for $q \leq 5 \times 10^6 \text{ m}^{-1}$. This confirms the concept of an emerging single-particle character of collective modes, once their dispersion enters the single-particle continua. Consequently, the occurrence of damped collective modes is not completely limited by the polarization selection rules.

To sum up this section, we approached the theoretical picture of the different scattering processes by means of a 25 nm-wide single quantum well. The claim of dominating collective excitations in large quantum well systems could be verified, which is in accordance with several publications on intersubband transitions in GaAs/AlGaAs (see, e. g., Ref. [Pin89, Yu91]). Furthermore, the qualitative behavior of dispersions of electronic excitations in a 2DES could be reproduced for a wide range of transferred wave vector.

3.2.2 12 nm-wide quantum well

After the fundamental properties of a 25 nm-wide quantum well are clarified, we reduce the well width and consider the changed quantities of the system. Raman studies on intersubband transitions in narrower quantum well structures are quite rare in literature. Early publications discussed only very narrow well widths of 4–7 nm [Abs88] or focused on the correlation between transition energy and doping concentration [Ram90]. A more recent study of Unuma et al. in 2004 reported on the dependency of single-particle and collective excitations on the width of GaAs quantum wells, ranging from 8.5 to 18 nm [Unu04].

Subsequently, we elaborate on the peculiarities of narrow well widths by means of sample B, which contains a 12 nm-wide GaAs/AlGaAs quantum well structure. A waterfall plot of Raman spectra is shown in Fig. 3.12 for polarized (a) and de-

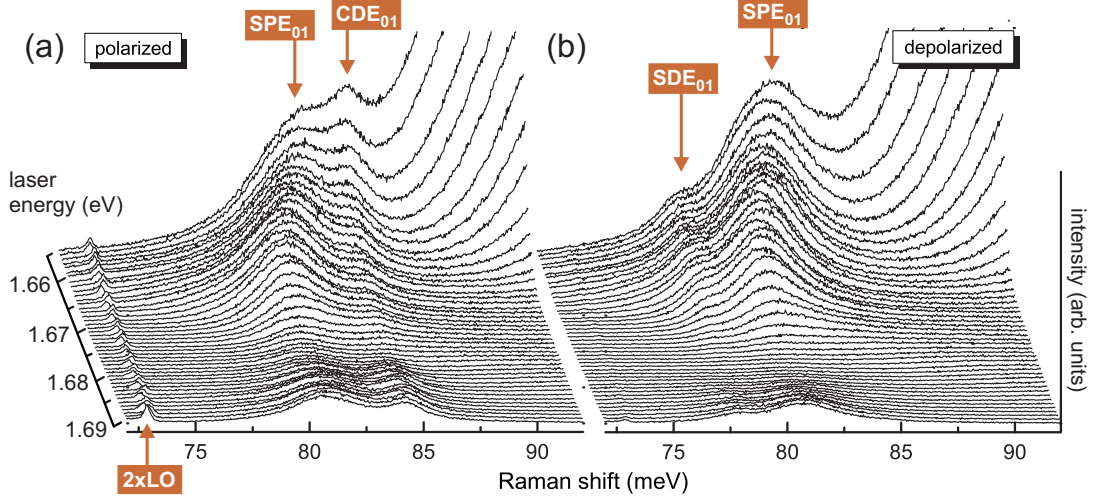


Figure 3.12: Waterfall plot for sample B in polarized (a) and depolarized (b) scattering geometry, measured at $T = 5.5$ K. The laser energy was tuned between 1.655 and 1.690 eV and all spectra show intersubband transitions without a transferred wave vector.

polarized (b) scattering geometry. The laser energy was varied between 1.655 and 1.690 eV and the increasing background stems from the photoluminescence of the fundamental band gap. For parallel polarization, the spectra yield a small peak around 73 meV, which can be attributed to a 2-LO-phonon excitation. The broad peak just above 80 meV represents the single-particle transition from the lowest to the first subband, and the shoulder on its high-energy side can be assigned to the corresponding charge-density wave. On the other hand, the depolarized spectra depict the SPE as well as the spin-density wave as a redshifted shoulder. Within the investigated energy range, a weak resonance is visible for bottom spectra, while a strong resonance emerges when the laser energy is tuned towards the band gap.

For a better comparison, all extracted values for intersubband excitations in sample B and C are presented in Tab. 3.1. As expected, the bare subband spacing increases by reducing the well width. The huge anisotropy in the energy shift of collective modes regarding the single-particle transition in the 25 nm quantum well stems from the strong coupling of the CDE to the phonon and was already addressed in the previous section. Considering the strength of depolarization and excitonic shift, we achieve higher values for sample B, which can be directly attributed to the larger carrier density and hence, stronger Coulomb parameters in this sample. The linewidth of the SPE reveals an enhanced broadening for sample B, which may correspond to an inhomogeneous broadening due to microscopic fluctuations in the well width. Since the energy of a box-like potential scales with $E \sim 1/d_{qw}^2$, structures with narrow quantum wells are strongly affected by this energy fluctuations caused by layer inhomogeneities. Taking the macroscopic focus of 80 – 100 μm for all Raman measurements into consideration, an averaging over different well widths and consequently, an influence of this effect on the spectra

sample name	width (nm) qw	E (meV) SPE ₀₁	E (meV) CDE ₀₁	E (meV) SDE ₀₁	FWHM (meV) SPE ₀₁
B	12	80.7	84.3 (+3.6)	77.9 (−2.8)	3.5
C	25	29.8	30.2 (+0.4)	28.0 (−1.8)	1.2

Table 3.1: *Extracted values for measured intersubband transitions in exact backscattering geometry. The bracketed values represent the distance to the corresponding SPE and hence, the strength of depolarization (CDE) and excitonic (SDE) shift.*

is easily conceivable. A further explanation may be found in the homogeneous broadening, which implicates every measured peak. Starting with the uncertainty principle for energy and time, $\Delta E \Delta t \geq \hbar/2$, one arrives with $\Delta E = FWHM/2$ at the relation $FWHM \geq \hbar/\Delta t$. Lifetime measurements of intersubband excitations in GaAs quantum wells with a subband spacing above the LO phonon energy achieved lifetimes of $\Delta t \leq 1$ ps [Tat89, Fai93], which is in good agreement with theoretical predictions [Fer89]. An estimation would consequently lead to a broadening of ≈ 0.6 meV. In our case, a slightly faster relaxation with a lifetime below 1 ps may be assumed, because the SPE energy exceeds the 2-LO-phonon energy and the scattering on phonons describes the dominant relaxation mechanism. However, this estimation suggests that the homogeneous broadening may not account exclusively for the broad peak in the 12 nm-wide quantum well, since very low lifetimes below 0.2 ps are not quite reasonable.

If we return to Fig. 3.12 once again, we can identify a very weak and unusually broad manifestation of collective modes in the spectra. This observation matches very well with the study of Unuma et al. concerning intersubband transitions in 2DES with different well widths [Unu04]. They found strong collective modes in an 18 nm quantum well, but by decreasing the well widths, the charge and spin waves became weaker and weaker until they vanished at a width of around 10 nm. For even narrower quantum wells, only the single-particle transition remains. An explanation for this fading behavior of collective excitations could not be delivered in Ref. [Unu04], however, a possible approach would be the following: In a macroscopic picture, collective CDE and SDE modes are characterized by a coherent motion of electrons. This coherence may be more and more destroyed as the scattering events get stronger. The smaller the quantum well width, the stronger the scattering on fluctuations and consequently, the lower is the possibility of a coherent motion of electrons.

Intersubband transitions with an applied gate voltage

In the last small part of this chapter we consider intersubband transitions of a 12 nm-wide quantum well under the influence of an external electric field. Selected spectra of sample B* for a fixed laser energy of $E_L = 1.66$ eV and a gate

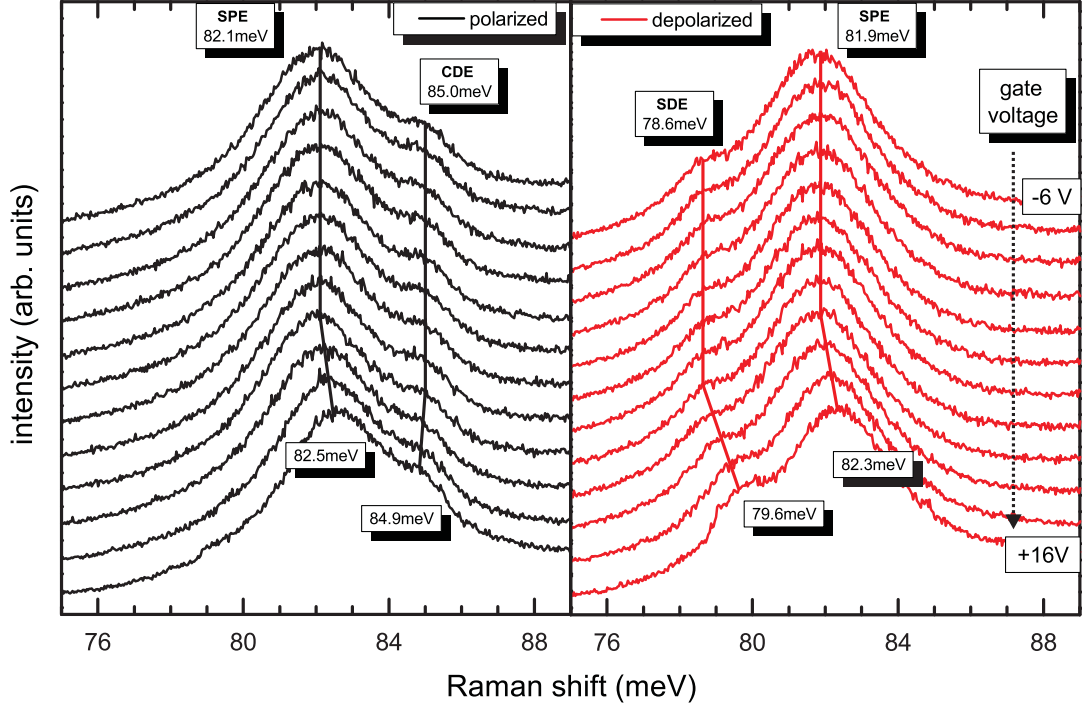


Figure 3.13: Selected spectra for intersubband transitions in sample B^* with equidistant steps of an applied gate voltage between -6 and $+16$ V. The intensities are vertically shifted to provide a better presentation of each spectrum. Additional lines serve as a guide to the eye.

voltage range between -6 and $+16$ V are plotted in Fig. 3.13. The solid lines are a guide to the eye and represent the shifting of the regarded excitations. No considerable modification of the investigated transitions is observable in the upper spectra ranging from -6 to approximately $+8$ V. Although sample B^* stems from the same wafer as sample B , small variations in well widths may occur and a slightly larger subband spacing around 82 meV for the region around zero gate voltage is not contradictory to previous results. However, there also appears a slight deviation of SPE energy between polarized and depolarized scattering geometry, which may be explained by an incoherent motion of electrons with an undefined phase correlation for both single-particle transitions.

Focusing on the progression of the SPE for higher gate voltages, a total blueshift of 0.4 meV is identifiable in both configurations. Nevertheless, the minor order of magnitude for the changed subband spacing reveals the marginal influence of an electric field induced by an external gate. From PL measurements, we can assume a maximum drop of carrier density by 20% within the studied voltage range. Consequently, the behavior of the collective modes in the voltage region between $+10$ and $+16$ V may be explained by regarding two different influences: For the spin-density wave, the excitation is dragged towards higher energies, since the subband spacing rises. This movement is additionally enhanced by the simultaneously dropping carrier density, which induces a reduction of the excitonic shift after Eq. (3.9) and hence, an approaching of the SDE to the SPE. On the con-

trary, these two effects are opposed for the charge-density wave. The increasing subband spacing triggers a blueshift, while the decreasing carrier density pushes the CDE through the reduced depolarization shift towards the SPE. Obviously, these two influences are almost balanced here, which leads to a nearly constant plasmon energy throughout the investigated voltage range.

To give a summery, we examined in the last section the intersubband transitions of a 12 nm-wide quantum well and observed an increased subband spacing as well as a decreased manifestation of collective modes compared to sample C, which has a larger well width. The further broadening of the single-particle transition is mainly ascribed to energy variations originating from microscopic fluctuations of the well width. Furthermore, measurements with an external gate revealed a rather small influence of an applied electric field on the existing subband structure. Despite a relatively large gate voltage, PL traces suggested a total carrier density variation up to 20 % only. This may be attributed to leakage currents in measurements with strong laser illumination, which probably reduce the effective gate field. With this, we conclude the chapter about intersubband transitions and proceed to studies on excitations within a single subband.

Chapter 4

Spin-orbit coupling and the persistent spin helix

Spin-orbit interaction (SOI) has a major influence on the band structure of a semiconductor, as it lifts, e.g., the sixfold degeneracy of the valence band at the Γ -point. In general, the coupling effect can be visualized by means of a semiclassical picture, where a moving electron senses a surrounding electric field as a magnetic field. Considering an electron's rest frame, the positively charged nucleus describes an orbital motion around the electron and, according to Biot-Savart's law, this loop current generates a magnetic field [Jac99]. Consequently, the coupling between the electron spin and the emerging magnetic field is called spin-orbit interaction. In special relativity, the term of the spin-orbit interaction can be derived directly from the Dirac equation and has the general form [Fab07]

$$H_{SO} = \frac{\hbar}{4m_0^2c^2} \mathbf{p} \cdot (\boldsymbol{\sigma} \times \nabla V) , \quad (4.1)$$

with the free electron mass m_0 , the velocity of light c and the canonical momentum \mathbf{p} . The cross product between the vector of the Pauli matrices $\boldsymbol{\sigma} = (\sigma_x, \sigma_y, \sigma_z)$ and the gradient of the electric potential V represents the described spin-orbit coupling. In the case of non-relativistic quantum mechanics, the SOI is simply taken into account by extending the Schrödinger equation with the depicted Hamiltonian. For isolated atoms, V would refer to the Coulomb potential arising from the nucleus and core electrons, whereas in solids, the interaction is based on the coupling of the electron spin to the average electric field emerging from the periodic crystal potential.

A crucial impact on the spin-orbit interaction of a semiconductor can be attributed to its prevalent symmetry. In semiconductors with space inversion symmetry, such as silicon or germanium, the energy states are spin degenerated for any possible momentum \mathbf{k} :

$$E_{\uparrow}(\mathbf{k}) = E_{\downarrow}(\mathbf{k}) \quad (4.2)$$

In fact, this equation holds only if the addressed space inversion symmetry ($E_{\uparrow,\downarrow}(\mathbf{k}) = E_{\uparrow,\downarrow}(-\mathbf{k})$) as well as the time inversion symmetry ($E_{\uparrow}(\mathbf{k}) = E_{\downarrow}(-\mathbf{k})$), also denoted as Kramers doublets, is fulfilled. Hence, the spin degeneracy can be removed in two possible ways. The time inversion symmetry can be broken by an external magnetic field, which separates the spin subbands along the energy axis. This is known as Zeeman effect. On the contrary, the space inversion symmetry is already broken for non-centrosymmetric crystals, such as semiconductor compounds like GaAs or InAs, resulting in a horizontal splitting of the subbands¹⁸. Consequently, the lack of inversion symmetry can induce a spin-orbit interaction, which lifts the remaining spin degeneracy even in the absence of an external magnetic field. Similar to the Zeeman splitting, the spin-orbit Hamiltonian for semiconductors with a broken spatial inversion symmetry may be expressed as

$$H_{SO} = \frac{\hbar}{2} \boldsymbol{\sigma} \cdot \boldsymbol{\Omega}_{\mathbf{k}}, \quad (4.3)$$

where $\boldsymbol{\Omega}_{\mathbf{k}}$ is the Larmor frequency, which describes the \mathbf{k} -dependent effective magnetic field of the SOI.

In the following, the different origins of this $B = 0$ spin splitting in a 2DES will be clarified in detail. After introducing fundamental basics, the particular impact of the spin splitting on electronic Raman scattering is discussed for (001)- and (110)-grown quantum wells, accompanied by the corresponding results on intrasubband transitions.

4.1 Origin of the $B = 0$ spin splitting

In low-dimensional semiconductors of zinc-blende type, we can distinguish between three different contributions, which break the space inversion symmetry and cause a $B = 0$ spin splitting: The bulk inversion asymmetry (BIA), also known as Dresselhaus effect [Dre55], arises due to a lack of inversion symmetry in the crystal lattice. A second contribution, denoted as Rashba effect [Byc84], emerges if a structure inversion asymmetry (SIA) is present in the sample and stems, e. g., from electric fields induced by modulation doping or external gates. The third mechanism for spin splitting occurs through interfaces of heterostructures, where contiguous layers share no common atom [Kre96, Win03, Dya08]. Usually, the impact from this natural interface asymmetry (NIA) is rather small and often neglected, since it behaves similar to BIA. Moreover, this contribution is absent for GaAs/AlGaAs heterostructures as both layers share a common arsenide anion, and hence, NIA is of no further interest here.

In general, the spin splitting of a (001)-grown quantum well depends on \mathbf{k}_{\parallel} and is anisotropic within the k_x - k_y plane. Jusserand et al. and Richards et al. demonstrated in several pioneering works the anisotropy of the spin splitting in the conduction band of GaAs/AlGaAs quantum wells by resonant inelastic light scattering on spin-flip intrasubband transitions [Jus92, Ric93, Jus95, Ric96]. But

¹⁸In fact, a given space inversion symmetry may also be lifted by an external magnetic field.

the impact of spin-orbit interaction is not limited to the conduction band, also the anisotropic spin-split hole dispersion in the valence band was proven by electronic Raman scattering in p-modulation-doped two-dimensional hole systems [Hir11]. Another approach to spin-orbit coupling in nanostructures is provided by photocurrent measurements from Ganichev et al. [Gan01, Gan02, Gan04, Gig07]. They deduced the ratio of Rashba and Dresselhaus coefficients by employing the spin-galvanic and the circular photogalvanic effect to semiconductor quantum wells.

Besides an anisotropic spin splitting for quantum wells based on zinc-blende structure, a huge spin-dephasing anisotropy was predicted for electrons of a 2DES with an in-plane spin orientation [Ave99]. An experimental proof was demonstrated by polarization-resolved photoluminescence [Ave06] and time-resolved Kerr rotation [Liu07, Sti07], revealing a strong spin dephasing for one in-plane direction and a weak relaxation for the perpendicular direction. Depending on the relative strengths of Rashba and Dresselhaus fields, this anisotropic behavior can be modified [Kai03], while a maximal anisotropy is achieved for a balanced ratio. In 2003, Schliemann et al. proposed a spin-field-effect transistor, which utilizes this unique feature to provide a nonballistic spin transport [Sch03].

In recent years, the distinct case of equal Rashba and Dresselhaus coupling constants gained more and more interest as a special situation arises: For a balanced ratio, a new type of $SU(2)$ spin rotation symmetry, which is generally broken by spin-orbit interaction, was theoretically proposed by Bernevig et al. [Ber06]. This symmetry entails very long spin lifetimes for a certain wave vector and leads to the formation of a persistent spin helix (PSH). The first experimental evidence was reported in 2009 by lifetime measurements with transient spin-grating spectroscopy [Kor09], followed by a direct mapping of the PSH state via time- and spatially resolved Kerr microscopy [Wal12a]. Furthermore, magnetotransport measurements on InGaAs quantum wells have shown that this special symmetry is controllable by an external gate, while the PSH state is indicated through the weak localization effect [Koh12].

Within this chapter, we will demonstrate the persistent spin helix state in a GaAs/AlGaAs quantum well with resonant inelastic light scattering (RILS) on spin-density excitations [Sch14]. Contrary to the above addressed methods, the $SU(2)$ symmetry is verified here through the spin splitting in the conduction band, which should reveal a maximum anisotropy in the crystallographic axes ($[110]$ and $[1\bar{1}0]$) for equal strengths of Rashba and Dresselhaus coupling constants.

4.1.1 Bulk inversion asymmetry

The spin-orbit interaction due to the lack of inversion symmetry in crystals with zinc-blende structure was proposed theoretically by G. Dresselhaus in 1955 [Dre55]. Without an inversion center, only the Kramers doublets remain and the spin degeneracy is lifted already for bulk materials. The corresponding spin-orbit Hamiltonian for the conduction band is obtained by an expansion according to

perturbation theory, while cubic-in- \mathbf{k} terms appear in the first place, since linear terms are forbidden due to symmetry reasons [Dre55]:

$$H_D^{3D} = \gamma_c [\sigma_x k_x (k_y^2 - k_z^2) + \sigma_y k_y (k_z^2 - k_x^2) + \sigma_z k_z (k_x^2 - k_y^2)] , \quad (4.4)$$

Here, the axes are defined along the standard cubic crystallographic directions ($x \parallel [100]$, $y \parallel [010]$, $z \parallel [001]$) and the material-specific Dresselhaus parameter γ_c is given by [Dya71a, Zut04]

$$\gamma_c = -\frac{\kappa_D \hbar^2}{2m^* \sqrt{2m^* E_g}} . \quad (4.5)$$

Consequently, the strength of the Dresselhaus SOI in a 3D system depends on the effective electron mass, the size of the band gap and a dimensionless parameter, which was determined as $\kappa_D = 0.07$ for moderately n-doped bulk GaAs [Mar83].

Proceeding to lower dimensional electron systems, the wave function gets confined and the momentum is quantized along the growth direction. Considering a quantum well of width d_{qw} , where only the lowest subband is occupied by electrons, k_z and k_z^2 are replaced by their expectation values $\langle k_z \rangle = 0$ and $\langle k_z^2 \rangle = (\pi/d_{qw})^2$. As a result of the quantization, the Dresselhaus field now differs in shape and orientation for various growth directions. In the following, we discuss two cases, which are relevant for this work and also the most common ones.

Dresselhaus field in a (001)-grown quantum well

For a (001)-grown quantum well, the spin-orbit Hamiltonian due to bulk inversion asymmetry reads

$$H_D^{2D} = \underbrace{\beta(\sigma_x k_x - \sigma_y k_y)}_{\text{linear in } \mathbf{k}} + \underbrace{\gamma_c(\sigma_x k_x k_y^2 - \sigma_y k_y k_x^2)}_{\text{cubic in } \mathbf{k}} , \quad (4.6)$$

where $\beta = -\gamma_c \langle k_z^2 \rangle$ denotes the linear Dresselhaus parameter. Studies with time-resolved Kerr rotation on various (001)-grown GaAs quantum wells verified the linear correlation between bulk and linear Dresselhaus parameters, and obtained $\gamma_c = (-11 \pm 2) \text{ eV \AA}^3$ for well widths between 6 and 30 nm [Wal12b]. As indicated, the confinement potential separates the Hamiltonian into a contribution linear, and a contribution cubic in \mathbf{k} . Focusing on the linear part, the Larmor frequency in the effective magnetic field description introduced by Eq. (4.3) can be written as

$$\Omega_D^{lin} = \frac{2\gamma_c}{\hbar} \langle k_z^2 \rangle \begin{pmatrix} -k_x \\ k_y \\ 0 \end{pmatrix} = \frac{2\gamma_c}{\hbar} \begin{pmatrix} -\langle k_z^2 \rangle k \cos \varphi \\ \langle k_z^2 \rangle k \sin \varphi \\ 0 \end{pmatrix} , \quad (4.7)$$

with the in-plane wave vector $k = \sqrt{k_x^2 + k_y^2}$ composed of $k_x = \cos \varphi$ and $k_y = \sin \varphi$, while φ defines the angle between \mathbf{k} and $x \parallel [100]$. The resulting spin splitting, induced by the linear Dresselhaus field, is given by

$$\Delta E_D^{lin} = \hbar \Omega_D^{lin} = 2\gamma_c \langle k_z^2 \rangle k = -2\beta k. \quad (4.8)$$

Note that $2\beta k$ has a positive value since γ_c is negative for GaAs [Wal12b]. Within effective mass approximation, the corresponding electron dispersion is described by a revolution of two rotating parabolas, which are symmetrically shifted around the energy axis. This dispersion is schematically illustrated in Fig. 4.1 (a), whereas (b) depicts a contour of constant energy in the k_x - k_y plane. Here, the colored arrows indicate the orientation of the in-plane spins, aligned by the linear Dresselhaus field.

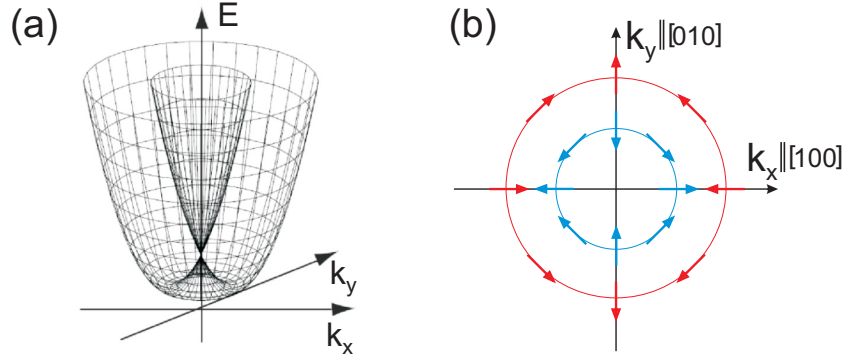


Figure 4.1: (a) Schematic band structure of a 2DES including SOI with \mathbf{k} -linear terms from the Dresselhaus field only. Taken from [Ivc05]. (b) Illustration of the corresponding spin orientation for electrons at the Fermi surface.

So far only the linear part of the Dresselhaus Hamiltonian was considered, but the cubic terms may also affect the band structure. Using trigonometric functions, the second part of Eq. (4.6) can be expressed by first- and third-order harmonics of the angle φ . A detailed derivation of the cubic Dresselhaus field may be found in [Sch12, Lec12], here, we only focus on the outcome and the corresponding impact on the spin splitting.

If the terms from the cubic and the linear part are combined, the total Larmor frequency appears as [Ivc05]

$$\Omega_D = \frac{2\gamma_c}{\hbar} \begin{pmatrix} -\Omega_1 \cos \varphi - \Omega_3 \cos 3\varphi \\ \Omega_1 \sin \varphi - \Omega_3 \sin 3\varphi \\ 0 \end{pmatrix} \quad (4.9)$$

with

$$\Omega_1 = k (\langle k_z^2 \rangle - \frac{1}{4}k^2) \quad \text{and} \quad \Omega_3 = \frac{1}{4}k^3. \quad (4.10)$$

Compared with the Larmor frequency in Eq. (4.7), a renormalization of the linear Dresselhaus field can be observed and an additional contribution proportional to third-order harmonics emerges. The resulting spin splitting, involving linear- and cubic-in- \mathbf{k} terms, is now anisotropic and can be written as [Epp88, Win03]

$$\Delta E_D = 2\gamma_c k \sqrt{\langle k_z^2 \rangle^2 - (\langle k_z^2 \rangle - \frac{1}{4}k^2)k^2 \sin^2(2\varphi)} . \quad (4.11)$$

This angular anisotropy in the conduction band was experimentally verified by B. Jusserand et al. in 1995 [Jus95]. They investigated the in-plane spin splitting of a highly doped GaAs/AlGaAs quantum well with spin-flip intrasubband transitions using inelastic light scattering.

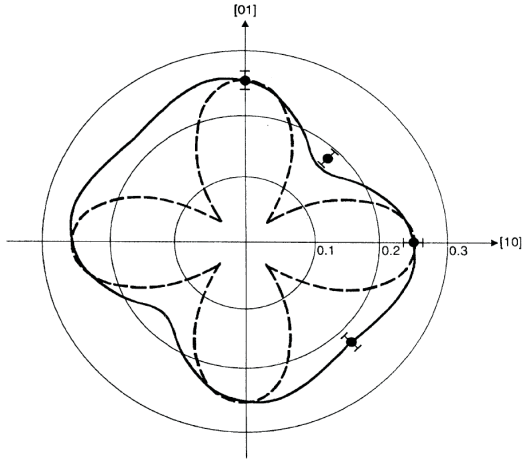


Figure 4.2: Angular variation of the spin splitting due to Dresselhaus field (dashed line) and total SO field (including Rashba field, solid line). Experimental values are represented by dots. Taken from [Jus95].

Figure 4.2 demonstrates the angular variation of the spin splitting, while the dashed line corresponds to the expected four-fold symmetry due to linear and cubic Dresselhaus terms and the dots represent experimental values. The discrepancy between theoretical and measured spin splitting can be attributed to a superposition with the Rashba field, which will be discussed in the following section. Nevertheless, the anisotropy of the spin splitting induced by the Dresselhaus field is still observable, even though it is experimentally weakened by the contribution of the Rashba term.

Under experimental conditions, the cubic-in- \mathbf{k} term of the Dresselhaus field is often neglected since this contribution is only important for high electron energies corresponding to high temperatures or a large carrier concentration [Ivc05]. In our samples, the electron density is 2–3 times lower compared to the heterostructures in Ref. [Jus95], and all measurements are carried out at very low temperatures. Therefore, we expect a nearly isotropic Dresselhaus field, dominated by the linear-in- \mathbf{k} terms, and a rather small anisotropic contribution of cubic-in- \mathbf{k} terms, which are not of further interest then.

Dresselhaus field in a (110)-grown quantum well

As already addressed above, the Dresselhaus field of (110)-grown quantum wells differs from the one obtained with a quantization axis along the (001)-direction. For a coordinate system with $x \parallel [\bar{1}10]$, $y \parallel [001]$, $z \parallel [1\bar{1}0]$ and φ defined as the angle between \mathbf{k} and $[1\bar{1}0]$, the Dresselhaus field can be written as [Ivc05]

$$\mathbf{\Omega}_D = \frac{\gamma_c}{\hbar} \begin{pmatrix} 0 \\ 0 \\ \Omega_1 \cos \varphi - \Omega_3 \cos 3\varphi \end{pmatrix} \quad (4.12)$$

with

$$\Omega_1 = k \left(\langle k_z^2 \rangle - \frac{1}{4} k^2 \right) \quad \text{and} \quad \Omega_3 = \sqrt{\frac{3}{4}} k^3. \quad (4.13)$$

Again, we can neglect the contribution from the cubic-in- \mathbf{k} terms and end up with the linear Dresselhaus field for (110)-grown quantum wells:

$$\mathbf{\Omega}_D^{lin} = \frac{\gamma_c}{\hbar} \langle k_z^2 \rangle \begin{pmatrix} 0 \\ 0 \\ k_x \end{pmatrix} \quad (4.14)$$

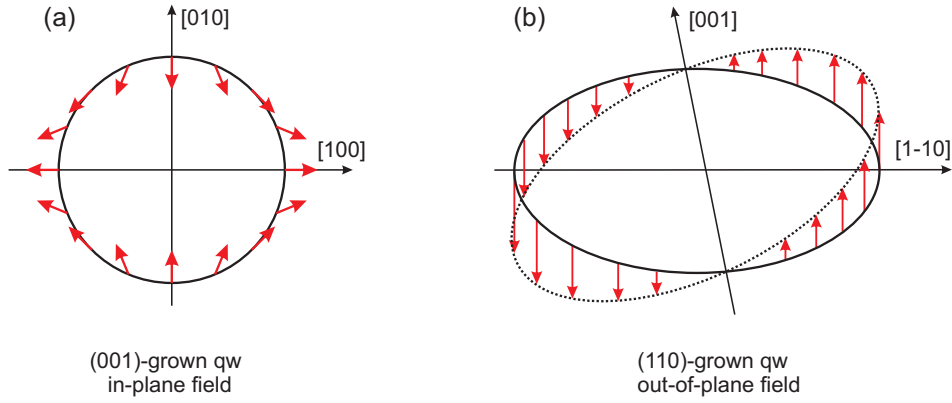


Figure 4.3: Schematic picture of the Dresselhaus spin-orbit field for two different electron systems. In a (001)-grown quantum well (a), the field features only in-plane components, whereas in (110)-grown structures (b), the SO field is oriented out of plane along the growth direction.

Here, the Dresselhaus field is not oriented in plane, but points out of plane parallel or antiparallel to the quantization axis for all possible wave vectors. A schematical picture of the field orientation is illustrated in Fig. 4.3, where it is compared to the linear Dresselhaus field in a (001)-grown quantum well system. This elucidates that the shape and orientation of the spin-orbit field induced by bulk inversion asymmetry strongly depends on the growth direction of the investigated 2DES.

4.1.2 Structure inversion asymmetry

In low-dimensional semiconductors, a second contribution to the SO field may emerge if an electric field E_z is present in the confined region [Ras60, Byc84]. This electric field can be induced by any kind of structure inversion asymmetry like asymmetrically shaped quantum wells or an asymmetrical modulation doping, but is not related to the crystal lattice. Similar to BIA, the Rashba field may be considered as an effective magnetic field and expressed as

$$\mathbf{\Omega}_R = \frac{2\alpha_R E_z}{\hbar} \begin{pmatrix} k_y \\ -k_x \\ 0 \end{pmatrix} = \frac{2\alpha}{\hbar} \begin{pmatrix} k_y \\ -k_x \\ 0 \end{pmatrix}, \quad (4.15)$$

where $\alpha = \alpha_R E_z$ denotes the Rashba parameter. Using the extended Kane model, the material parameter α_R for GaAs is determined as $5.2 \text{ e}\text{\AA}^2$ [Win03]. The corresponding spin splitting due to structure inversion asymmetry is linear in \mathbf{k} and given by

$$\Delta E_R = \hbar \Omega_R = 2\alpha_R E_z k = 2\alpha k. \quad (4.16)$$

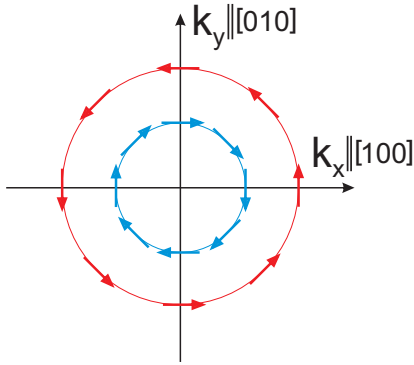


Figure 4.4: *Spin orientation of electrons at a contour of constant energy if only SIA is present. Here, a positive Rashba parameter is assumed, while the spins would be flipped for a negative value.*

Analog to the linear Dresselhaus field, the electron dispersion including only Rashba terms consists of a revolution of two rotating parabolas (see Fig. 4.1 (a)), but the effective magnetic field, and hence, the orientation of the in-plane spins differs. Since a dependency of the Rashba field on the growth direction does not exist, a spin orientation as sketched in Fig. 4.4 is valid for any given quantum well system. In fact, the SO field is oriented always in the quantum well plane and perpendicular to the electron in-plane \mathbf{k} -vector. In this figure, we assume a positive Rashba parameter, which can be attributed to a positive electric field, pointing along the growth direction (see, e.g., sample A). For an electric field antiparallel to the growth direction, as for instance induced by a dominant doping on the surface side of the 2DES (see sample B), the Rashba parameter becomes negative and the orientation of the effective field is reversed.

Such a linear dependency on the electric field opens attractive possibilities to manipulate SOI in semiconductor nanostructures, since it allows an external control by an electric gate. However, studies with different δ -doping positions have shown that if a vanishing Rashba field is desired, the electric field E_z can already be tuned to zero by a symmetrical distribution of doping layers [Olb09].

4.1.3 The persistent spin helix

In the previous sections we discussed how the spin degeneracy of the conduction band is lifted if either bulk inversion asymmetry or structure inversion asymmetry is present, but usually, an electron in a quantum well is subjected to both fields at the same time. For the following considerations, we restrict ourselves to linear terms in the spin-orbit Hamiltonian, since we can neglect the cubic-in- \mathbf{k} part of

the Dresselhaus field for good reasons. At first, we start with the discussion about a (001)-grown quantum well structure. In general, the spin splitting in the conduction band is anisotropic if both fields are taken into account, even in the absence of the cubic Dresselhaus contribution. For the very distinct case of equal Rashba and Dresselhaus coupling constants, however, an interesting situation arises as a new type of $SU(2)$ spin rotation symmetry is present [Ber06]. This symmetry leads to a helical spin mode, called the persistent spin helix (PSH), where a spin polarization, with an initial out of plane orientation, is predicted to resist any spin-independent scattering event. Hence, the net spin precession depends only on the net displacement in the propagation direction of the spin helix and is therefore independent of any other property of the electron's path, as, e.g., the initial momentum. This results in very long spin lifetimes up to 1 ns [Kor09], since common spin dephasing mechanisms like Dyakonov-Perel' [Dya71a, Dya71b] and Elliot-Yafet [Ell54, Yaf63] are suppressed. The conservation of spin polarization is a direct consequence of the effective magnetic field, which is unidirectional for every in-plane electron momentum. This spin-orbit field can be deduced from the corresponding Hamiltonian of an electron in a (001)-grown quantum well,

$$H_{SO}^{lin} = \alpha(k_y\sigma_x - k_x\sigma_y) + \beta(k_x\sigma_x - k_y\sigma_y) , \quad (4.17)$$

where only linear-in- \mathbf{k} terms are regarded and both, α and β , are assumed to be positive quantities. Here, we still use the standard convention for (001)-oriented nanostructures, denoting $x \parallel [100]$, $y \parallel [010]$ and $z \parallel [001]$. Using the Zeeman-like notation, the effective Larmor frequency is defined as

$$\Omega_{SO}^{lin} = \frac{2}{\hbar} \cdot [(\alpha k_y + \beta k_x)\mathbf{e}_x + (-\alpha k_x - \beta k_y)\mathbf{e}_y] . \quad (4.18)$$

For the discussed situation of balanced Rashba and Dresselhaus coupling constants, i.e., $\alpha = \beta$, the spin-orbit field reduces to

$$\Omega_{SO}^{lin} = \frac{2}{\hbar} \cdot \alpha \cdot (k_x + k_y)(\mathbf{e}_x - \mathbf{e}_y) . \quad (4.19)$$

As a consequence, the effective magnetic field for all \mathbf{k} is oriented either parallel or antiparallel to the $[1\bar{1}0]$ in-plane direction, which is determined by the sign of the sum $(k_x + k_y)$. The resulting band structure for equal Rashba and Dresselhaus coupling constants, together with the corresponding spin orientation at a contour of constant energy, is depicted in Fig. 4.5 (a) and (b).

Here, the electron dispersion is described by two energy paraboloids, which are symmetrically shifted around $k = 0$. Depending on the regarded paraboloid, the electron spins point either along the $[110]$ or the $[1\bar{1}0]$ -direction and the characteristic magnitude Δk for the paraboloid displacement is given by [Ber06]

$$\Delta k = \frac{4m^*\alpha}{\hbar^2} . \quad (4.20)$$

Furthermore, Δk may be considered as the PSH wave vector for an out-of-plane spin excitation and is connected via $\Delta k = 2\pi/\lambda_{PSH}$ to its wavelength λ_{PSH} . Assuming positive Rashba and Dresselhaus coupling constants (see Fig. 4.5 (b)), the

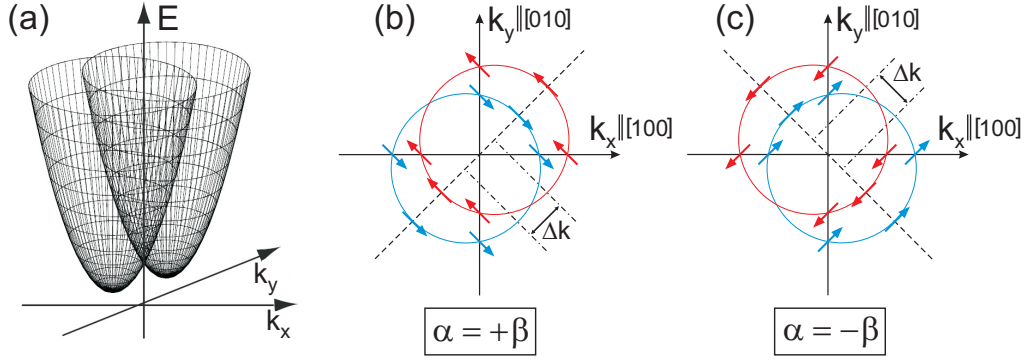


Figure 4.5: (a) Schematic electron band structure of a (001)-grown quantum well including SOI with a balanced ratio of Rashba and Dresselhaus coupling constants. Taken from [Ivc05]. The corresponding spin orientation at a contour of constant energy is unidirectional along $[1\bar{1}0]$ for $\alpha = +\beta$ (b) and along $[110]$ for $\alpha = -\beta$ (c).

spin splitting has a maximum in the $[110]$ -direction, while the splitting vanishes for the orthogonal in-plane direction. For electrons at the Fermi energy, the spin splitting $\Delta E_{S,[110]}$ can be determined by

$$\Delta E_{S,[110]} = \frac{\hbar^2}{m^*} k_F \Delta k, \quad (4.21)$$

where $k_F = \sqrt{2\pi N_s}$ describes the Fermi wave vector of the 2DES.

As we learned in the previous section, the Rashba SO field might have a negative parameter due to a negative electric field. The combined SO field for that case is still unidirectional, but now aligned to the orthogonal in-plane direction (see Fig. 4.5 (c)). Moreover, the energy paraboloids are shifted along the $[1\bar{1}0]$ -axis, which leads to a spin degeneracy for the $[110]$ -direction. Hence, the PSH can be established in a (001)-grown quantum well for two different configurations, sharing the same symmetries, but for different in-plane directions.

At this point, we need to address the contribution of the cubic Dresselhaus field again and spend a few more words on its impact on the PSH state. Generally speaking, the cubic-in- \mathbf{k} terms of the SO Hamiltonian may not be neglected for high electron energies or in materials with strong SO coupling, like InGaAs, and hence, represent a limiting factor for long spin lifetimes. Consequently, this influence destroys the above introduced model of the PSH with balanced Rashba and linear Dresselhaus parameters in the first place, however, experiments on magnetoconductance demonstrated a weak localization state in presence of strong cubic Dresselhaus terms, which indicates unambiguously a realization of the PSH [Koh12]. Additional calculations confirmed these experimental findings and revealed a PSH-type state for a system with strong cubic terms, although not at $\alpha = \beta$.

In (110)-oriented nanostructures, we face a whole new situation, because the Dresselhaus field differs in shape and orientation. For this growth direction, the bulk inversion asymmetry leads to a spin-orbit field, which points out of the quan-

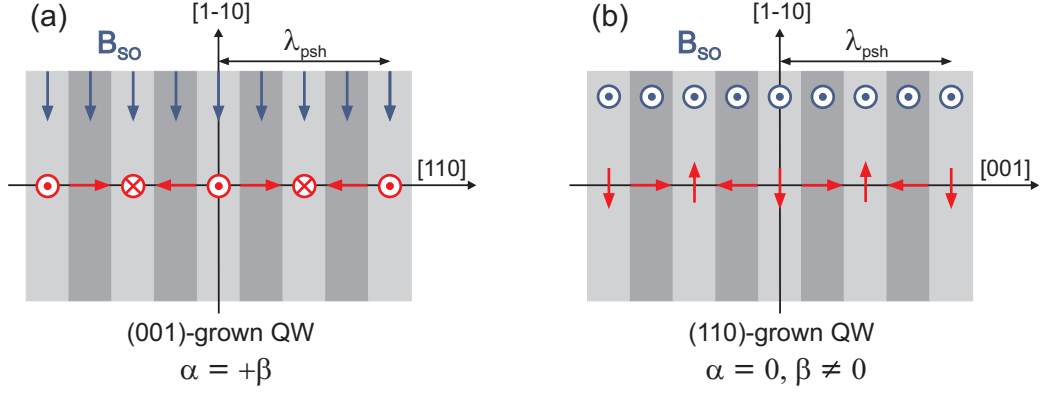


Figure 4.6: PSH model for a (001)- and a (110)-oriented quantum well system. The spin polarization of the helical spin mode, in red, is precessing around the magnetization axis of the unidirectional spin-orbit field, indicated in blue. Adapted from [Ber06].

tum well plane for every possible wave vector \mathbf{k} (see Fig. 4.3 (b)). Consequently, a spin helix symmetry can be achieved if the contribution of the Rashba field is tuned to zero, because a uniaxial effective field is already present from the Dresselhaus contribution. Although this symmetry is mathematically equivalent to the one proposed for (001)-grown nanostructures [Ber06], the manifestation of the PSH differs due to an out-of-plane SO field. As a consequence, the spin wave features only spin states with a polarization within the quantum well plane. The effective magnetic field and the corresponding helical spin mode for both growth directions is schematically sketched in Fig. 4.6. For a (001)-grown quantum well, the SO field is in-plane and forces an initially out-of plane excited electron spin to precess around its magnetization axis until it reaches its original orientation after the PSH wavelength λ_{PSH} . In an ideal picture without scattering, this precession continues infinitely. On the contrary, the effective field of a $SU(2)$ -symmetry points for a (110)-oriented nanostructure always out of the quantum well plane, which leads to a strictly in-plane precession of created spins with initial in-plane orientation.

Very recent publications have shown that these two models are not the end of the line in PSH research. Magneto-optical Kerr measurements demonstrated a further enhanced lifetime for the spin-polarization if the PSH direction is confined to a 1D wire structure [Alt14]. Simultaneously, a novel concept to determine the effective magnetic field direction and deduce absolute values for α and β without fitting parameters was presented [Sas14]. In fact, first approaches for two-dimensional hole gases revealed a signature of spin-preserving symmetries in heavy-hole subbands [Dol14], even though some required parameters are hardly accessible under experimental conditions.

To conclude this section, we discussed (001)- and (110)-grown quantum wells and found various types of spin helix symmetries for these semiconductor nanostructures. While a balanced ratio of Rashba and Dresselhaus coupling constants

($\alpha = \pm \beta$) is necessary for the PSH in (001)-oriented quantum wells, a unidirectional SO field and hence a signature of the PSH emerges in (110)-grown structures only for a vanishing Rashba contribution. In the following sections, we present an approach how this symmetry can be probed by inelastic light scattering and address the experimental limitation for a verification of the PSH in (110)-oriented heterostructures.

4.2 Intraband excitations in (001)-grown quantum wells

After we discussed how the band structure is influenced by different components of the spin-orbit field, we now draw our attention to particular applications of electronic Raman scattering. More than a decade ago Ullrich and Flatté investigated the impact of an effective magnetic field on collective intersubband excitations of GaAs quantum well systems [Ull02, Ull03]. They predicted a threefold, anisotropic splitting for the intersubband SDE dispersion if bulk and structure inversion asymmetry is present and emphasized the importance of many-body effects for this model. Recently, measurements on inelastic light scattering have proven these claims and revealed that the spectrum of the spin plasmon is split into a triplet through a giant collective SO field, which is enhanced by a factor of five compared to the SOI of individual electrons [Bab12]. Further studies considering intrasubband transitions in a CdMnTe quantum well underlined such an enhancement of SO fields for collective excitations due to many-body effects [Bab13]. But not only collective excitations provide an approach to the spin-orbit field, also Raman scattering on single-particle transitions may be employed to investigate the band structure of a quantum well. In the following, we demonstrate how the spin splitting, which features an unambiguous characteristic for a PSH state, can be probed by inelastic light scattering on intrasubband SDE.

4.2.1 Theoretical considerations

In a microscopical picture, the SDE features spin-flip and non spin-flip intrasubband transitions of individual electrons, which are coupled by exchange Coulomb interaction. Although energy renormalization due to collective effects might occur, an intrasubband SDE is usually regarded as an intrasubband single-particle excitation, since it is Landau damped for every possible wave vector (see Fig. 3.5) and interaction effects are typically small [Ber90]. Subsequently we will demonstrate that for a (001)-oriented 2DES with $\alpha = \beta$ only spin-flip transitions between states of opposite in-plane spin orientations are expected for depolarized scattering geometry. We start with the scattering amplitude deduced in the previous chapter and consider only the second term of Eq. (3.20), which is the relevant contribution for resonant inelastic light scattering on single-particle excitations:

$$\gamma_{fi} \propto \frac{1}{m} \sum_{\xi} \frac{\langle \psi_f | \mathbf{p} \mathbf{A}_S | \psi_{\xi} \rangle \langle \psi_{\xi} | \mathbf{p} \mathbf{A}_I | \psi_i \rangle}{E_i - E_{\xi} - \hbar \omega_I} \quad (4.22)$$

Here, $\psi_{i,f}$ represents the initial and final state, respectively, and ψ_{ξ} is the resonant intermediate state. If we use the band-edge Bloch functions and assume a constant band gap energy $E_0 = E_i - E_{\xi}$ for each possible transition, the scattering amplitude can be approximated as [Sch06]

$$\gamma_{fi} \propto \mathbf{e}_I \Pi_p \mathbf{e}_S \delta_{fi} + \Pi_d (\mathbf{e}_I \times \mathbf{e}_S) \langle \psi_f | \hat{\sigma} | \psi_i \rangle, \quad (4.23)$$

with

$$\Pi_p = \frac{2P^2}{3m} \cdot \frac{E_0}{E_0^2 - (\hbar \omega_I)^2} \quad \text{and} \quad \Pi_d = i \frac{2P^2}{3m} \cdot \frac{\hbar \omega_I}{E_0^2 - (\hbar \omega_I)^2}. \quad (4.24)$$

P is the interband dipole matrix element and $\hat{\sigma}$ the vector of the Pauli spin matrices. The prefactors $\Pi_{p,d}$ may be considered as constant, if the laser energy $\hbar \omega_I$ is fixed and the regarded Raman transitions are energetically small. We can identify two contributing parts, one with parallel polarization of incident and scattered light, which corresponds to scattering by charge-density fluctuations, and one with crossed polarization, originating from scattering by spin-density fluctuations [Ham69]. Since we are here only interested in spin-density excitations, the scattering amplitude for depolarized scattering geometry reduces to

$$A_{fi} = \Pi_d (\mathbf{e}_I \times \mathbf{e}_S) \langle \psi_f | \hat{\sigma} | \psi_i \rangle. \quad (4.25)$$

In exact backscattering geometry ($\theta = 0$), a nonzero contribution from the cross product between the polarization vector of the incident and scattered light is expected only for the z component, as the most simplified example demonstrates:

$$(\mathbf{e}_I \times \mathbf{e}_S) = (1, 0, 0) \times (0, 1, 0) = (0, 0, 1)$$

This restriction holds as long as both polarization vectors have zero z components, but will be softened by a finite tilt angle θ . However, an approximation of vanishing x and y components is still reasonable due to the large difference in the refraction indices of GaAs (~ 3.6) and vacuum. If we choose the [001] direction (z -axis) as the quantization axis of the spin, the spin-dependent part $\psi_{\pm \mathbf{k}}$ of the electron wave function for spin orientations in the quantum well plane is given by [Mal97]

$$\psi_{\pm \mathbf{k}} = \frac{1}{\sqrt{2}} e^{-i\phi_k/2} [|\uparrow\rangle \pm e^{i\phi_k} |\downarrow\rangle], \quad (4.26)$$

where ϕ_k is the angle between the direction of the spin-orbit field and the [100] direction (x -axis). The spin eigenvectors $|\uparrow\rangle = (1, 0)$ and $|\downarrow\rangle = (1, 0)$ represent the parallel and antiparallel projection of the electronic spin onto the z direction, respectively. For a system with $\alpha = \beta$, where both coupling constants are presumably positive (see Fig. 4.5 (b)), a unidirectional spin-orbit field with $\phi_k = -45^\circ$

or 135° is obtained and the two possible eigenfunctions for in-plane spins read [Sch14]

$$\psi_{\pm\mathbf{k}} = \frac{1}{\sqrt{2}} e^{i\pi/8} \left[|\uparrow\rangle \pm \frac{1}{\sqrt{2}}(1-i) |\downarrow\rangle \right], \quad (4.27)$$

while the plus (minus) sign corresponds to a spin orientation parallel (antiparallel) to $[1\bar{1}0]$. Inserting this wave function into Eq. (4.25) and neglecting the marginal contribution from x and y components, the scattering amplitude for an intrasubband transition from a spin-down ($-, \phi_k = -45^\circ$) to a spin-up state ($+, \phi_k = 135^\circ$) can be deduced as follows:

$$\begin{aligned} A_{+-} &= \Pi_d \cdot \left\{ \frac{e^{i\pi/8}}{\sqrt{2}} \left[\begin{pmatrix} 0 \\ 1 \end{pmatrix} + \frac{1}{\sqrt{2}}(1-i) \begin{pmatrix} 1 \\ 0 \end{pmatrix} \right] \right\}^* \cdot \begin{pmatrix} 1 & 0 \\ 0 & -1 \end{pmatrix} \cdot \\ &\quad \cdot \left\{ \frac{e^{i\pi/8}}{\sqrt{2}} \left[\begin{pmatrix} 0 \\ 1 \end{pmatrix} - \frac{1}{\sqrt{2}}(1-i) \begin{pmatrix} 1 \\ 0 \end{pmatrix} \right] \right\} \\ &= \Pi_d \cdot \frac{e^{-i\pi/8}}{\sqrt{2}} \cdot \frac{e^{i\pi/8}}{\sqrt{2}} \left\{ \begin{pmatrix} 1 \\ 0 \end{pmatrix} + \begin{pmatrix} 0 \\ \frac{1}{\sqrt{2}}(1+i) \end{pmatrix} \right\} \cdot \begin{pmatrix} 1 & 0 \\ 0 & -1 \end{pmatrix} \cdot \\ &\quad \cdot \left\{ \begin{pmatrix} 1 \\ 0 \end{pmatrix} + \begin{pmatrix} 0 \\ -\frac{1}{\sqrt{2}}(1-i) \end{pmatrix} \right\} \\ &= \Pi_d \cdot \frac{1}{2} \begin{pmatrix} 1 \\ \frac{1}{\sqrt{2}}(1+i) \end{pmatrix} \begin{pmatrix} 1 & 0 \\ 0 & -1 \end{pmatrix} \begin{pmatrix} 1 \\ -\frac{1}{\sqrt{2}}(1-i) \end{pmatrix} \\ &= \Pi_d \cdot \frac{1}{2} \begin{pmatrix} 1 \\ \frac{1}{\sqrt{2}}(1+i) \end{pmatrix} \begin{pmatrix} 1 \\ \frac{1}{\sqrt{2}}(1-i) \end{pmatrix} \\ &= \Pi_d \cdot \frac{1}{2} \left[1 + \frac{1}{2} \cdot (1+i) \cdot (1-i) \right] \\ &= \Pi_d \cdot \frac{1}{2} [1 + \frac{1}{2} \cdot 2] \\ &= \Pi_d \end{aligned}$$

Calculations for the remaining possibilities are straightforward and reveal $A_{+-} = A_{-+} = \Pi_d$ for spin-flip and $A_{++} = A_{--} = 0$ for non spin-flip excitations. Consequently, only spin-flip transitions between different spin subbands have a finite possibility and contribute to the Raman signal.

Next, we consider the energy dispersion of the discussed system in more detail. Figure 4.7 displays a cut through the energy paraboloids in $[110]$ and $[1\bar{1}0]$ direction, respectively, together with its respective enlargement of the area around the Fermi energy. As expected from previous considerations, the parabolas in $[110]$ direction are spin-spitted by Δk (a), while the spin states along $[1\bar{1}0]$ are degenerated for every possible wave vector (c). If we take a closer look at the region around the Fermi energy and assume a fixed transferred wave vector q , we can create for the $[110]$ direction two possible spin-flip transitions with individual energies and the difference in the energy is exactly two times the energy of the spin splitting (see Eq. (4.21)). Note that transitions between split spin subbands are only possible for $\Delta k < q$. As deduced above, non spin-flip excitations may be

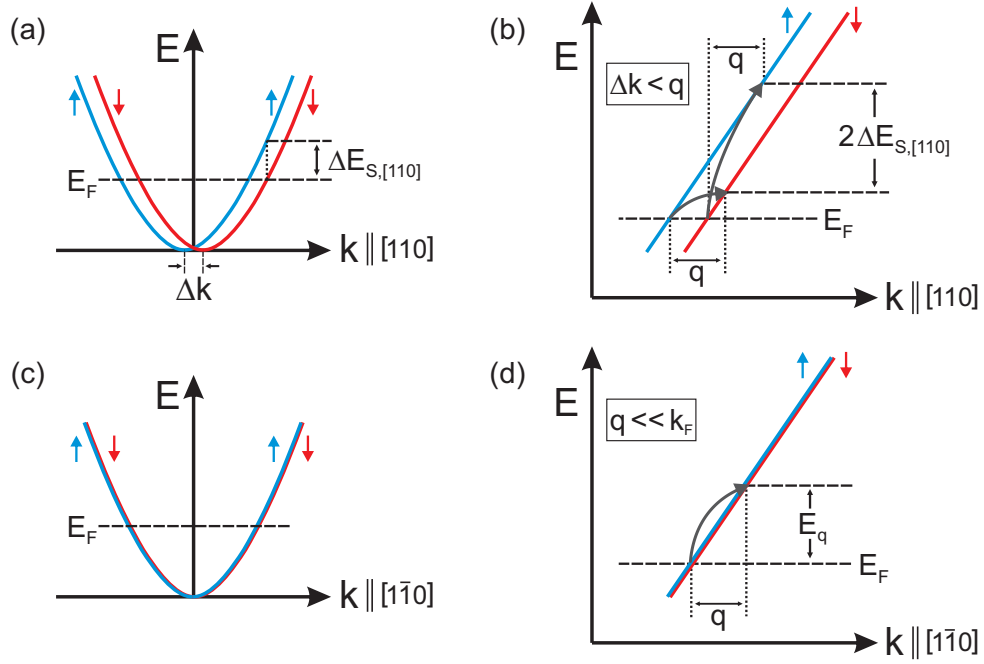


Figure 4.7: (a) Cut through the energy paraboloids in the $[110]$ in-plane direction. (b) Schematic enlargement of the area around the Fermi energy. Spin-flip intrasubband transitions for a fixed transferred wave vector q and $\Delta k < q$ are indicated by curved arrows. (c) and (d): Same consideration, but for a cut in the $[1\bar{1}0]$ direction, where the spin splitting is zero.

neglected in the Raman spectra under the given conditions. By contrast, for the $[1\bar{1}0]$ direction we can also find two possible excitations, but here both spin-flip transitions feature the same energy.

All depicted single-particle transitions of Fig. 4.7 (b) and (d) represent the high-energy cutoffs of the corresponding intrasubband spin-flip excitations for a given wave vector q [Sch14]. In fact, the electron dispersion in the k_{\parallel} -space is a two-dimensional paraboloid rather than a one-dimensional parabolic curve and thus, single-particle transition energies are actually given by a continuum for a defined wave vector q [Pin88a]. The resulting spectral shape of this continuum is described by the so called Lindhard-Mermin line shape for single-particle excitations [Fas87]. A characteristic feature is the sawtooth-like shape starting with a nearly linear increase of intensity at zero energy up to the addressed cutoff energy, where a very steep decrease of intensity is visible (see, e. g., the bottommost spectrum in Fig. 4.8 (b)).

These theoretical considerations so far are appropriate for a system with equal Rashba and Dresselhaus spin-orbit fields, where both coupling constants are assumed to be positive quantities ($\alpha = +\beta$). For quantum well systems with opposite signs in coupling constants ($\alpha = -\beta$), however, the discussion is fairly similar and leads to the same situation as sketched in Fig. 4.7, but with interchanged crystal directions. In other words, we would expect two possible spin-flip transitions with individual energies for a wave-vector transfer parallel to $[1\bar{1}0]$, whereas both excitations in the $[110]$ direction would reveal the same energy.

To emphasize the important facts of this section, we verified in the first place that in good approximation only spin-flip processes contribute to intrasubband spin-density excitations. Further considerations of the energy dispersion demonstrated an experimental approach to the spin splitting via inelastic light scattering. We expect for a balanced ratio of Rashba and Dresselhaus coupling constants two individual transitions for a wave-vector transfer parallel to the crystal direction, where the in-plane spin splitting has its maximum, while only a single transition energy should be present in the orthogonal in-plane direction. As already discussed in the previous section, the direction of the uniaxial spin-orbit field, which determines the orientation of the spin splitting, depends only on the relative signs of α and β .

4.2.2 Excitations in the regime of the persistent spin helix state

So far we developed the required background of the persistent spin helix and its associated peculiarities concerning electronic Raman scattering, in the following we aim to bridge the gap between theoretical expectations and experimental results. To that end, we start with the discussion about sample A, because a previous publication on a sample from the same wafer has shown via the magneto optical Kerr-effect that the persistent spin helix state and therefore the desired unidirectional spin-orbit field is fulfilled for this quantum well system [Wal12a]. The subsequent discussion mainly follows Ref. [Sch14].

Figure 4.8 shows the experimental results for electronic Raman scattering on intrasubband spin-density excitations, where the wave vector q is transferred either

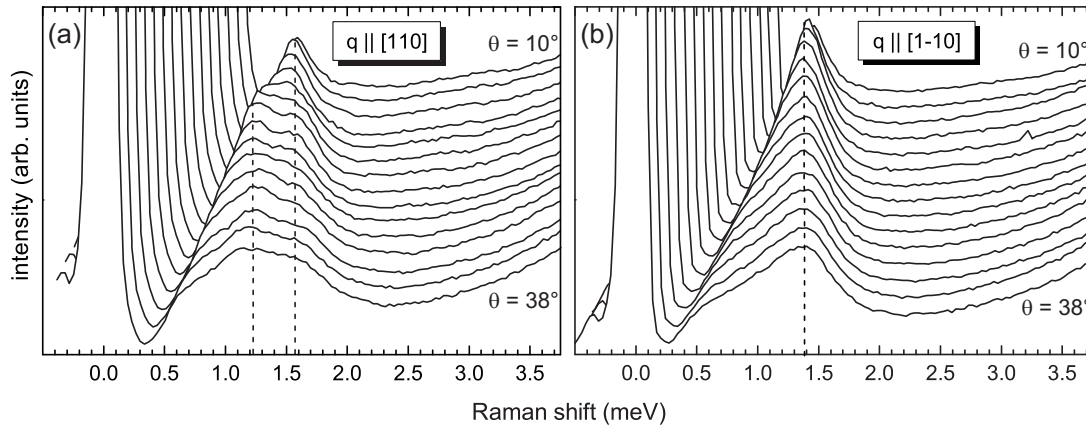


Figure 4.8: Waterfall plot of inelastic light scattering spectra from sample A for a fixed laser energy, measured at $T = 5.5$ K. A wave-vector transfer parallel to the $[110]$ (a) or the $[1\bar{1}0]$ in-plane direction (b) reveals the intrasubband SDE in depolarized scattering geometry. The transferred wave vector increases from $2.76 \times 10^6 \text{ m}^{-1}$ for the top spectra ($\theta = 10^\circ$) up to $9.79 \times 10^6 \text{ m}^{-1}$ for the bottom one ($\theta = 38^\circ$). A vertical and horizontal shift of single spectra provide a clearer overview.

along the $[110]$ direction (a), or parallel to $[1\bar{1}0]$ (b). Each plot contains a series of depolarized spectra for various tilt angles θ , ranging from $\theta = 10^\circ$ for the top spectra up to $\theta = 38^\circ$ for the bottom one. The laser energy was kept fixed and its strong amount of elastically scattered light is still visible at around zero Raman shift. Furthermore, the sharp cutoff in each spectra, located at about 0.5 meV in the bottom ones, can be attributed to the cutoff of the triple stage Raman spectrometer. All spectra except the ones for $\theta = 38^\circ$ have been shifted vertically and horizontally to provide a clear picture over the whole range. The dashed line is a guide to the eye and should emphasize the maxima in the spectra, which appear vertically in these plots through the horizontal shift. The increasing slope at the high energy side of the depicted spectral range stems from the photoluminescence of the fundamental band gap. Considering a single spectrum of Fig. 4.8 (b), the asymmetric Lindhard-Mermin line shape [Fas87] for single-particle intrasubband transitions is very well identifiable by the linear increase of intensity combined with a (relatively) sharp closure of the excitation. The corresponding high energy cutoff E_q , observable at around 1.6 meV in the bottom spectrum, depends linearly on the Fermi wave vector k_F and the transferred in-plane wave vector q ,

$$E_q = \frac{\hbar^2}{m^*} k_F q, \quad (4.28)$$

if a parabolic band and $q \ll k_F$ is assumed. This allows after Ref. [Fas87] an experimental estimation of the electron density in the quantum well via $N_s = k_F^2/(2\pi)$. The effective mass m^* was determined by inelastic light scattering measurements in a perpendicular magnetic field under similar experimental conditions, later discussed in Chap. 6. From cyclotron resonance excitations, we could extract $m^* = (0.075 \pm 0.001) m_e$ at the Fermi energy of the 2DES, which is somewhat larger than the nominal value of $m^* = 0.067 m_e$. Such a discrepancy is not unusual and probably due to a nonparabolicity of the conduction band [Eke89] and a finite penetration of the electron wave function into the barrier material. Hence, we get $N_s = (4.40 \pm 0.75) \times 10^{15} \text{ m}^{-2}$ for the carrier density from the analysis of Fig. 4.8 (b), which is slightly smaller than the presented value in Tab. 2.1. However, considering the facts that this estimation contains a reasonable error and that the compared value stems from transport measurements on a different sample, a difference of such extent is not unlikely. An additional deviation may be attributed to the strong illumination through the continuous-wave laser, which typically reduces the electron density of the quantum well through a redistribution of carriers between doping layers in the barrier and the 2DES.

If we focus again on the spectra in Fig. 4.8, we can identify a double-peak structure with a peak separation of about $(0.37 \pm 0.05) \text{ meV}$ for a wave-vector transfer parallel to $[110]$, while the orthogonal direction features only a single maximum. The peak distance in subframe (a) appears to be nearly independent of the transferred wave vector and the spectra closely resemble the characteristic shape of single-particle excitations reported on asymmetric GaAs quantum wells [Jus92, Ric93], even though the value of the peak separation deviates due to dif-

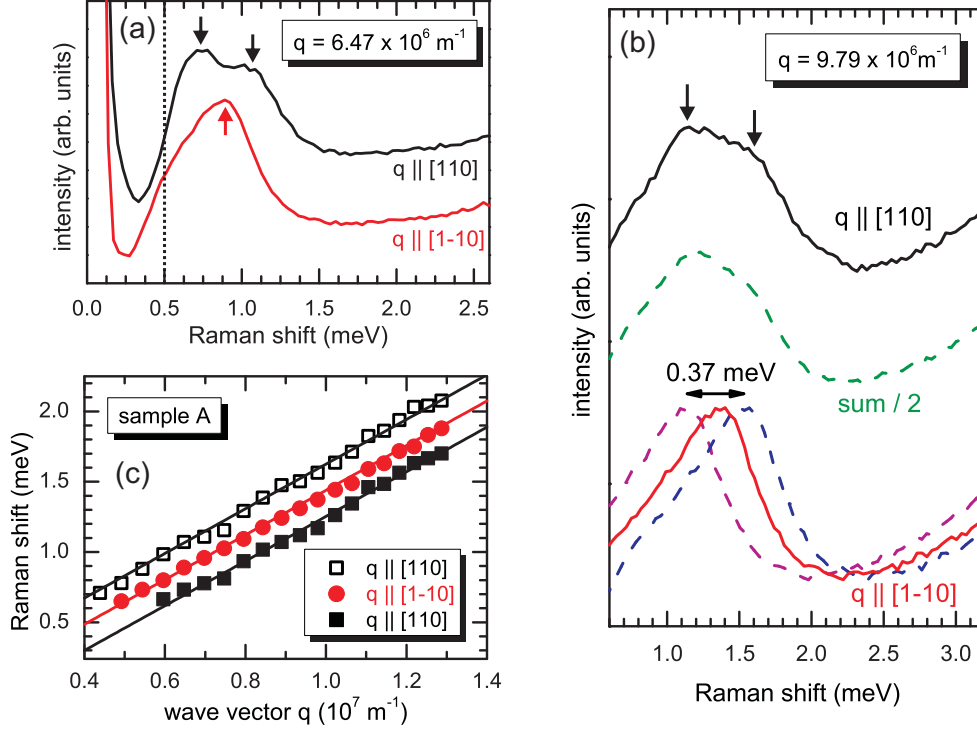


Figure 4.9: (a) Depolarized spectra of sample A with two different in-plane directions at a fixed wave-vector transfer of $q = 6.47 \times 10^6 \text{ m}^{-1}$. Arrows indicate the respective peak positions and the dashed line represents the cutoff frequency of the Raman spectrometer. (b) Same as (a) with a wave vector of $q = 9.79 \times 10^6 \text{ m}^{-1}$ (red and black solid lines). The spectra of blue and magenta dashed lines are reproductions of the red experimental spectrum, but equally shifted to higher and lower energies. The green dashed line represents the sum of both created curves divided by a factor of 2. (c) Extracted peak positions of the intrasubband SDE in the experimental spectra with respect to the transferred wave vector. The size of the symbols is representative for the experimental error. Solid lines should emphasize a constant peak separation.

ferent sample parameters. For the spectral position of the high-energy cutoff of both spin-flip transitions follows from the previous theoretical treatment

$$E_{\pm} = E_q \pm \Delta E_{S,[110]} , \quad (4.29)$$

which explains the equally shifted peak positions in Fig. 4.8(a) compared to the peaks in (b), where a single transition energy suggests a close to zero spin splitting.

For a simplified analysis we compare in Fig. 4.9(a) spectra from both depicted in-plane directions for a fixed transferred wave vector of $q = 6.47 \times 10^6 \text{ m}^{-1}$ ($\theta = 24^\circ$). The double-peak structure in the black curve is very well pronounced and the single peak for $q \parallel [1\bar{1}0]$ is energetically located in the center of the double peak (maxima indicated with small arrows). Again, the dashed line represents the cutoff frequency of the Raman spectrometer. The identified spectral behavior of the excitations clearly holds for moderate q , however, for higher transferred wave vectors an even closer inspection is required.

For that purpose, Fig. 4.9(b) depicts the related spectra measured at $q = 9.79 \times 10^6 \text{ m}^{-1}$. Even though the characteristic shape is identifiable in the experimental spectra (black and red solid lines), we can observe only a blurred double peak structure for the [110] direction. To verify our theoretical expectation, we try to recreate the measured black curve by processing the red one, which was recorded with a wave-vector transfer parallel to $[1\bar{1}0]$ and features presumably only a single cutoff energy. Hence, we duplicate the red curve and shift the created ones symmetrically by the experimentally extracted value of the peak separation. After both shifted spectra are summarized, we obtain the green dashed line, which represents an almost exact reproduction of the measured curve taken in the [110] direction. This is a strong evidence for the superposition of two intrasubband excitations with different cutoff energies (see Fig. 4.7(b)), even at higher transferred wave vectors, where the double-peak structure is not clearly visible at first sight. The simulated curve further confirms our assumption of balanced contributions between both spin-flip transitions, as deduced in the previous section for the scattering amplitudes $A_{+-} = A_{-+} = \Pi_d$, and justifies the neglect of an additional admixture with non spin-flip transitions occurring at finite tilt angles, at least within the depicted range up to $\theta \leq 38^\circ$. Here we can resume that our experimental findings match very well the theoretical expectations of a single cutoff energy in the $[1\bar{1}0]$ direction, caused by zero spin splitting, and two energetically separated excitations for the orthogonal direction, which are symmetrically displaced by $\pm \Delta E_{S,[110]}$.

Figure 4.9(c) shows the extracted peak positions for both scattering configurations as a function of the transferred wave vector q . This analysis also includes values obtained from spectra with a larger tilt angle as depicted in Fig. 4.8. The supplementary solid lines suggest the expected independence of the peak separation from the transferred wave vector and yield an experimentally detected spin splitting of $\Delta E_{S,[110]} = (0.18 \pm 0.05) \text{ meV}$.

Since we observe a double peak structure for the [110] and a corresponding single peak in the $[1\bar{1}0]$ direction, we might conclude that the ratio between Rashba and Dresselhaus coupling constants is nearly balanced in this sample. However, a further discussion of limitations in the analysis is thoroughly appropriate. In general, the spin splitting for a 2DES with Rashba and linear Dresselhaus contributions is given by

$$\Delta E_{S,[110]} = 2(\alpha + \beta)k_F \quad (4.30)$$

for the [110] direction, and

$$\Delta E_{S,[1\bar{1}0]} = 2(\alpha - \beta)k_F \quad (4.31)$$

for the $[1\bar{1}0]$ direction. If we use the obtained value for the spin splitting $\Delta E_{S,[110]}$ and $k_F = (1.66 \pm 0.18) \times 10^8 \text{ m}^{-1}$, which can be extracted from the analysis of the cutoff frequencies in the $[1\bar{1}0]$ direction, we receive $(\alpha + \beta)/2 = (2.77 \pm 0.83) \text{ meV \AA}$. In an ideal picture with $\alpha = \beta$, this value would quantify the strengths of both Rashba and Dresselhaus coupling constants. Compared to the determined

strength in Ref. [Wal12a] ($\alpha \approx 2.3 \text{ meV \AA}$, measured at $T = 40 \text{ K}$), we can notice a slight deviation, which can be attributed to a different sample piece or changed experimental conditions, since a strong laser illumination may induce a different electric field across the quantum well. A further reason for the discrepancy may be found in the finite spot size of the excitation [Sal14], which was not included in the analysis of Ref. [Wal12a], but causes a slightly too small estimation of Δk .

The obvious downside of our method to determine the spin-orbit fields is the accuracy of the peak distance extracted from the Raman spectra. After a careful inspection of all experimental data, it appears that we are not able to resolve a peak distance smaller than about 0.1 meV , which corresponds to a spin splitting of $\Delta E_S < 0.05 \text{ meV}$. By using Eq. (4.31), we can estimate $(\alpha - \beta) < 1.5 \text{ meV \AA}$ as an upper limit for the difference of Rashba and linear Dresselhaus coefficients. If we further include Eq. (4.30), the coupling constants $\alpha < 3.5 \text{ meV \AA}$ and $\beta > 2.0 \text{ meV \AA}$ follow as the limiting values in our experiments.

Assuming a balanced ratio of Rashba and Dresselhaus SO fields again, we can determine $\Delta k = (1.14 \pm 0.33) \times 10^6 \text{ m}^{-1}$ for the wave vector of the PSH and its corresponding wavelength as $\lambda_{PSH} = (5.5 \pm 1.5) \mu\text{m}$. This is in reasonable accordance to the measured PSH wavelength in Ref. [Wal12a], gained from a direct mapping with the magneto-optical Kerr effect for long time delays between pump and probe pulses.

4.2.3 Angular dependency of the spin splitting

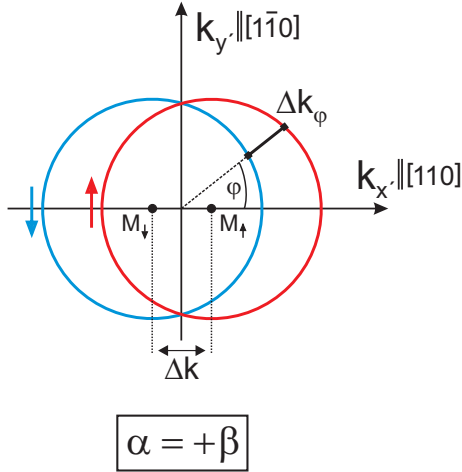


Figure 4.10: Fermi contour for a (001)-grown quantum well with $\alpha = +\beta$. The circles are displaced by Δk along the $[110]$ direction and the corresponding angular offset is given by Δk_φ .

In the previous section we have demonstrated how the spin splitting of a (001)-grown quantum well may be approached by inelastic light scattering on intrasubband spin-flip transitions. A sufficient criteria for a persistent spin helix state in the addressed system is a vanishing spin splitting for one in-plane direction, while simultaneously a splitting of spin states in the perpendicular direction of the quantum well plane is present. However, to confirm these results and complete the picture of the reciprocal space, an investigation of the spin splitting for additional in-plane directions is reasonable.

An illustration of the Fermi contour for a (001)-grown quantum well with equal Rashba and Dresselhaus coupling constants is depicted in Fig. 4.10. Here, the axes parallel to $[110]$ and $[1\bar{1}0]$ are denoted as $k_{x'}$ and $k_{y'}$, respectively, and both α and

β are assumed to be positive quantities, which results in a horizontal displacement of the Fermi contours by Δk . In the following, we deduce the magnitude of the angular offset Δk_φ of the Fermi contours for every possible in-plane direction.

The equation of a circle in Cartesian coordinates reads

$$(x - x_M)^2 + (y - y_M)^2 = r_k^2, \quad (4.32)$$

with the center coordinates (x_M, y_M) and the radius r_k . Introducing r as the radius from the origin and φ as the angle between an arbitrary and the [110] direction, the coordinates x and y can be expressed as $x = r \cdot \cos(\varphi)$ and $y = r \cdot \sin(\varphi)$. Hence, the equation of a circle in polar coordinates is given by

$$r^2 + r(-2x_M \cos(\varphi) - 2y_M \sin(\varphi)) + (x_M^2 + y_M^2 - r_k^2) = 0, \quad (4.33)$$

while a solution for the radius can be found with

$$r(\varphi) = x_M \cos(\varphi) + y_M \sin(\varphi) \pm \sqrt{r_k^2 - (x_M \sin(\varphi) - y_M \cos(\varphi))^2}. \quad (4.34)$$

Applying this formula to the considered situation of two circles with a unitary radius of $r_{k,\uparrow} = r_{k,\downarrow} = r_k$ and center coordinates $(-\frac{\Delta k}{2}, 0)$ for the spin-down and $(\frac{\Delta k}{2}, 0)$ for the spin-up contour, we obtain for the angular offset:

$$\begin{aligned} \Delta k_\varphi &= r_\uparrow(\varphi) - r_\downarrow(\varphi) \\ &= \frac{\Delta k}{2} \cos(\varphi) + 0 \pm \sqrt{r_k^2 - (\frac{\Delta k}{2} \sin(\varphi) - 0)^2} + \\ &\quad - [-\frac{\Delta k}{2} \cos(\varphi) + 0 \pm \sqrt{r_k^2 - (-\frac{\Delta k}{2} \sin(\varphi) - 0)^2}] \\ &= \frac{\Delta k}{2} \cos(\varphi) \pm \sqrt{r_k^2 - (\frac{\Delta k}{2} \sin(\varphi))^2} + \frac{\Delta k}{2} \cos(\varphi) \mp \sqrt{r_k^2 - (\frac{\Delta k}{2} \sin(\varphi))^2} \\ &= \Delta k \cos(\varphi) \end{aligned} \quad (4.35)$$

Note that the deduced expression is independent of the circle radius r_k as long as both circles are of the same size, what is assumed for the PSH state. According to Eq. (4.21), we get for the angular dependency of the spin splitting:

$$\Delta E_{S,\varphi} = \frac{\hbar^2}{m^*} k_F \Delta k \cos(\varphi) = \Delta E_{S,[110]} \cdot \cos(\varphi) \quad (4.36)$$

This means we expect a maximum splitting for the [110] direction ($\varphi = 0^\circ$), a vanishing splitting for the perpendicular $[1\bar{1}0]$ direction ($\varphi = 90^\circ$) and a cosine behavior for all directions in between. To verify these theoretical predictions, we probed the angular dependency of the spin splitting for three different tilt angles of $\theta = 25^\circ$, 35° and 45° . Some of the experimental results are summarized in Fig. 4.11. Subframe (a) shows the obtained Raman spectra in depolarized scattering geometry for $\theta = 35^\circ$. Each spectrum was measured with a different in-plane direction of the transferred wave vector q , corresponding to angles $\varphi = 0^\circ$, 30° , 60° and 90° with respect to the [110] direction. Again, the increasing

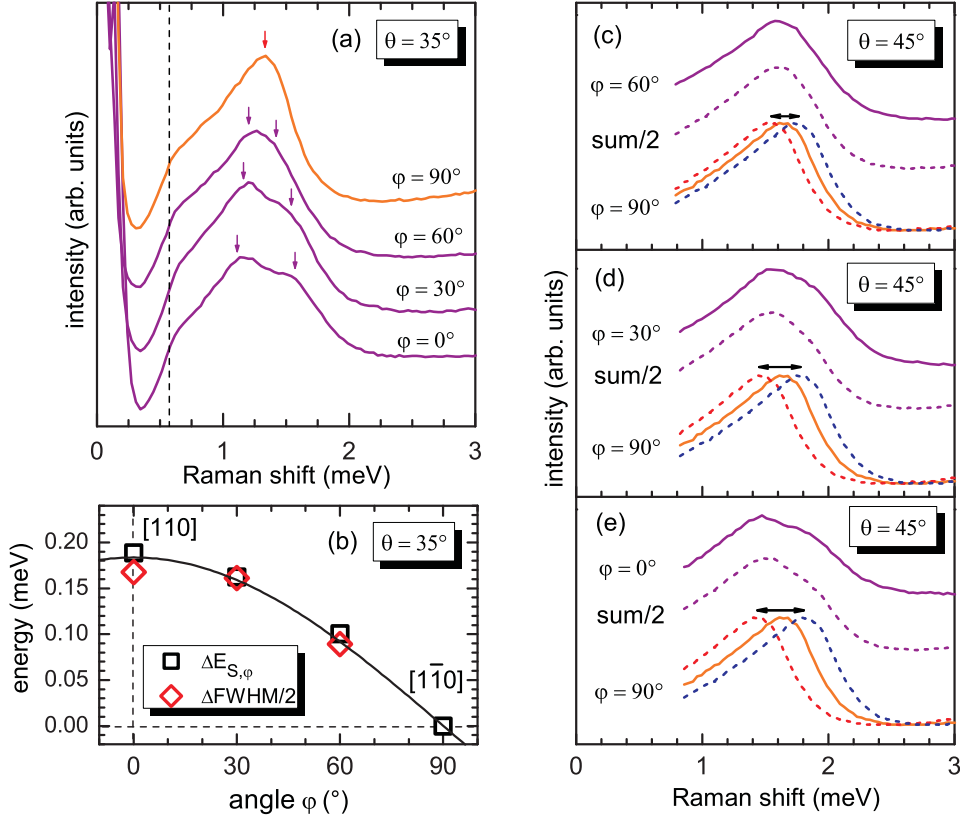


Figure 4.11: Depolarized Raman spectra at a tilt angle of $\theta = 35^\circ$ ($q = 9.1 \times 10^6 \text{ m}^{-1}$) for four different in-plane directions. (b) Extracted values for the angular dependent spin splitting $\Delta E_{S,\varphi}$ and $\Delta FWHM/2$ with respect to the angle φ . The cosine fit is based on Eq. (4.36) with an amplitude of $\Delta E_{S,[110]} = 0.18 \text{ meV}$. (c)-(e) Reconstruction of the experimentally measured spectra (solid lines) at $\theta = 45^\circ$. The dashed lines represent simulated curves, based on the spectra obtained for $\varphi = 90^\circ$. The method was introduced in the previous section.

intensity at around zero energy can be attributed to the elastically scattered light and the dashed line should represent the cutoff frequency of the triple Raman spectrometer. The characteristic Lindhard-Mermin line shape for the uppermost spectrum as well as a double peak structure for zero angle φ are easily identifiable. As deduced in the previous section (see Fig. 4.7), the energy of the peak separation of the intrasubband SDE, which is indicated here by colored arrows, is twice the spin splitting. The extracted values for the angular dependent spin splitting $\Delta E_{S,\varphi}$ are plotted in Fig. 4.11 (b) against the in-plane angle φ , and the fitting curve is a cosine function after Eq. (4.36) with an amplitude of 0.18 meV for the spin splitting in the $[110]$ direction, as determined in the previous discussion of sample A. An additional validation of the cosine behavior in the spin splitting may be achieved by the analysis of the line shape for each spectrum. Assuming the above introduced picture of two individual excitations, which share the same spectral shape but are energetically displaced by a certain amount, one can estimate the peak separation by

$$\Delta FWHM = FWHM(\varphi \neq 90^\circ) - FWHM(\varphi = 90^\circ) , \quad (4.37)$$

which describes the difference of FWHM between the considered direction and the direction, where only a single peak is present (here: $\varphi = 90^\circ$). As the plotted values in Fig. 4.11 (b) suggest, this method provides further evidence for the predicted behavior of the spin splitting, while the additional factor of 0.5 in the plot stems from the conversion of the peak separation. Moreover, the reproduction of the expected cosine-dependent spin splitting reinforces the claim of a zero or very close to zero spin splitting with a single peak structure, which is hardly verifiable under experimental conditions.

To ensure a reasonable accuracy for the extracted spin splitting $\Delta E_{S,\varphi}$, we applied for every measurement the already introduced method of peak simulation. Figure 4.11 (c) - (e) exemplarily depict the experimentally obtained spectra (solid lines) as well as the reconstructed curves (dashed lines) for a tilt angle of $\theta = 45^\circ$. Such an additional verification is quite appropriate for a transferred wave vector direction corresponding to small φ , but absolutely indispensable for higher values like $\varphi = 60^\circ$, where the spectrum shows no hint of a double peak structure. Small deviations between the shape of the measured and the simulated curves are not contradictory, because this method is based on the simplified model of two identical excitations, which add up equally. In fact, a different line shape is expected for different cutoff energies, since single-particle transitions with a smaller cutoff energy should also exhibit a steeper increase on the low energy side of the Lindhard-Mermin line shape. However, the comparison of simulated and measured curves suggests a rather small influence of this effect.

At this point we can draw as a preliminary conclusion that we have directly determined the spin splitting in sample A via inelastic light scattering on the intrasubband spin-density excitations. The predicted anisotropy for this (001)-grown quantum well system with approximately equal strengths of Rashba and Dresselhaus SO fields could be verified through a vanishing spin splitting for the $[1\bar{1}0]$ direction and a spin splitting of 0.18 meV for in-plane spins in the $[110]$ direction. We additionally demonstrated the cosine behavior of the spin splitting for in-plane directions deviating from the addressed crystal directions. All extracted values from these Raman measurements are in reasonable accordance with the values presented in Ref. [Wal12a], where the PSH for out-of plane excitations was proven by the magneto-optical Kerr effect in a sample from the same wafer.

4.2.4 Impact of the sample design on the direction of the PSH

Next we focus on sample B, which was also designed to fulfill the condition of the persistent spin helix. The 12 nm-wide single quantum well features similar to sample A an asymmetrical band profile, but the internal electric field is inverted due to a single doping layer on the vacuum side of the 2DES. However, the the-

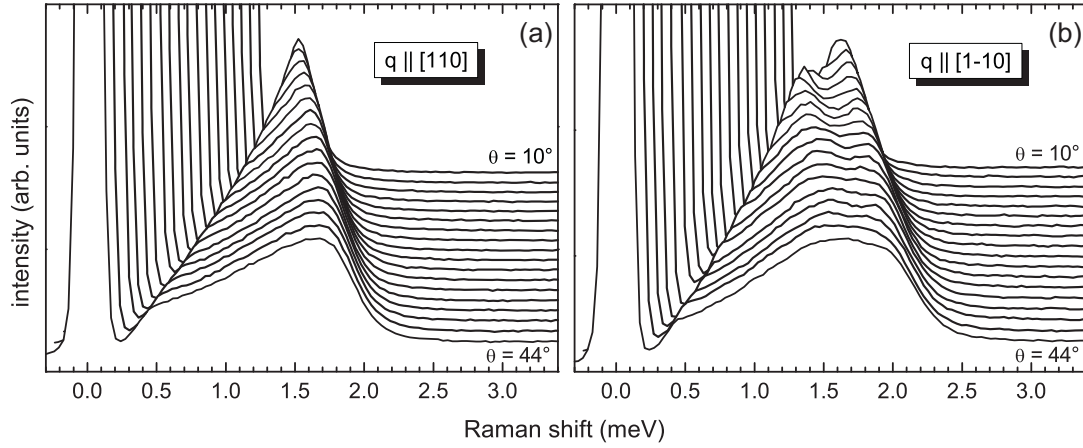


Figure 4.12: Waterfall plot of inelastic light scattering spectra from sample B for a fixed laser energy, measured at $T = 5.5\text{ K}$. A wave-vector transfer parallel to the $[110]$ (a) or the $[1\bar{1}0]$ in-plane direction (b) reveals the intrasubband SDE in depolarized scattering geometry. The transferred wave vector increases from $2.76 \times 10^6\text{ m}^{-1}$ for the top spectra ($\theta = 10^\circ$) up to $11.05 \times 10^6\text{ m}^{-1}$ for the bottom ones ($\theta = 44^\circ$). A vertical and horizontal alignment of single spectra provide a clearer overview.

oretical considerations about the scattering amplitude in Chap. 4.2.1 still hold, since both samples are based on a (001)-grown quantum well structure.

Figure 4.12 depicts the intrasubband SDE in depolarized scattering geometry for a wave-vector transfer parallel to $[110]$ (a) and $[1\bar{1}0]$ (b). Each waterfall plot contains a series of spectra ranging from a tilt angle of $\theta = 10^\circ$ for the top to $\theta = 44^\circ$ for the bottom spectrum. The elastically scattered light is visible at around zero energy and the kink in each spectra, located at about 0.4 meV for the bottom ones, can be attributed to the band pass feature of the triple stage Raman spectrometer. Contrary to sample A, a double peak structure is now observable for a transferred wave vector along $[1\bar{1}0]$, while a single peak appears for the orthogonal in-plane direction. This behavior can be easily explained by means of the prevalent spin-orbit field in the 2DES. The Dresselhaus field, induced by bulk inversion asymmetry, is mainly determined by the growth direction of the nanostructure and by the width of the corresponding quantum well system. Since both criteria are equally fulfilled in sample A and sample B, we can expect a very similar contribution from the Dresselhaus field. The contribution from the Rashba field, however, differs due to an inverted orientation of the internal electric field. Provided that both spin-orbit fields are of equal strengths with $\alpha = -\beta$, a $\text{SU}(2)$ symmetry with a uniaxial effective field along the $[110]$ direction emerges (see Fig. 4.5 (c)) and we arrive at the situation sketched in Fig. 4.7, but with interchanged crystal directions. Consequently, the spin-flip transitions exhibit a spin splitting of in-plane spins in the $[1\bar{1}0]$ direction and only a single peak for a wave-vector transfer along $[110]$. While all spectra in Fig. 4.12 (a) reflect the expected Lindhard-Mermin lineshape perfectly, a double peak structure in subframe (b) is well identifiable for smaller wave vectors only. Such a blurring for

higher tilt angles may be attributed either to the broadened line shape of each single excitation of the assembled double peak structure, or to a certain admixture with non spin-flip transitions, which gains more influence for larger wave vectors due to nonzero z -components of the light polarizations.

Similar to sample A, the peak position is extracted from the measured spectra and plotted in Fig. 4.13 against the transferred wave vector. Experimental data from even higher tilt angles as depicted in the waterfall plots are also included in this analysis. The solid lines suggest a nearly constant peak separation over the whole investigated range, and verify the expected behavior with the single peak in the center between the double peak structure. From this experimental behavior we can conclude with some caution that the spin helix symmetry for sample B is mainly fulfilled within the boundaries of accessible accuracy in such a Raman investigation. The maximum spin splitting is determined through the halved peak separation and yields $\Delta E_{S,[1\bar{1}0]} = (0.19 \pm 0.05) \text{ meV}$, which

is quite close to the spin splitting of sample A obtained in the $[110]$ direction. Additional studies with a perpendicular magnetic field revealed an effective electron mass of $m^* = (0.073 \pm 0.001) m_e$, and thus an electron density of $N_s = (4.68 \pm 0.70) \times 10^{15} \text{ m}^{-2}$ could be estimated after Ref. [Fas87] from the spectra in Fig. 4.12(a). The corresponding Fermi wave vector of $k_F = (1.71 \pm 0.18) \times 10^8 \text{ m}^{-1}$ leads to an estimation of $|\alpha| \approx |\beta| = (2.78 \pm 0.83) \text{ meV \AA}$ if a balanced ratio of Rashba and Dresselhaus field is assumed. According to Eq. (4.20), the characteristic magnitude for the paraboloid displacement is then given by $\Delta k = (1.06 \pm 0.33) \times 10^6 \text{ m}^{-1}$ and for the wavelength of the PSH follows $\lambda_{PSH} = (5.9 \pm 1.5) \mu\text{m}$. These values deviate only slightly from the ones obtained for sample A, which is very well expected due to a similar sample design and a nearly identical magnitude of spin splitting. Complementary measurements, carried out in our workgroup, further confirmed the presented results as a PSH wavelength of $\lambda_{PSH} = (5.5 \pm 0.5) \mu\text{m}$ was detected for sample B at $T = 40 \text{ K}$ by using the same mapping technique as described in Ref. [Wal12a].

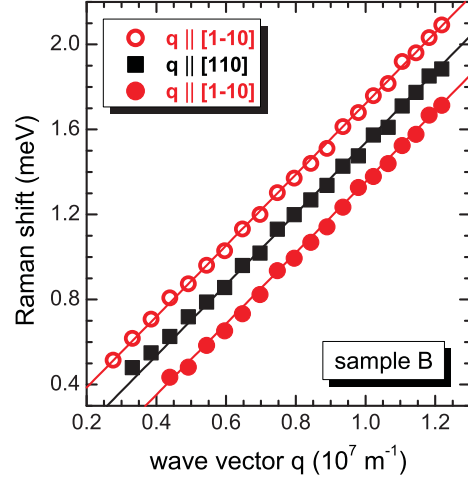


Figure 4.13: *Extracted peak positions of the intrasubband SDE with respect to the transferred wave vector.*

4.2.5 Excitations in polarized scattering geometry

So far we only regarded intrasubband transitions in depolarized scattering geometry, now we take a quick detour and discuss non spin-flip excitations within a single subband occurring in polarized scattering geometry.

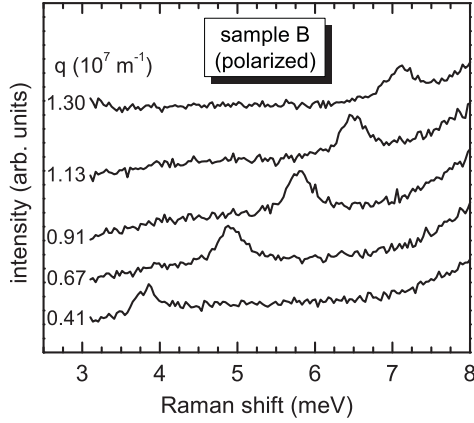


Figure 4.14: Polarized Raman spectra for sample B at a fixed laser energy. The vertically shifted spectra reveal the intrasubband CDE for a wave-vector transfer of $q = 0.41 - 1.30 \times 10^7 \text{ m}^{-1}$.

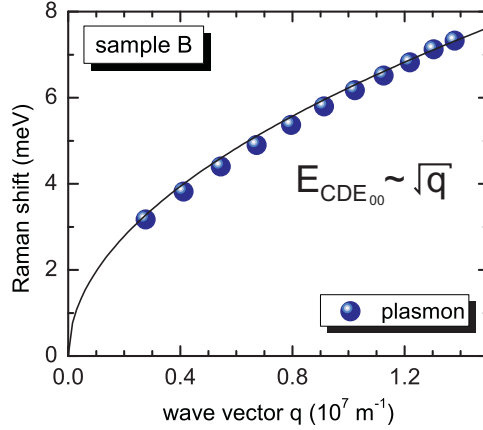


Figure 4.15: Extracted peak positions of the plasmon plotted against the transferred wave vector. The energy of the intrasubband CDE follows the expected square root behavior of q .

Figure 4.14 illustrates the intrasubband CDE (intrasubband plasmon) of sample B emerging in a parallel scattering configuration. The selected spectra are vertically shifted and cover a transferred wave vector range between 0.41 and $1.30 \times 10^7 \text{ m}^{-1}$. In contrast to intrasubband SDEs, the particular direction of in-plane wave vectors does not play a role here, because only non spin-flip transitions contribute to the charge-density wave and hence, all in-plane directions should reveal the same excitation energies if a parabolic band structure is assumed. This expectation was probed and could be verified for the most part. The depicted spectra reveal a rather weak and broad plasmon line shape, which may be attributed to a strong doping concentration of the heterostructure. Since free carriers occasionally occur in the AlGaAs barriers of highly modulation doped quantum wells systems, a parallel conductance between these carriers and the plasmon mode might appear. Considering the macroscopic picture, where the intrasubband CDE is described by a charge-density oscillation parallel to the quantum well plane, a Coulomb induced coupling to free carriers in the barrier would lead to a damped oscillation, because carriers in the barrier typically exhibit a very low mobility due to the strong disorder potential and the Coulomb scattering with positively-charged donors in this region [Sch06].

The extracted peak positions of the plasmon are plotted in Fig. 4.15 against the transferred wave vector. As expected, the energy of the intrasubband CDE follows after Eq. (3.14) a square root dependency on q . If we use the high frequency dielectric constant $\epsilon_\infty = 10.9$ for GaAs and an effective mass of $m^* = (0.073 \pm 0.001) m_e$, we can deduce the carrier density for sample B from this measurement as $N_s = (4.48 \pm 0.60) \times 10^{15} \text{ m}^{-2}$. This is in reasonable accordance with the value obtained in the analysis of the previous section based on the intrasubband spin-density wave. Hence, both independent measurements confirm the assumption that the actual carrier density in the Raman experiments is somewhat

lower than the nominal value determined after the growth process via transport experiments.

Surprisingly, the polarized scattering geometry reveals a second excitation besides the discussed intrasubband CDE. A single spectrum for $q = 5.4 \times 10^6 \text{ m}^{-1}$ is illustrated in Fig. 4.16 and compared with the corresponding spectrum obtained in the depolarized scattering geometry. Here, a wave-vector transfer parallel to [110] is selected to provide a single-peak structure for the spin-flip excitation in depolarized configuration. As indicated, the peak energy in the polarized spectrum is slightly shifted to higher energies and a different line shape is recognizable. The origin of this excitation is not fully understood yet, but due to their energy they can be regarded as single-particle transitions within a single subband. Consequently, the small discrepancy between both peak energies may be attributed to the strongly Landau-damped excitation in the depolarized scattering geometry, because the intrasubband SDE is fully subjected to the single-particle continuum and therefore indistinguishable with a single-particle transition.

However, if we reconsider the small discrepancy of SPE energy concerning the scattering configuration in the previous presented intersubband transitions (see Fig. 3.13), where for $q = 0$ no Landau damping should be present, we might have to discuss an additional approach for this issue. Using the phenomenological picture again, we can regard (intersubband and intrasubband) CDEs in polarized scattering geometry as a coherent charge oscillation against the positively charged background. If the phase correlation between the oscillating carriers would be lost, the collective charge mode would decay into incoherent oscillations and the depolarization shift is averaged out to some extent. Such a picture might explain the energy difference between collective and single-particle-like excitations in the spectra. Furthermore, if we regard the here depicted intrasubband SDE as an incoherent oscillation as well, an energy discrepancy between both single-particle transitions in Fig. 4.16 is quite reasonable, since no defined phase correlation is present in both configurations. This macroscopic picture is reinforced by theoretical calculations about the scattering amplitude in GaAs quantum dots, where single-particle-like states with a slightly deviating energy for different scattering configurations are predicted [Ste99, Ste00].

With that, we conclude the short subchapter about excitations in polarized scattering geometry and return to the main aspect of this chapter, the intrasubband SDE, observable with crossed polarizations.

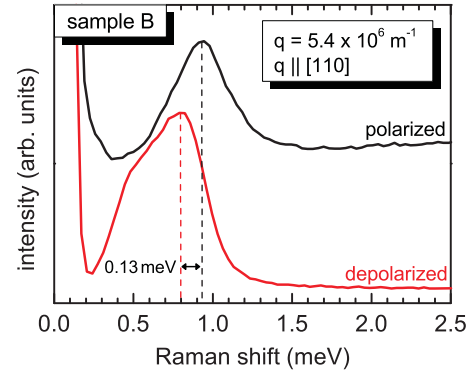


Figure 4.16: Comparison of intrasubband transitions between polarized and depolarized scattering geometry. The cutoff energy of the spectrometer is about 0.5 meV.

4.2.6 Influence of an external electric field

A major task in nowadays physics is not only to grow heterostructures with a certain spin-orbit interaction, but also to control and tune the incorporated field externally during the measurement. Several studies figured mechanical strain as a possible approach [Kat03, Cro05, Sih06], however, a more common way to influence the spin-orbit field is the application of an external electric field [Nit97, Mil03, Stu09]. Very recent publications demonstrated furthermore that the condition of the persistent spin helix state can be realized by external gate tuning [Koh12, Ish14] and hence, revealed a more precise way to experimentally access the desired ratio of equal Rashba and Dresselhaus fields.

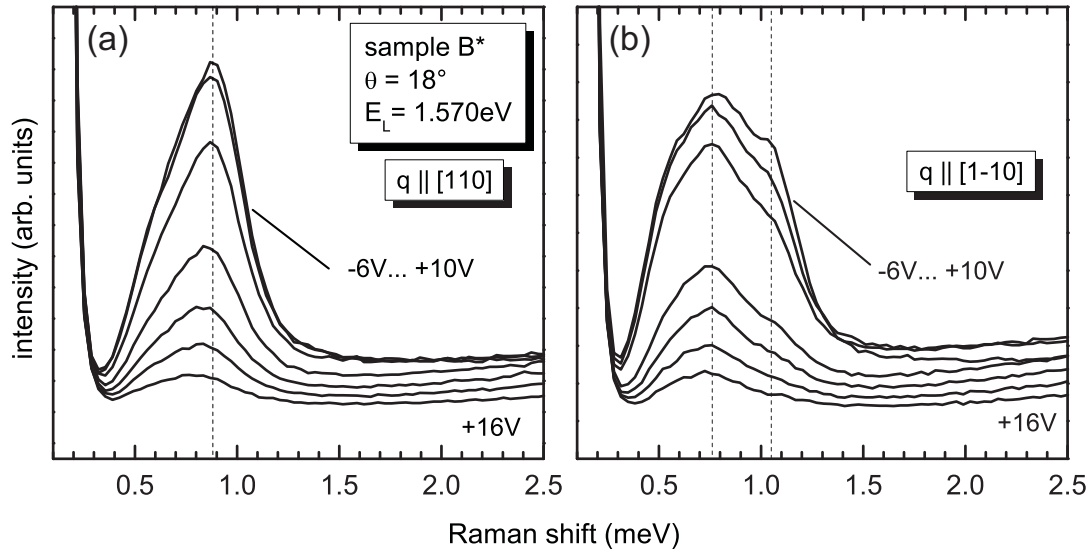


Figure 4.17: Depolarized Raman spectra for a fixed tilt angle of $\theta = 18^\circ$ and a wave-vector transfer parallel to $[110]$ (a) and $[1\bar{1}0]$ (b). The gate voltage is varied between -6 V and $+16\text{ V}$ (bottom spectrum), while the uppermost curve is obtained at 0 V and represent for a clearer picture the whole range between -6 V and $+10\text{ V}$, since these curves are nearly identical.

For optical measurement techniques like inelastic light scattering, a semi transparent top gate is evaporated to detect a Raman signal, which is simultaneously influenced by the applied gate voltage. This external electric field allows a direct manipulation of the Rashba SO field, since it interferes with the internal electric field E_z , which defines the strength of spin splitting due to structure inversion asymmetry (see Eq. (4.16)). Consequently, the total spin splitting should be tunable by means of an external gate.

Figure 4.17 demonstrates the electrical field dependence of the intrasubband SDE in sample B* for a fixed tilt angle of $\theta = 18^\circ$. Spectra for both in-plane directions are detected for a gate voltage range between -6 V and $+16\text{ V}$. Similar to the signals for intersubband transitions, a spectral variation emerges not until a quite high voltage is applied and so the nearly unchanged spectra for a gate voltage from -6 V up to $+10\text{ V}$ is represented in these two subframes by the cor-

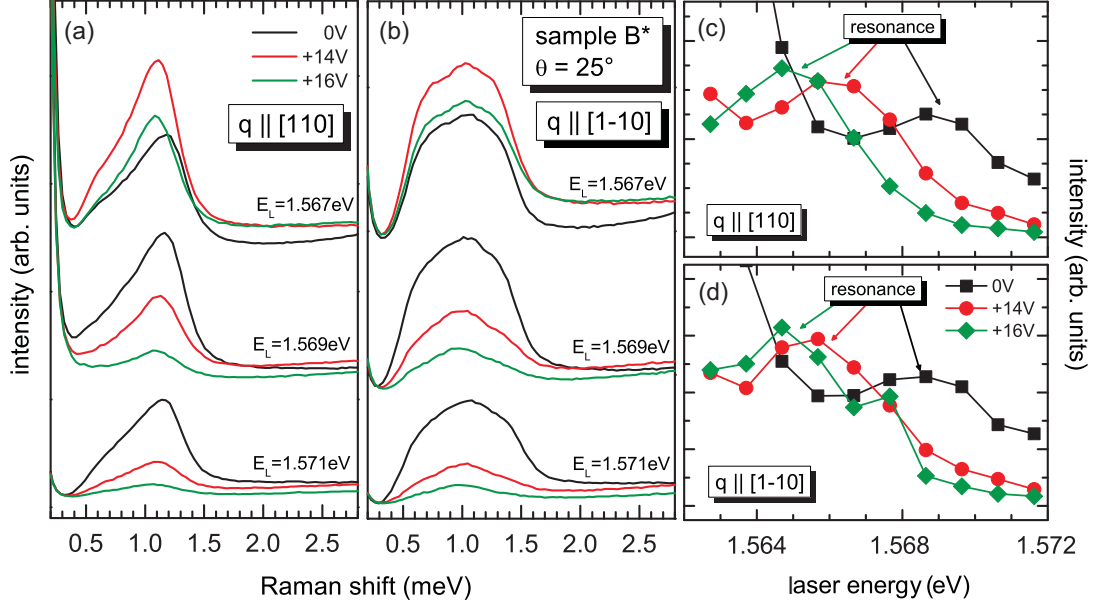


Figure 4.18: Selected spectra in depolarized scattering geometry for a fixed tilt angle of $\theta = 25^\circ$ and a wave-vector transfer parallel to $[110]$ (a) and $[1\bar{1}0]$ (b). Each plot contains a comparison of measured spectra at 0 V, +14 V and +16 V for three different excitation energies. (c) Extracted peak intensities plotted against the laser energy. (d) Same as (c), while only the maximum in the double-peak structure is extracted.

responding spectrum obtained at 0 V. Focusing on these two uppermost spectra, the single peak for a wave-vector transfer parallel to $[110]$ is clearly identifiable and we can observe a double peak structure for the $[1\bar{1}0]$ direction. The peak separation in Fig. 4.17 (b) reveals a spin splitting of $\Delta E_{S,[1\bar{1}0]} = (0.14 \pm 0.05) \text{ meV}$, which is somewhat lower as the extracted value for sample B. Such a discrepancy probably stems from an inconsistency of sample parameters throughout the wafer and was already reported for these two samples in the previous chapter about the intrasubband transitions with an applied gate voltage. Nevertheless, this should not affect the investigation about the influence of an external gate, since a huge anisotropy in spin splitting is still visible. Regarding the transition parallel to $[110]$ (Fig. 4.17 (a)), a decrease in peak intensity is clearly observable for increasing gate voltage and a slight shift to lower energies appears. This behavior is mainly reproduced in the orthogonal direction (Fig. 4.17 (b)), but a double peak structure is only hardly recognizable for very high gate voltages. From photoluminescence measurements and investigations on the intrasubband plasmon we can estimate a total decrease in carrier density by $\sim 15 - 20 \%$ for high values of the applied voltage range, which would explain the redshift of the excitation. However, a significant variation of spin splitting can not be observed within a range of -6 V to $+13 \text{ V}$, but it remains an open question for very high gate voltages, because the decreased intensity allows no reliable interpretation.

To clarify that issue, we varied the laser energy between 1.562 and 1.572 eV and measured the intrasubband SDE for 0 V, +14 V and +16 V. Selected spectra

for a fixed tilt angle of $\theta = 25^\circ$ are presented in Fig. 4.18 (a) and (b). The peak intensities for $E_L = 1.571$ eV in subframe (a) are as expected from the previous discussion, with a strong SDE for 0 V and a fading intensity for an increased gate voltage. If the excitation energy is decreased, we can observe nearly unchanged curves for 0 V and strongly enhanced intensities for non zero external fields, but the line shape approximately remains. As already addressed, different peak energies may be attributed mainly to changed carrier densities in the 2DES. A similar behavior is revealed for a wave-vector transfer parallel to $[1\bar{1}0]$, where the double peak structure is only hardly visible due to a small peak separation (Fig. 4.18 (b)). However, considering the spectra for $E_L = 1.567$ eV, where all excitations share a sufficient intensity, no essential difference in the line shape is identifiable throughout the regarded voltage range. Note that the kink on the low energy side of the SDE in (b) at around 0.6 meV stems from the cutoff of the triple stage Raman spectrometer, and not from an electronic excitation. For a further analysis, we extracted the peak intensities from the measured spectra and plotted them in Fig. 4.18 (c) and (d) against the laser energy. Since an exact determination of the double peak is very difficult here, we only used the maximum intensity in the spectra from the $[1\bar{1}0]$ direction, but the qualitative behavior matches very well the one obtained in the orthogonal in-plane direction. The resulting curves emphasize the importance of resonance effects, with an indicated resonance probably due to the LH valence band. This resonance shifts to lower excitation energies for very high gate voltages, suggesting either a lowered carrier density, because single-particle transitions mainly occur at the Fermi edge [Jus00], or a decreased band gap. The intensity enhancement at even lower laser energies, especially visible for 0 V, can be attributed to the resonance with the HH valence band. Unfortunately, the Raman signal for this resonance is superimposed by the photoluminescence from the fundamental band gap and is consequently not accessible.

From these results we can infer that we are not able to detect a significant change in spin splitting over the applied gate voltage range. Deviations in peak intensities are mainly due to resonance effects with the valence band, since an applied electric field results in a changed carrier concentration, which affects the resonance condition of single-particle transitions. Although various publications on different experimental techniques demonstrated a dependency of the spin-orbit interaction on an external electric field, a good tunability of the spin splitting is beyond the experimental limits of Raman scattering, since no hint of variation is visible and the strength of the electric field is restricted by the simultaneously decreasing Raman signal for thicker top gates.

Before we conclude this section about the (001)-grown quantum wells, we should mention sample C for the sake of completeness. In the course of the above discussed investigations, we also studied the intrasubband SDE of this heterostructure, but no spin splitting could be detected in any in-plane direction. However, a very low spin splitting, which lies below the resolvable limit for this measurement technique, is quite reasonable for these sample parameters. The maximum spin

splitting for in-plane spin states is given by $\Delta E_S = 2(\alpha + \beta)k_F$ (see Eq. (4.30)), while the Dresselhaus parameter scales with $\beta \sim (\pi/d_{QW})^2$. Consequently, an increase of well width from 12 nm to 25 nm would lead to an attenuation of β by more than a factor of 4. Moreover, a lower carrier density also implies a lower spin splitting through $k_F = \sqrt{2\pi N_s}$. A qualitative prediction about the Rashba parameter is very difficult here, but given the fact of a similar sample structure as sample B, combined with a decreased carrier density, we might assume a weaker internal electric field and hence, a decreased Rashba parameter α . In a very rough estimation with the Rashba field strength of sample B, which is certainly not correct for sample C, we can give $\Delta E_S = 0.08$ meV as an upper limit for the spin splitting. This value is already very close to our resolvable limit, and confirms our experimental findings if we take the actual Rashba field into consideration, which is most likely lower than the one assumed for the estimation. A further discussion of intrasubband transitions in sample C is spared here, since no additional knowledge arises from the experimental findings.

4.3 Intraband excitations in (110)-grown quantum wells

Another popular representative of spintronic research is the quantum well system with a quantization axis along the [110] direction. The striking feature is the unidirectional Dresselhaus field, which points out of the quantum well plane and leads to a strong suppression of the Dyakonov-Perel spin dephasing mechanism [Dya71a] for spins with an out of plane orientation [Dya86, Ohn99]. As a consequence, a strong spin dephasing anisotropy can be observed for these structures [Dö4], revealing very long lifetimes up to 100 ns for spins along the growth direction [Gri12b], while the lifetime for in-plane spins is decreased by more than one order of magnitude, even in the absence of a Rashba SO field. A very recent publication demonstrated the persistent spin helix state in a (110)-oriented quantum well structure by means of time- and spatially-resolved Kerr rotation, yielding a Dresselhaus coefficient of $\gamma \sim -10$ eVÅ³ for the unidirectional spin-orbit field [Che14], which compares fairly well with the one obtained in similar (001)-grown structures [Wal12b]. In the following, we will elaborate on the theoretical peculiarities of (110)-grown quantum wells for electronic Raman scattering on intrasubband transitions and discuss the consequences for our experimental investigations.

4.3.1 Theoretical considerations

In (110)-grown quantum wells with zinc-blende structure arises a very interesting situation if the Rashba field is negligibly small, because the remaining Dresselhaus contribution forces all electron spins to align to this uniaxial SO field, which is perpendicular to the quantum well plane. In such a situation, a SU(2) symmetry is established and the condition for a persistent spin helix state is fulfilled [Ber06].

A technical realization of a vanishing Rashba contribution is provided through a symmetrical band profile with accurately balanced modulation dopings.

At the beginning we focus on the scattering amplitude and deduce what kind of excitation we can expect for a (110)-grown quantum well. Here, we can use the scattering amplitude for single-particle transitions in depolarized scattering geometry as a starting point (see Eq. (4.25)), since it describes the intrasubband SDE independent from the quantization axis of the heterostructure. Similar to (001)-grown quantum wells, a nonzero contribution from the cross product of the polarization vectors is expected only for the z -component, if an exact backscattering geometry is assumed. In the case of a vanishing Rashba field, all electron spins are aligned parallel or antiparallel to the growth direction and the spin-dependent part of the electron wave function can be written as:

$$\psi_{\uparrow} = |\uparrow\rangle = \begin{pmatrix} 1 \\ 0 \end{pmatrix} \quad \text{and} \quad \psi_{\downarrow} = |\downarrow\rangle = \begin{pmatrix} 1 \\ 0 \end{pmatrix} \quad (4.38)$$

Inserting these wave functions into Eq. (4.25), we can deduce the scattering amplitude for non spin-flip and spin-flip transitions, respectively, starting from a spin-up state:

$$A_{\uparrow\uparrow} = \Pi_d \cdot \begin{pmatrix} 1 \\ 0 \end{pmatrix}^* \begin{pmatrix} 1 & 0 \\ 0 & -1 \end{pmatrix} \begin{pmatrix} 1 \\ 0 \end{pmatrix} = \Pi_d \cdot \begin{pmatrix} 1 \\ 0 \end{pmatrix} \begin{pmatrix} 1 \\ 0 \end{pmatrix} = \Pi_d \quad (4.39)$$

$$A_{\uparrow\downarrow} = \Pi_d \cdot \begin{pmatrix} 1 \\ 0 \end{pmatrix}^* \begin{pmatrix} 1 & 0 \\ 0 & -1 \end{pmatrix} \begin{pmatrix} 0 \\ 1 \end{pmatrix} = \Pi_d \cdot \begin{pmatrix} 1 \\ 0 \end{pmatrix} \begin{pmatrix} 0 \\ -1 \end{pmatrix} = 0 \quad (4.40)$$

The calculation for excitations from a spin-down state are straightforward and yield the same result, which says that only non spin-flip transitions are allowed in this configuration. Note that this is only an approximation, since a nonzero tilt angle of the sample ($\theta \neq 0$) would result in additional components for the x and y direction. As discussed in the section about (001)-grown quantum wells, however, this admixture is expected to be rather small for GaAs-based materials.

Figure 4.19 depicts a cut through the energy paraboloids for a (110)-grown system with Dresselhaus SO interaction only. The effective field, pointing out of the quantum well plane, leads for the $[1\bar{1}0]$ in-plane direction to a spin splitting of $\Delta E_{s,[1\bar{1}0]}$ along the energy axis (a). If we consider only non spin-flip excitations with a fixed transferred wave vector in the schematic enlargement on the right-hand side (c), we can identify the same energy for both transitions. Keep in mind that all depicted spin states here are out-of plane spins, as a contrast to the previous discussed system of (001)-grown quantum wells, where only in-plane spins were regarded due to the in-plane SO field. The spin states for the perpendicular in-plane direction (c) are still degenerated and only a single transition energy can be observed for a fixed q (d). If we take into consideration that all other in-plane directions indeed feature a different spin splitting ΔE_s , but still share the same transition energy for a fixed wave vector, we have to conclude that this method is

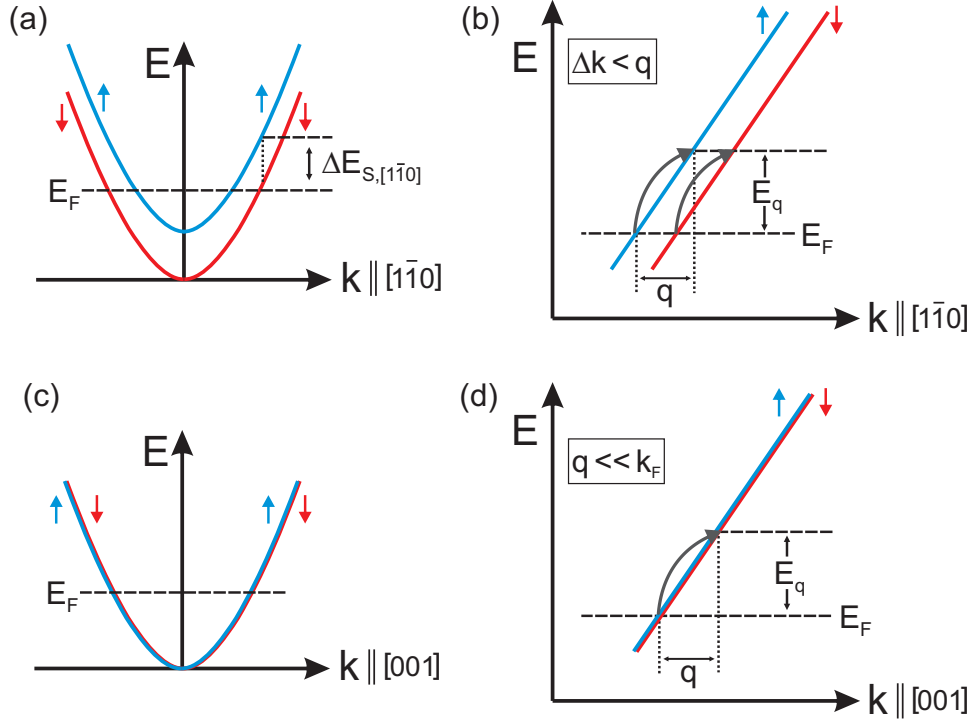


Figure 4.19: (a) Cut through the energy paraboloids in the $[1\bar{1}0]$ in-plane direction. (b) Schematic enlargement of the area around the Fermi energy. Non spin-flip intrasubband transitions for a fixed transferred wave vector q and $\Delta k < q$ are indicated by curved arrows. (c) and (d): Same consideration, but for a cut in the $[001]$ direction, where the spin splitting is zero.

unable to distinguish between different in-plane directions and therefore fails to detect the spin splitting.

A possible way to bypass this unfavorable situation might be found in a change of polarization directions of the incident and scattered light, as the following example elucidates: Assuming an unchanged polarization vector in the y direction for the scattered light, but a modification of incident polarization from the x to the z direction, we achieve for the cross product

$$(\mathbf{e}_I \times \mathbf{e}_S) = (0, 0, 1) \times (0, 1, 0) = (-1, 0, 0) .$$

Consequently, only x components contribute to the scattering amplitude and we arrive with σ_x at

$$A_{\uparrow\uparrow} = -\Pi_d \cdot \begin{pmatrix} 1 \\ 0 \end{pmatrix}^* \begin{pmatrix} 0 & 1 \\ 1 & 0 \end{pmatrix} \begin{pmatrix} 1 \\ 0 \end{pmatrix} = -\Pi_d \cdot \begin{pmatrix} 1 \\ 0 \end{pmatrix} \begin{pmatrix} 0 \\ 1 \end{pmatrix} = 0 \quad (4.41)$$

$$A_{\uparrow\downarrow} = -\Pi_d \cdot \begin{pmatrix} 1 \\ 0 \end{pmatrix}^* \begin{pmatrix} 0 & 1 \\ 1 & 0 \end{pmatrix} \begin{pmatrix} 0 \\ 1 \end{pmatrix} = -\Pi_d \cdot \begin{pmatrix} 1 \\ 0 \end{pmatrix} \begin{pmatrix} 1 \\ 0 \end{pmatrix} = -\Pi_d , \quad (4.42)$$

describing the possible transitions from a spin-up state, with a vanishing contribution for a non spin-flip process and a finite possibility for spin-flip transitions. The complementary calculation for an initial spin-down state yields the same result, as well as the variation of the scattered light polarization from y to x direction. Generally speaking, we expect the desired spin-flip transitions if either the incident or the scattered light is polarized along the z direction. This would provide a possible approach to measure the spin splitting in (110)-grown quantum wells, however, the experimental realization of this configuration is very tough. Since the polarization vector of light is always perpendicular to its propagation direction, a focusing of the laser light normal to the growth direction would be required, if the scattered light is gathered as usual in a direction along the quantization axis. Such a laser alignment on the edge of the sample would bear a huge challenge on its own, but intrasubband transitions are only possible with a finite tilt angle, which would rise even more complications. Although a technical realization of this scattering configuration was not possible with the given Raman setup, we can leave these considerations as a motivation for future experiments. In the following, we present our results on the intrasubband SDE in backscattering geometry, as depicted at the beginning of this section.

4.3.2 The persistent spin helix state in (110)-grown quantum wells

Modern growth schemes with a symmetrical distribution of doping layers allow the fabrication of structures with a vanishing Rashba field. If the quantum well

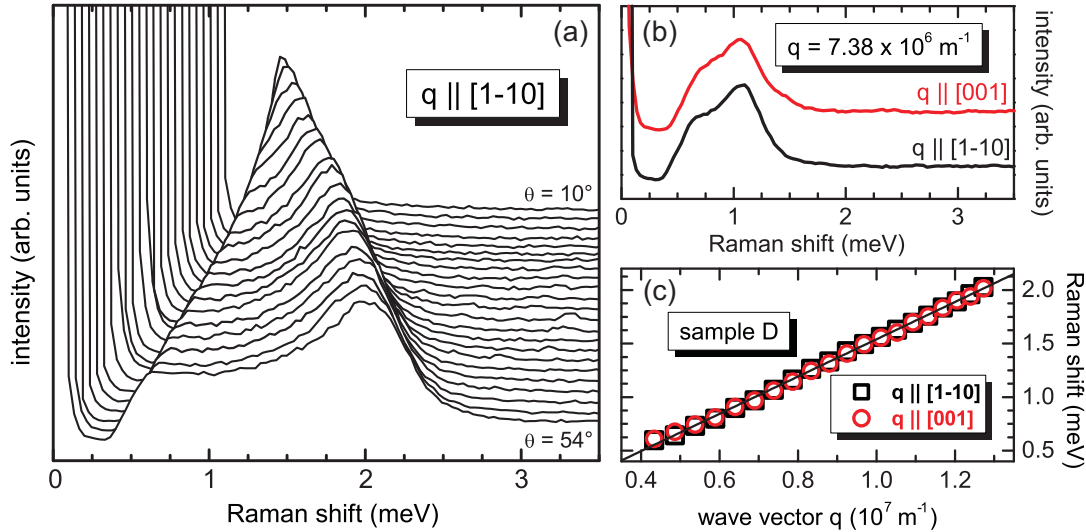


Figure 4.20: (a) Waterfall plot for sample D in depolarized scattering geometry with a wave-vector transfer parallel to $[1\bar{1}0]$ and a tilt angle varying between $\theta = 10^\circ$ and 54° . A vertical and horizontal shift of single spectra provide a clearer overview. (b) Comparison between two in-plane directions for a fixed $q = 7.38 \times 10^6 \text{ m}^{-1}$. (c) Extracted peak positions plotted against the transferred wave vector.

is based on a (110)-oriented substrate, free electrons are only subjected to an out-of-plane SO field, as induced from the Dresselhaus contribution. Sample D is grown after this pattern and aims to fulfill the conditions of a uniaxial SO field.

The results of scattering on the intrasubband SDE are illustrated in Fig. 4.20. In this configuration, only non spin-flip single-particle-like excitations are allowed for an approximation of exact backscattering. Subframe (a) shows a waterfall plot with a transferred wave vector parallel to $[1\bar{1}0]$, ranging between $\theta = 10^\circ$ and $\theta = 54^\circ$. The single peak, which shifts to higher energies for higher transferred wave vectors, is clearly observable. A comparison between two orthogonal in-plane directions is depicted in (b) for a fixed wave vector of $q = 7.38 \times 10^6 \text{ m}^{-1}$, revealing similar spectra with a nearly identical peak energy. The peak positions for all measured spectra are extracted and plotted in subframe (c) against the transferred wave vector. These experimental results verify the theoretical prediction that only a single peak energy is present for all in-plane directions. However, it also confirms that a determination of spin splitting is not possible with the used backscattering geometry.

Chapter 5

Anti-Stokes measurements

The anti-Stokes component of Raman scattering is often left out of consideration for GaAs based materials, since only a few excitations are existent at very low temperatures. An investigation under these conditions is mostly unrewarding or requires a pump-probe technique to previously create some excitations in the system. Early publications in this research field focused on the anti-Stokes component of LO phonons [Moo66, vdL80], however, observations on electronic excitations in GaAs are quite rare in literature. More recent studies involving anti-Stokes measurements reported on plasmon dispersions in a 2DES and could derive the electron temperature from the ratio between the plasmon intensities of Stokes and anti-Stokes components [Bha95, Bha96]. Nevertheless, a single-particle excitation could not be observed on the anti-Stokes side [Bha96] and neither were reported in common literature. In this short chapter, we will present our results on anti-Stokes measurements of the intrasubband SDE and discuss a possible explanation for our observations.

5.1 Wave-vector dependency

Some selected spectra of the anti-Stokes component in sample B are plotted in Fig. 5.1 (a). The nominal temperature was fixed at $T = 5.5$ K and a wave vector parallel to $[110]$ is transferred during the scattering mechanism. Starting at a tilt angle of $\theta = 20^\circ$, a fairly sharp peak appears just above the cutoff frequency of the triple stage Raman spectrometer, which is represented by the dashed vertical line. For higher tilt angles, the relatively sharp contour evolves into a broad feature with a slowly decreasing high energy tail. To understand these observations, we need to consider the corresponding Stokes signal, which is depicted in Fig. 5.1 (c) for a wave-vector transfer parallel to $[110]$, where the spin splitting is zero. Generally speaking, the Stokes component for an intrasubband SDE describes excitations of electrons within a single subband and is characterized by the Lindhard-Mermin line shape. Furthermore, all electrons are subjected to the Fermi-Dirac distribution. For the anti-Stokes process, this distribution is of great

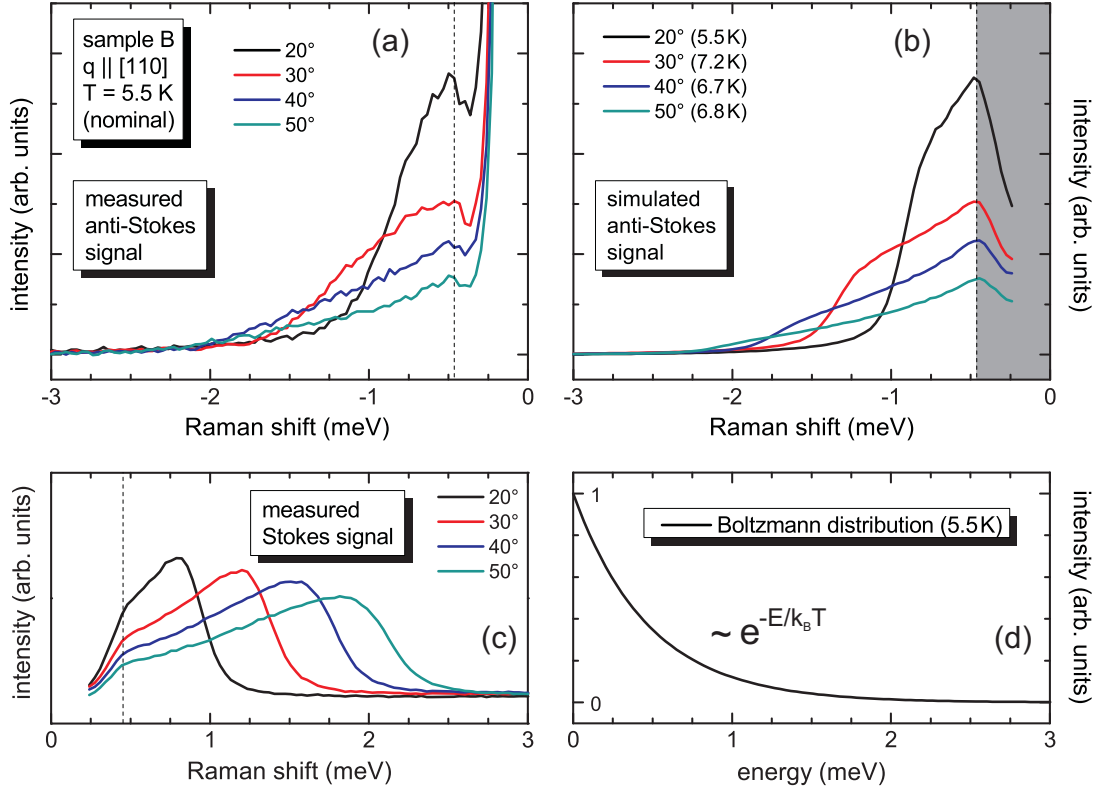


Figure 5.1: (a) Selected anti-Stokes spectra in depolarized scattering geometry for sample B, measured at a nominal temperature of $T = 5.5$ K. The wave vector is transferred parallel to [110] with a tilt angle between $\theta = 20^\circ$ and $\theta = 50^\circ$. The dashed line represents the cutoff energy of the Raman spectrometer. (b) Simulated anti-Stokes signal with an adjusted temperature for the best fitting result. The gray shaded area is below the cutoff energy and not considerable. All simulated curves are a product of the corresponding Stokes signal (c), also measured for $q \parallel [110]$, and the Boltzmann distribution (d) with the temperature as a fitting parameter.

importance because it describes thermally excited electrons (for $T > 0$), which can be annihilated during the scattering process. The distribution of electrons located above the Fermi edge due to nonzero temperature can be approximated by the Boltzmann distribution, which is exemplarily plotted for $T = 5.5$ K in Fig. 5.1 (d). According to this exponential function, most existing excitations in a system are locatable just above the Fermi energy, while the occupation decreases with increasing energy deviation from the Fermi edge (here: zero energy). Since the intensity of the anti-Stokes component (I_{AS}) is given by [Car82, Bha95]

$$I_{AS} = I_S \cdot \exp \left[\frac{-E}{k_B T} \right], \quad (5.1)$$

we can now combine the measured Stokes signal (I_S) of subframe (c) with the Boltzmann distribution for existing excitations to reconstruct the anti-Stokes signal for the measured intrasubband SDE. The simulated curves for the anti-Stokes process are depicted in Fig. 5.1 (b), while the temperature of the Boltzmann distribution was adjusted for each curve to provide the best match with the measured

signal in subframe (a). Please note that the gray shaded area is left out of consideration because the simulation depends on the measured Stokes signal and hence no reliable calculation is possible below the cutoff frequency of the Raman spectrometer. Above 0.5 meV, the simulated curves assimilate the measured anti-Stokes spectra very well. Since all fitting temperatures are in a reasonably small range above the nominal temperature of $T = 5.5$ K, we can exclude a drastic heating of the electron gas by the laser radiation. In order to investigate how an increased temperature affects the anti-Stokes component in general, a study on the temperature dependency is conducted and presented in the next section.

5.2 Temperature dependency

An essential requirement for the anti-Stokes process is an existing excitation in the investigated system. For experiments without optical pumping, the most obvious way to stimulate the electrons in the 2DES is to increase their temperature. Figure 5.2(a) shows depolarized spectra of the anti-Stokes component for sample B, obtained with temperatures ranging from 5.5 K up to 17.5 K. All spectra are measured with a wave-vector transfer parallel to $[110]$ and a fixed tilt angle of $\theta = 30^\circ$. The intensities are not modified and allow the first conclusion that excitations are strongly enhanced in the system if the temperature is raised. But not only the peak intensity increases, also the high energy tail is more pronounced with a slowly descending slope for high temperatures like 17.5 K, whereas a relatively sharp cutoff at around -1.5 meV is detected for $T = 5.5$ K. A simulation for the anti-Stokes spectra as realized in the previous section is not possible here, since no corresponding Stokes spectra for $T > 10$ K are accessible due to a superposition

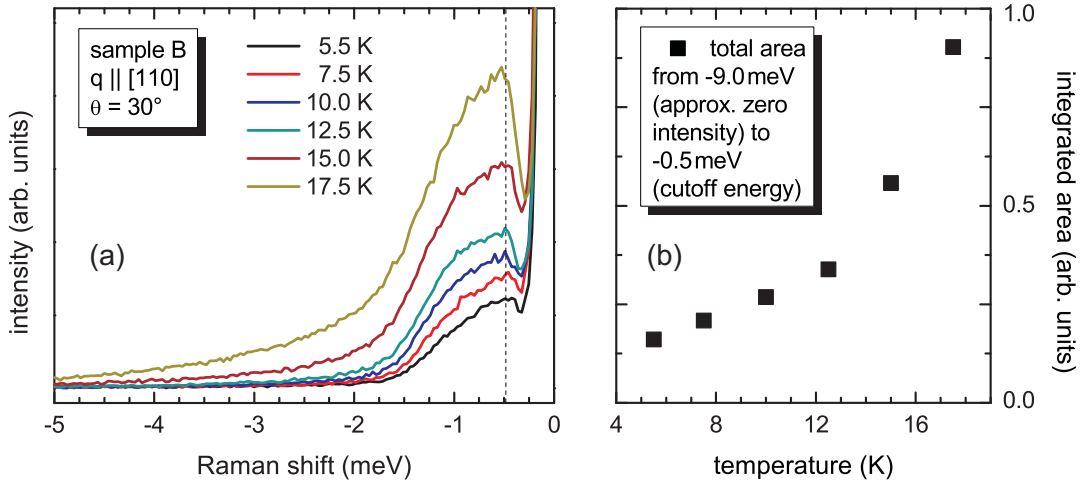


Figure 5.2: (a) Measured spectra of sample B in depolarized scattering geometry for different temperatures. A fixed tilt angle of $\theta = 30^\circ$ ensures a wave-vector transfer along $[110]$. Intensities are not shifted to provide a good comparability. (b) Total integrated area from -9 meV to -0.5 meV plotted against the nominal temperature.

of the Raman signal by the broadening PL trace and a calculation with a Stokes spectrum for $T = 5.5$ K would yield a significant error at higher temperatures.

To examine the total intensity increase for a raising temperature in more detail, an integration of the total area of the anti-Stokes signal is carried out and presented in Fig. 5.2 (b). The contributing area is restricted to -9 meV, where the intensity of the spectrum is approximately zero for all temperatures (without noise), and the cutoff energy of the spectrometer at around -0.5 meV. Although an exact mathematical description of the slope is very difficult since it requires an integration over the product of Boltzmann distribution and Lindhard-Mermin line shape, we can observe a steady increase of integrated area with the temperature, which is a main characteristic of the anti-Stokes process.

Chapter 6

GaAs quantum wells in external magnetic fields

At the beginning of Chap. 4 we explained the lifted spin degeneracy of the conduction band with the broken space inversion symmetry of zinc-blende structures and regarded the spin-orbit field as an effective magnetic field within the quantum well plane. Another possible approach to lift the spin degeneracy would be an external magnetic field, which leads to a Zeeman splitting in the band structure. If the field is applied perpendicular to the quantum well plane, Kramers doublets are destroyed and spin subbands are energetically separated. Additionally, a Landau quantization may be observed when the external magnetic field is strong enough. Within this chapter, we will give a short introduction to the Landau quantization in a quantum well structure and demonstrate the smooth transition of a 2DES towards a Landau quantized system by applying a mainly perpendicular magnetic field.

6.1 Landau quantization

Electrons in a 2DES are generally free to move within the quantum well plane, however, an application of a perpendicular magnetic field forces free electrons to move on circular orbits with a defined cyclotron frequency of

$$\omega_c = \frac{eB}{m^*} . \quad (6.1)$$

The resonant absorption of an external radiation, which matches this angular frequency ω_c , is called cyclotron resonance. An essential magnitude concerning the observation of this resonance effect is $\omega_c\tau$ (τ : average scattering time), which describes the number of orbital motions before the electron is scattered by, e. g., crystal impurities or interfaces. If an orbital motion is completed ($\omega_c\tau > 1$) and the electron is able to interfere with itself, a separation of the continuous 2D

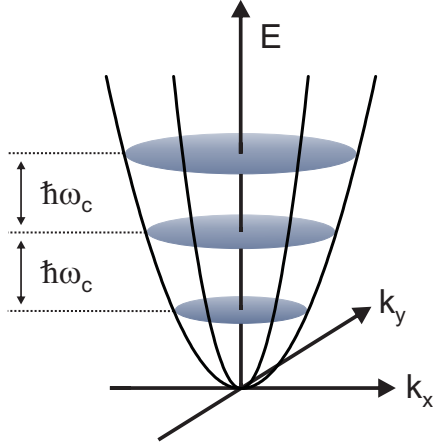


Figure 6.1: An external magnetic field perpendicular to the quantum well plane leads to a quantization along the energy axis. These Landau levels are separated by $\hbar\omega_c$.

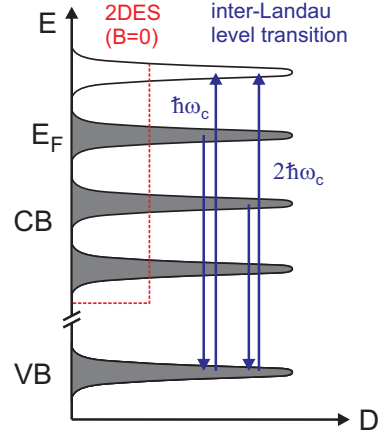


Figure 6.2: The constant density of states (D) of the 2DES evolves under a perpendicular magnetic field to broadened δ -peaks, which are occupied up to the Fermi energy E_F .

energy spectrum into quantized energy levels E_n appears (see Fig. 6.1). The total energy of these so called Landau levels in the i -th subband is given by [Win03]

$$E_{n,s}^i = E_z^i + (n + \frac{1}{2}) \hbar\omega_c + sg^* \mu_B B, \quad (6.2)$$

with the subband energy E_z^i . Here, $n = 0, 1, 2, \dots$ describes the Landau quantum number, $s = \pm \frac{1}{2}$ the spin quantum number, g^* the effective g-factor and $\mu_B = \frac{e\hbar}{2m_e}$ the Bohr magneton. The second term in Eq. (6.2) corresponds to the Landau splitting and yields a constant distance of $\Delta E_L = \hbar\omega_c$ between neighbored Landau levels. With the last term, the Zeeman splitting is taken into account, which would lead to an additional splitting of Landau levels by $\Delta E_Z = g^* \mu_B B$.

Figure 6.2 illustrates the density of states for a nonzero magnetic field, while the Zeemann splitting is here neglected for simplicity. Instead of a constant energy distribution like in a 2DES, Landau levels are given by discrete δ -peaks, but are broadened under experimental conditions due to scattering effects. The occupation of Landau levels is limited by the Fermi energy, as indicated by the gray shaded areas. In a quantum mechanical sense, cyclotron resonances may be described as inter-Landau level transitions, where an electron is lifted from an occupied to an unoccupied level. Accordingly, higher cyclotron resonances can be ascribed to transitions between remote Landau levels. For Raman measurements also the valence band needs to be considered since it provides the important intermediate state and determines the resonance.

The degeneracy N_L of Zeeman-split Landau levels strongly depends on the magnetic field strength and reads [Iba09]

$$N_L = \frac{eB}{h}. \quad (6.3)$$

Furthermore, the filling factor ν , which determines the number of filled Landau levels, is given by [Miu08]

$$\nu = \frac{N_s}{N_L} = \frac{hN_s}{eB}, \quad (6.4)$$

with the carrier density N_s and the Planck constant h . If the magnetic field is increased, all Landau levels shift to higher energies and the level separation as well as the degeneracy rises. As a consequence, Landau levels pass through the Fermi energy, what is accompanied by a depopulation of this level and a jump of E_F down to the next occupied level. This oscillating behavior of Fermi energy accounts for a $1/B$ -periodic oscillation in many physical parameters like the conductivity (Shubnikov-de Haas effect) or the magnetic moment (de Haas-van Alphen effect).

In electronic Raman scattering, inter-Landau level transitions, as sketched in Fig. 6.2, are generally forbidden since only interband transitions between conduction and valence band states with the same Landau quantum number ($\Delta n = 0$) are allowed [Wor83, Jus03]. Note that for far-infrared dipole transitions, the selection rule $\Delta n = \pm 1$ holds. The restraint for Raman scattering, however, may be broken by means of an in-plane wave vector q , while transitions with $\Delta n \neq 0$ appear when q reaches the strength of $1/l_0$ [Wor83, Jus03]. The magnetic length l_0 is defined as

$$l_0 = \sqrt{\frac{\hbar}{eB}} \quad (6.5)$$

and describes in a classical picture the smallest possible radius of cyclotron motion, while the radius of a higher Landau level corresponds to $r_n = \sqrt{2n+1}l_0$ [Miu08]. In fact, a magnetic field strength of $B \sim 0.1$ T would already cause a strong enough $1/l_0$ to exceed q in the Raman measurement, if a typical wave vector of $q \sim 10^7 \text{ m}^{-1}$ is assumed. However, several publications observed cyclotron resonances in Raman spectra due to a relaxation of the parity selection rule by the heavy-hole-light-hole mixing of the resonant intermediate state in the valence band [Pin88b, Bro93, Sch97]. Therefore, we can presume that an observation of inter-Landau level transitions should not be prevented by the selection rule, since our measurements are also based on a resonant behavior with the valence band.

6.2 Low and moderate magnetic fields

In the following, we discuss experimental results of sample B, which was mounted on a 25° -wedge in the magnetic field cryostat depicted in Fig. 2.23. This configuration features a splitting of externally applied field into a component parallel to the quantum well, given by $B_{\parallel} = B \sin \theta$, and a component perpendicular to it, $B_{\perp} = B \cos \theta$, where B is the total field of the solenoid. For a fixed tilt angle of $\theta = 25^\circ$, we obtain a large field strength for the perpendicular component according to $\cos \theta \sim 0.91$, while the in-plane field has less influence with $\sin \theta \sim 0.42$. If

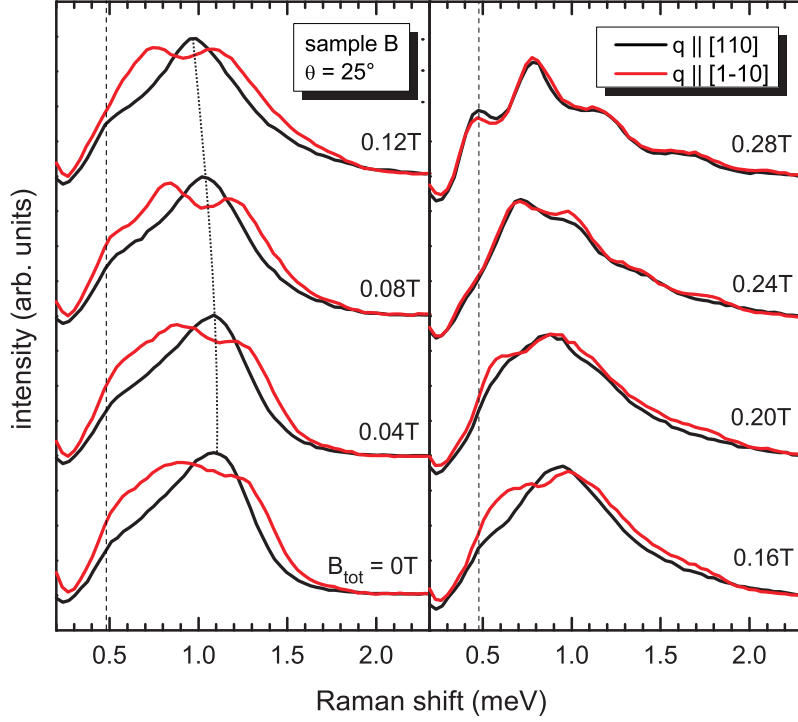


Figure 6.3: Depolarized spectra of sample B with a fixed tilt angle of $\theta = 25^\circ$. The comparison shows the intrasubband SDE for the directions with maximum (red spectra) and minimum spin splitting (black spectra). An external magnetic field is applied up to $B = 0.28\text{ T}$, while the magnetic field perpendicular to the quantum well plane is given by $B_\perp \approx 0.91 B$. The dashed line represents the cutoff energy of the Raman spectrometer and the dotted line is a guide to the eye.

we consider the relation $B_{SO} = \frac{\Delta E_S}{g^* \mu_B}$, we can deduce the maximum in-plane spin-orbit field of sample B as $B_{SO} = 15.5\text{ T}$, wherein an effective g-factor of $|g^*| = 0.2$ for a 12 nm-wide GaAs/AlGaAs quantum well [Yug07] and a spin splitting of $\Delta E_{S,[1\bar{1}0]} = 0.19\text{ meV}$ (see Chap. 4.2.4) were used. Obviously, this prevalent spin-orbit field is strong enough that we do not expect a measurable impact of the external in-plane field within the investigated B -field range.

Figure 6.3 shows a direct comparison in depolarized scattering geometry between the directions where the spin splitting has its maximum ($q \parallel [1\bar{1}0]$) and its minimum ($q \parallel [110]$), respectively. The external magnetic field is increased in small steps up to $B = 0.28\text{ T}$ and the laser energy was kept fixed during the whole measurement, since no drastic change in resonance condition could be observed here. Moreover, the cutoff frequency of the spectrometer is symbolized by the dashed line just below 0.5 meV . Without applied magnetic field, we can recognize the intrasubband SDE with the double peak structure in the red colored spectrum and the single peak in black with the asymmetric Lindhard-Mermin line shape right in between. An increase of external magnetic field leads to a sharpening of the double peak for the first steps, however, a blurring of the structure starts again at $B = 0.12\text{ T}$. Additionally we can observe a slight redshift of peak energies, while the slope at the high energy cutoff is flattened to some extent. This behavior is

essentially similar in the perpendicular in-plane direction, where the energy shift is marked by the dotted line. Within this field range of the left panel, the spin splitting appears to be nearly constant but slightly shifted to lower energies. Proceeding to higher magnetic fields, depicted in the right panel of Fig. 6.3, the main characteristic with respect to $B = 0$ gets lost and both spectra tend to assimilate each other, which is mainly accomplished at a field strength of $B = 0.24$ T. For $B = 0.28$ T, the in-plane directions are indistinguishable and the spectra reveal multiple cyclotron resonances. These measurements reflect the smooth transition of the excitation spectrum of a 2DES towards a Landau quantized system. Such a transition was already reported in different publications [Ric00, Jus03], however, neither of them investigated a sample with a huge anisotropy in the spin splitting and hence, these reports focused only on a single in-plane direction.

A two dimensional behavior is generally expected as long as $\hbar\omega_c < \hbar\Gamma$, where $\hbar\omega_c$ describes the energy separation of the Landau level and $\hbar\Gamma$ corresponds to its broadening [Ric00]. Furthermore we can definitely identify a wave-vector conserving mechanism for the field range, where both spectra are still distinguishable. The open question, whether the unmodified peak separation for a field up to 0.12 T can be still ascribed to the spin splitting of the 2DES, yet remains. An analytical calculation by R. Winkler predicts a vanishing spin splitting at $B_\perp = 0.8$ T for a system with a dominating Dresselhaus spin-orbit field, using a 15 nm-wide GaAs quantum well and a carrier density of $N_s = 2 \times 10^{15} \text{ m}^{-2}$ [Win03]. The zero crossing of the spin splitting stems from the negative g -factor for GaAs quantum wells and would consequently lead to a decreasing spin splitting with increasing field strength until zero is reached. An important difference between the calculated and the here depicted system is the spin-orbit field, which features an approximately balanced ratio of Dresselhaus and Rashba contribution in sample B, whereas a dominating Dresselhaus field is considered for the calculation. Therefore, a constant peak separation observable at very small fields ($B < 0.12$ T) may not be contradictory to the results of R. Winkler. At higher fields, the signature of an excitation in the 2DES vanishes and the spin splitting is no longer visible. An exact explanation of these complex observations would require a specific calculation with equal spin-orbit fields, however, an analytical treatment is only possible for either a dominating Rashba or a dominating Dresselhaus field [Win03]. Consequently, a numerical approach would be indispensable for this system.

For even higher magnetic fields, it is sufficient to consider only a single direction, since no variation of spectra concerning different in-plane directions is present any more. A series of spectra with a total magnetic field ranging from 0.3 T up to 0.7 T is depicted in Fig. 6.4 (a), where intensities are shifted for a cleared picture. The measurement reveals a discretizing behavior with cyclotron resonances evolving out of the initial excitation spectrum of the 2DES. Obviously, the emergence energy of the cyclotron resonance strongly depends on the strength of the transferred wave vector, which could be confirmed by corresponding measurements with a higher tilt angle (not shown) and by means of Ref. [Jus03]. This implies that a larger wave vector would consequently lead to an emergence of inter-Landau

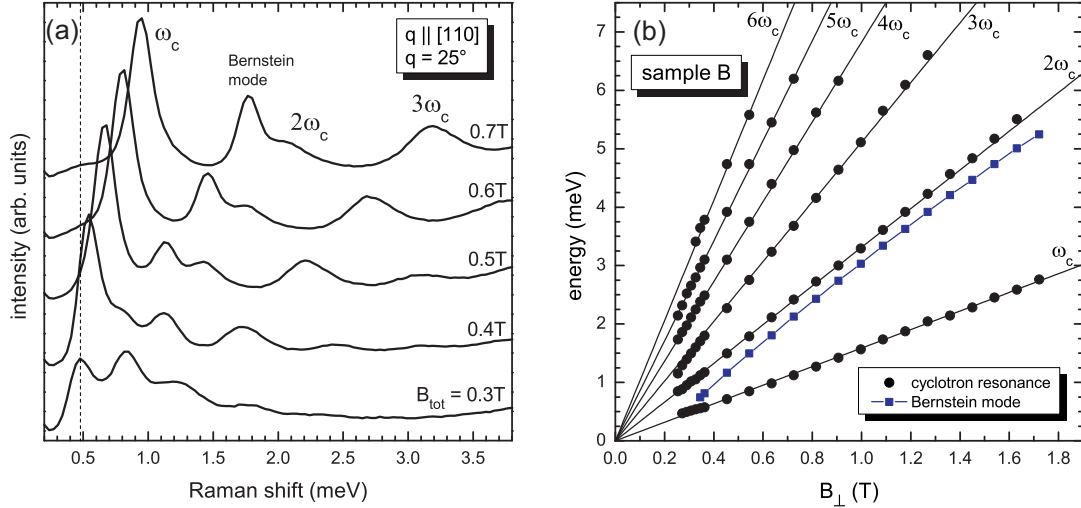


Figure 6.4: (a) Depolarized Raman spectra of sample B with an applied magnetic field between $B = 0.3 - 0.7 \text{ T}$. A wave vector with a tilt angle of $\theta = 25^\circ$ is transferred along $[110]$ and intensities are shifted for a cleared picture. (b) Standard Landau fan diagram where extracted peak positions are plotted against the external magnetic field perpendicular to the quantum well plane.

level transitions at higher energies, what again underlines the claim of a wave-vector conserving mechanism for this field strength. Generally, a discretization of excitation energy occurs when the cyclotron energy exceeds the homogeneous broadening of the excitations [Jus03]. As expected, all emerged inter-Landau level transitions shift to higher energies as the external magnetic field is increased. The narrow peak on the low-energy side of the first harmonic $2\omega_c$ is called Bernstein mode and will be discussed in detail in the next section, here we focus only on the depicted inter-Landau level transitions.

Figure 6.4(b) shows all extracted peak positions of this moderate field range plotted against the perpendicular magnetic field. The linear dependency in such a standard Landau fan diagram is very well observable and allows a determination of effective electron mass via Eq. (6.1). We can deduce for the cyclotron resonance, which corresponds to a transition between neighboring Landau levels, an effective mass of $m^* = 0.073 m_e$, whereas this value decreases successively for higher harmonics down to $m^* = 0.068 m_e$ for $6\omega_c$. Such a discrepancy of effective mass probably stems from the nonparabolicity of the conduction band [Eke89, Ruf90] and may be explained by regarding the corresponding energy dispersion of an initial 2DES. An electron, which is subjected to a transition between neighboring Landau levels, would experience in the case of a nonparabolic band another curvature of energy dispersion as an electron of a transition between remote levels, and this would consequently lead to different effective masses for different transitions. Considering that the effective mass generally increases with increasing energy [Ruf90, Miu08], we can assume for higher harmonics a transition from deeper Landau levels to an unoccupied level just above the Fermi energy.

At the end of this section we note that the inter-Landau level transitions have

been detected in polarized scattering geometry as well, but no significant variation between both spectra was observable. This was also reported in Ref. [Sch97] and indicates the single-particle character of these excitations.

6.3 The magnetoplasmon and Bernstein modes

Before we proceed to higher external fields, we turn our attention to the narrow mode in Fig. 6.4(a), visible on the low energy side of the first harmonic $2\hbar\omega_c$. For a detailed investigation, we now consider polarized spectra, where this narrow mode also appears similar to cyclotron resonances. The polarized scattering geometry further allows the occurrence of an additional peak, which can be attributed to the plasmon frequency discussed in Chap. 4.2.5. In the presence of a perpendicular magnetic field, the plasmon is modified by the cyclotron resonance and the frequency ω_{mp} of this magnetoplasmon is then given by [Ban96]

$$\omega_{mp}(B)^2 = \omega_p(0)^2 + \omega_c(B)^2. \quad (6.6)$$

Without magnetic field, this mode is determined by the plasmon frequency ω_p for a given wave vector, whereas for high fields an asymptotic approach to the cyclotron frequency ω_c is observable. If some lateral inhomogeneity is present in the system, a nonlocal interaction between the plasmon and the harmonics of the cyclotron resonance leads to an emergence of so called Bernstein modes [Bat85, Ban96, Ric00].

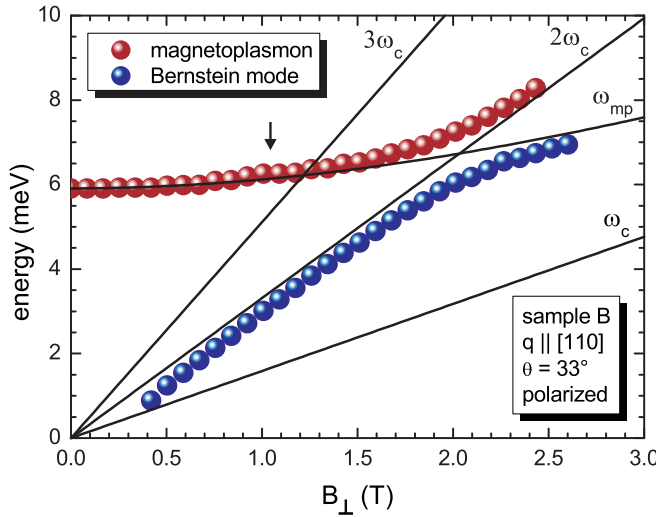


Figure 6.5: *Extracted peak positions of sample B plotted against the perpendicular magnetic field. The analysis refers to polarized Raman spectra with a transferred wave vector parallel to [110] and a tilt angle of $\theta = 33^\circ$. The theoretical dispersion of the magnetoplasmon was calculated with Eq. (6.6). An anticrossing behavior is observable near $2\omega_c \sim \omega_{mp}$.*

Figure 6.5 shows the extracted peak positions of sample B dependent on the external magnetic field perpendicular to the quantum well plane. As already announced, we refer here to Raman spectra obtained in polarized scattering configuration and consider now a tilt angle of $\theta = 33^\circ$ with a wave-vector transfer parallel to [110]. Note that polarized spectra do not differ for various in-plane directions. The dispersion of the magnetoplasmon was calculated by means of Eq. (6.6) and is plotted as a solid line. Measured values of the cyclotron resonance and its harmonics are also symbolized by solid lines to focus on the main aspect of this

section. The measured peak of the Bernstein mode emerges out of the cyclotron resonance and approaches the first harmonic, where it sticks on the low energy side until its energy comes close to the calculated energy of the magnetoplasmon. At this point we can observe an anticrossing behavior with the measured peak of the magnetoplasmon bending towards the first harmonic and a Bernstein mode following the calculated dispersion of the magnetoplasmon. This interaction with an anticrossing near $\omega_{mp} \sim n_c \omega_c$ ($n_c = 2, 3, \dots$) is very well predicted and can be described by means of a classical nonlocal theory [Bat85, Bat86, Ban96]. In fact, an interaction with higher harmonics should also lead to a series of Bernstein modes with a much weaker intensity [Ric00]. Although another Bernstein mode could not be observed in our measurements, we can identify a slight anomaly as a small hint on the anticrossing of the magnetoplasmon and the second harmonic, which is indicated in Fig. 6.5 by the black arrow.

An essential condition for the occurrence of Bernstein modes is a transferred wave vector, since they are not present for $q = 0$ [Ric00]. This leads to the assumption of a wave-vector conserving mechanism at least up to a perpendicular field of $B_\perp \approx 2.5$ T, where the Bernstein mode is still detectable. An exact determination of field strength, which would be required for a breakdown of wave-vector conservation, is not possible here, because the Bernstein mode is superimposed by PL traces for an external perpendicular field above 2.5 T.

6.4 High magnetic fields

In the last section of this chapter we further increase the external magnetic field up to $B = 5$ T, which corresponds for a tilt angle of $\theta = 25^\circ$ to $B_\perp \approx 4.5$ T for the perpendicular field of the quantum well plane. At a certain field strength, no inter-Landau level transitions or Bernstein modes are observable any more and the spectrum is dominated by the photoluminescence of different Landau levels.

Figure 6.6 (a) and (c) show a comparison of PL traces from sample A and sample B in absolute energy. The perpendicular magnetic field is increased in both waterfall plots from $B_\perp = 0$ for the bottom spectrum up to $B_\perp = 4.5$ T for the uppermost one. At first sight, we can identify a roughly similar behavior, where the characteristic photoluminescence of the 2DES at zero field splits up into various peaks for an increasing magnetic field. These peaks can be ascribed to Landau levels and in a simplified picture, as introduced in Chap. 6.1, we would assume an equal spacing between each level. In the case of sample B, a magnetic field of $B_\perp = 4.5$ T would therefore cause a separation of Landau levels by $\Delta E_L = \hbar \omega_c = 7.2$ meV. The expected position of the second deepest Landau level with respect to the main peak is marked in subframe (c) by the black arrow. Obviously, the spectrum is more complex than this simple picture suggests. In exemplified models, often the conduction band is considered only and the valence band is assumed to be flat, but in real systems also the valence band is Landau quantized under high magnetic fields and reveals a rather complex behavior due to heavy-hole-light-hole mixing for $\mathbf{k} \neq 0$ [Sch97]. Hence we can ascribe the dou-

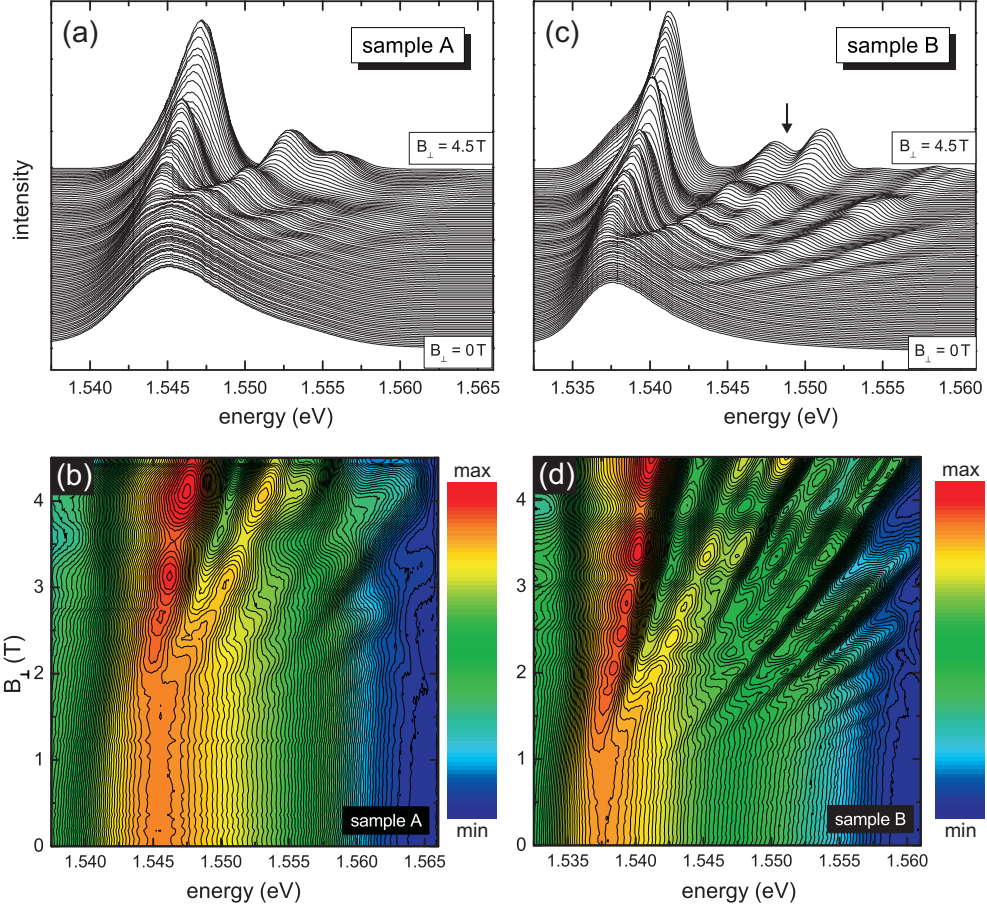


Figure 6.6: (a) Waterfall plot of PL spectra from sample A, obtained for a perpendicular magnetic field between $B_{\perp} = 0$ and $B_{\perp} = 4.5$ T. (b) False-color plot with spectra from (a), where the intensity scales with the color. Contours of constant intensity are represented by solid lines. (c) and (d): Same as (a) and (b), but for sample B.

ble peak structure around the black arrow most likely to a split final state of the photoluminescence in the valence band. We note that an impact of Zeeman splitting on the Landau levels is not detectable in this measurement, since a maximum value of $\Delta E_Z = 0.06$ meV, achieved for $B = 5$ T, is negligibly small here.

For a more detailed analysis, we consider the presented results in a false-color plot depicted in Fig. 6.6(b) and (d). The intensity is scaled by the color and contours of constant intensity are symbolized by black lines. As expected, all Landau levels shift nearly linearly to higher energies and the separation rises as the magnetic field is increased. If we compare the results of both samples, we can identify a more distinct behavior for sample B with first Landau levels emerging at $B_{\perp} \approx 1$ T, giving rise to a characteristic fan structure observable over the whole energy range. Whereas in sample A, a splitting of Landau levels is recognizable not before $B_{\perp} \approx 2$ T and a rather weak emphasis of each level is revealed. This discrepancy can be attributed to a different electron mobility, which is directly linked to the average scattering time by $\mu = \frac{e\tau}{m^*}$ [Miu08]. Since $\omega_c\tau > 1$ is the

essential criteria for the occurrence of Landau levels, a dependency on the electron mobility is straightforward. Following this consideration, we can conclude a higher mobility for sample B compared to sample A, what is confirmed by the nominal sample parameters. But an impact of the mobility is not limited to the emergence of Landau levels, also the broadening is affected. For a high mobility, electrons feature a longer mean free path and the scattering due to impurities or interfaces is reduced, which leads to a low broadening of Landau levels. This can be observed in Fig. 6.6 (d) by the narrow width of each string, which describes a single Landau level, while all strings in subframe (b) are broadened due to a lower scattering time. Another interesting point is the occurrence of maxima in PL intensity, which appear, individually for both samples, in all given Landau levels at approximately the same perpendicular field strength. This behavior follows a $1/B$ periodicity and stems from the oscillating Fermi energy described in Chap. 6.1.

At the end of this chapter we would like to note that sample A was also investigated for lower magnetic fields, but due to a lower mobility, results are less meaningful and not as promising as results from sample B. Nevertheless, we could extract the effective mass for sample A from measurements of inter-Landau level transitions and use the obtained value throughout the work.

Chapter 7

Conclusion

A very interesting phenomenon called the persistent spin helix emerged during the last decade of spintronics research. Its prevalent spin-rotation symmetry is for a (001)-oriented 2DES a consequence of equal Rashba and Dresselhaus spin-orbit fields and yields long spin lifetimes as well as a Fermi contour with two shifted circles of anti parallel spin states. The overall aim of this work was to investigate the persistent spin helix state by means of inelastic light scattering and hence contribute to current results in this research field. For that purpose we examined two similar samples, where both feature a 12 nm-wide GaAs quantum well system but differ in terms of orientation of the Rashba field. A verification was achieved in each structure through the revelation of a maximum anisotropy in the spin splitting of the conduction band, which is a sufficient signature of the persistent spin helix.

Experimental results started in this thesis with a depiction of intersubband excitations in different quantum well structures. This part was intended to survey the previously gained knowledge about the scattering process and provide a comprehensive characterization of investigated samples. Series with a tuned laser energy underlined the importance of a resonant intermediate state in the valence band, independent from the size of the quantum well width. Further studies on a wave-vector transfer in a 25 nm-wide quantum well structure revealed the dispersion of electronic excitations in a 2DES and confirmed the phenomenological picture of collective modes, which are Landau damped once their energies enter the single-particle continua. A comparison with results of a 12 nm-wide quantum well demonstrated the impact of the subband spacing on the manifestation of collective and single-particle modes. In accordance to Ref. [Unu04], we found a vanishing occurrence of collective CDE and SDE for a decreasing well width. The simultaneous broadening of single-particle excitations probably stems from energy variations concerning a quantum well inhomogeneity and a short lifetime of excitations due to a very fast relaxation via phonons. An attempt to manipulate the subband structure with an electric gate indicated a rather low influence of

an external field on intersubband excitations, even though a total carrier-density modification of 20 % could be realized.

In the second and main part of this work, we focused on intrasubband excitations with a transferred wave vector and a verification of the persistent spin helix. In (001)-grown quantum well structures, the intrasubband SDE is restricted in a good approximation to spin-flip excitations within a single subband. This provides a direct approach to detect the spin splitting in the conduction band. Assuming a positive Rashba field, a persistent spin helix structure is characterized by a special anisotropy with a maximum spin splitting for the $[110]$ direction, while the splitting vanishes for the perpendicular $[\bar{1}\bar{1}0]$ direction. We investigated a 12 nm-wide GaAs quantum well structure and verified a balanced ratio of Rashba and Dresselhaus coupling constants for the first time by means of electronic Raman scattering. A maximum spin splitting of $\Delta E_{S,[110]} = 0.18$ meV and a corresponding PSH wavelength of $\lambda_{PSH} \approx 5.5 \mu\text{m}$ compare very well with previously published results obtained with a sample from the same wafer, but independently measured by time- and spatially resolved Kerr microscopy [Wal12a]. Furthermore we could demonstrate with another 12 nm-wide GaAs quantum well structure that a negative Rashba field, induced by a reversed emphasis of modulation doping, causes a manifestation of persistent spin helix with interchanged crystal directions. This outlines inelastic light scattering as a powerful tool to characterize the spin splitting and even reveal a PSH state in a 2DES. However, the obvious downside of this measurement technique is a rather low accuracy for the resolution of a spin splitting close to zero. Due to a finite broadening of experimental peaks, an exact determination of the persistent spin helix state is only possible within certain error limits and ideally requires a second independent evidence. An additional study with an external electric field was conducted to investigate its impact on the spin splitting. Although the Rashba field should be affected by an electrical gate process, no real hint on a variation of spin splitting could be detected in the accessible field range.

Another possibility to influence the band structure is an external magnetic field. Starting from a 2DES and the corresponding intrasubband SDE, we demonstrated a smooth transition to a Landau quantized system by applying a magnetic field, which is mainly perpendicular to the quantum well plane. For small magnetic fields, we could observe an assimilation of the initial anisotropic spin splitting, while the characteristic shape of the intrasubband SDE faded and inter-Landau level transitions emerged when the field strength was increased. A theoretical clarification regarding the behavior of the spin splitting during the transition would have been very helpful here, however, the required numerical treatment could not be completed within the timeframe of this work and is consequently left for future considerations. Speaking of worthwhile prospects, an investigation with a pure in-plane magnetic field would be a very promising project, since it represents a direct approach to affect the in-plane spin-orbit field without the side effect of an emerging Landau quantization. For a (001)-oriented 2DES with equal Rashba and Dresselhaus coupling constants, a spin-orbit field with a unidirectional ori-

entation within the quantum well plane is expected. This spin-orbit field may be enhanced or attenuated by means of an external in-plane field, which would result in a modified spin splitting. A comparison between the experimentally determined magnetic field, necessary to compensate the spin-splitting, and the calculated value (see, e. g., Chap. 6.2) may give some indication about collective effects of the spin-orbit field. Such an impact of collective interactions is very well predicted [Ull03] and has already been observed for intersubband transitions, where the collective spin-orbit field was enhanced by a factor of 5 compared to the spin-orbit field of a non-interacting system [Bab12]. A detailed investigation of this interesting effect with a system characterized by a unidirectional symmetry of the spin-orbit field would be a challenging task and is left as a strong motivation for the future.

Bibliography

- [Abs79] G. Abstreiter and K. Ploog, *Inelastic Light Scattering from a Quasi-Two-Dimensional Electron System in GaAs-Al_xGa_{1-x}As Heterojunctions*, Phys. Rev. Lett. **42**, 1308 (1979). [Cit. on p. 2, 35]
- [Abs88] G. Abstreiter, T. Egeler, S. Beeck, A. Seilmeier, H. Hübner, G. Weimann, and W. Schlapp, *Electronic excitations in narrow GaAs/Al_xAl_xGa_{1-x}As quantum well structures*, Surface Science **196**, 613 (1988). [Cit. on p. 40]
- [Ada85] S. Adachi, *GaAs, AlAs, and Al_xGa_{1-x}As: Material parameters for use in research and device applications*, J. Appl. Phys. **58**, 1 (1985). [Cit. on p. 8]
- [Alt14] P. Altmann, M. P. Walser, C. Reichl, W. Wegscheider, and G. Salis, *Suppressed decay of a laterally confined persistent spin helix*, Phys. Rev. B **90**, 201306(R) (2014). [Cit. on p. 55]
- [And82] T. Ando, A. B. Fowler, and F. Stern, *Electronic properties of two-dimensional systems*, Rev. Mod. Phys. **54**, 437 (1982). [Cit. on p. 28]
- [Ash13] N. W. Ashcroft and D. N. Mermin, *Festkörperphysik*, Oldenbourg Verlag (2013). [Cit. on p. 7, 10]
- [Ave99] N. S. Averkiev and L. E. Golub, *Giant spin relaxation anisotropy in zinc-blende heterostructures*, Phys. Rev. B **60**, 15582 (1999). [Cit. on p. 47]
- [Ave06] N. S. Averkiev, L. E. Golub, A. S. Gurevich, V. P. Evtikhiev, V. P. Kochereshko, A. V. Platonov, A. S. Shkolnik, and Y. P. Efimov, *Spin-relaxation anisotropy in asymmetrical (001) Al_xGa_{1-x}As quantum wells from Hanle-effect measurements: Relative strengths of Rashba and Dresselhaus spin-orbit coupling*, Phys. Rev. B **74**, 033305 (2006). [Cit. on p. 47]
- [Bab12] F. Baboux, F. Perez, C. A. Ullrich, I. D’Amico, J. Gómez, and M. Bernard, *Giant Collective Spin-Orbit Field in a Quantum Well: Fine Structure of Spin Plasmons*, Phys. Rev. Lett. **109**, 166401 (2012). [Cit. on p. 56, 97]
- [Bab13] F. Baboux, F. Perez, C. A. Ullrich, I. D’Amico, G. Karczewski, and T. Wojtowicz, *Coulomb-driven organization and enhancement of spin-orbit fields in collective spin excitations*, Phys. Rev. B **87**, 121303 (2013). [Cit. on p. 56]

- [Ban96] D. Bangert, R. Stuart, H. Hughes, D. Ritchie, and J. Frost, *Bernstein modes in grating-coupled 2DEGs*, Semiconductor Science and Technology **11**, 352 (1996). [Cit. on p. 91, 92]
- [Bas81] G. Bastard, *Superlattice band structure in the envelope-function approximation*, Phys. Rev. B **24**, 5693 (1981). [Cit. on p. 9]
- [Bat85] E. Batke, D. Heitmann, J. P. Kotthaus, and K. Ploog, *Nonlocality in the Two-Dimensional Plasmon Dispersion*, Phys. Rev. Lett. **54**, 2367 (1985). [Cit. on p. 91, 92]
- [Bat86] E. Batke, D. Heitmann, and C. W. Tu, *Plasmon and magnetoplasmon excitation in two-dimensional electron space-charge layers on GaAs*, Phys. Rev. B **34**, 6951 (1986). [Cit. on p. 92]
- [Bel08] V. V. Bel'kov, P. Olbrich, S. A. Tarasenko, D. Schuh, W. Wegscheider, T. Korn, C. Schüller, D. Weiss, W. Prettl, and S. D. Ganichev, *Symmetry and Spin Dephasing in (110)-Grown Quantum Wells*, Phys. Rev. Lett. **100**, 176806 (2008). [Cit. on p. 15]
- [Ber90] M. Berz, J. F. Walker, P. von Allmen, E. F. Steigmeier, and F. K. Reinhart, *Strong intermediate-state effects in exciton-mediated electronic intrasubband scattering in multiple-quantum-well structures*, Phys. Rev. B **42**, 11957 (1990). [Cit. on p. 56]
- [Ber06] B. A. Bernevig, J. Orenstein, and S.-C. Zhang, *Exact $SU(2)$ Symmetry and Persistent Spin Helix in a Spin-Orbit Coupled System*, Phys. Rev. Lett. **97**, 236601 (2006). [Cit. on p. 2, 47, 53, 55, 75]
- [Bha95] A. Bhatti, D. Richards, H. Hughes, D. Ritchie, J. Frost, and G. Jones, *Plasmon dispersion and electron heating in a drifting two-dimensional electron gas*, Phys. Rev. B **51**, 2252 (1995). [Cit. on p. 81, 82]
- [Bha96] A. S. Bhatti, D. Richards, H. P. Hughes, and D. A. Ritchie, *Spatially resolved Raman scattering from hot acoustic and optic plasmons*, Phys. Rev. B **53**, 11016 (1996). [Cit. on p. 81]
- [Blu70] F. A. Blum, *Inelastic Light Scattering from Semiconductor Plasmas in a Magnetic Field*, Phys. Rev. B **1**, 1125 (1970). [Cit. on p. 33]
- [Bro93] G. Brozak, B. V. Shanabrook, D. Gammon, and D. S. Katzer, *Collective intersubband spin- and charge-density excitations in tilted magnetic fields*, Phys. Rev. B **47**, 9981 (1993). [Cit. on p. 87]
- [Bur80] E. Burstein, A. Pinczuk, and D. Mills, *Inelastic light scattering by charge carrier excitations in two-dimensional plasmas: Theoretical considerations*, Surface Science **98**, 451 (1980). [Cit. on p. 31, 32]
- [Byc84] Y. A. Bychkov and I. Rashba, *Properties of a 2D electron gas with lifted spectral degeneracy*, JETP Lett. **39**, 78 (1984). [Cit. on p. 1, 46, 51]
- [Car82] M. Cardona, *Light Scattering in Solids, II*, Springer (1982). [Cit. on p. 82]

- [Che76] J. R. Chelikowsky and M. L. Cohen, *Nonlocal pseudopotential calculations for the electronic structure of eleven diamond and zinc-blende semiconductors*, Phys. Rev. B **14**, 556 (1976). [Cit. on p. 7]
- [Che14] Y. S. Chen, S. Fält, W. Wegscheider, and G. Salis, *Unidirectional spin-orbit interaction and spin-helix state in a (110)-oriented GaAs/(Al,Ga)As quantum well*, Phys. Rev. B **90**, 121304(R) (2014). [Cit. on p. 75]
- [Cro05] S. A. Crooker and D. L. Smith, *Imaging Spin Flows in Semiconductors Subject to Electric, Magnetic, and Strain Fields*, Phys. Rev. Lett. **94**, 236601 (2005). [Cit. on p. 72]
- [Dö4] S. Döhrmann, D. Hägele, J. Rudolph, M. Bichler, D. Schuh, and M. Oestreich, *Anomalous Spin Dephasing in (110) GaAs Quantum Wells: Anisotropy and Intersubband Effects*, Phys. Rev. Lett. **93**, 147405 (2004). [Cit. on p. 75]
- [Dan89] G. Danan, A. Pinczuk, J. P. Valladares, L. N. Pfeiffer, K. W. West, and C. W. Tu, *Coupling of excitons with free electrons in light scattering from GaAs quantum wells*, Phys. Rev. B **39**, 5512 (1989). [Cit. on p. 32, 33]
- [Dat90] S. Datta and B. Das, *Electronic analog of the electrooptic modulator*, Appl. Phys. Lett. **56**, 665 (1990). [Cit. on p. 1]
- [Dav98] J. H. Davies, *Low-Dimensional Semiconductors: An Introduction*, Cambridge University Press (1998). [Cit. on p. 12]
- [Dol14] T. Dollinger, M. Kammermeier, A. Scholz, P. Wenk, J. Schliemann, and K. Richter, *Signatures of spin-preserving symmetries in two-dimensional hole gases*, Phys. Rev. B **90**, 115306 (2014). [Cit. on p. 55]
- [Dre55] G. Dresselhaus, *Spin-Orbit Coupling Effects in Zinc Blende Structures*, Phys. Rev. **100**, 580 (1955). [Cit. on p. 1, 5, 6, 46, 47, 48]
- [Dru81] T. J. Drummond, H. Morkoç, K. Hess, and A. Y. Cho, *Experimental and theoretical electron mobility of modulation doped $Al_xGa_{1-x}As$ /GaAs heterostructures grown by molecular beam epitaxy*, J. Appl. Phys. **52**, 5231 (1981). [Cit. on p. 11]
- [DS90] S. Das Sarma, R. Jalabert, and S.-R. E. Yang, *Band-gap renormalization in semiconductor quantum wells*, Phys. Rev. B **41**, 8288 (1990). [Cit. on p. 16]
- [DS98] S. Das Sarma and E. H. Hwang, *Plasmons in Coupled Bilayer Structures*, Phys. Rev. Lett. **81**, 4216 (1998). [Cit. on p. 31]
- [DS99] S. Das Sarma and D.-W. Wang, *Resonant Raman Scattering by Elementary Electronic Excitations in Semiconductor Structures*, Phys. Rev. Lett. **83**, 816 (1999). [Cit. on p. 25, 31, 33]
- [Dya71a] M. I. Dyakonov and V. I. Perel, *Spin Orientation of electrons associated with the interband absorption of light in semiconductors*, Sov. Phys. JETP **33**, 1053 (1971). [Cit. on p. 48, 53, 75]

- [Dya71b] M. I. Dyakonov and V. I. Perel, *Spin relaxation of conduction electrons in noncentrosymmetric semiconductors*, Sov. Phys. Solid State **13**, 3023 (1971). [Cit. on p. 53]
- [Dya86] M. I. Dyakonov and V. Kachorovskii, *Spin relaxation of two-dimensional electrons in noncentrosymmetric semiconductors*, Sov. Phys. Semicond. **20**, 110 (1986). [Cit. on p. 75]
- [Dya08] M. Dyakonov, *Spin Physics in Semiconductors*, Springer (2008). [Cit. on p. 46]
- [Ege90] T. Egeler, G. Abstreiter, G. Weimann, T. Demel, D. Heitmann, P. Grambow, and W. Schlapp, *Anisotropic plasmon dispersion in a lateral quantum-wire superlattice*, Phys. Rev. Lett. **65**, 1804 (1990). [Cit. on p. 35]
- [Eke89] U. Ekenberg, *Nonparabolicity effects in a quantum well: Sublevel shift, parallel mass, and Landau levels*, Phys. Rev. B **40**, 7714 (1989). [Cit. on p. 61, 90]
- [Ell54] R. J. Elliott, *Theory of the Effect of Spin-Orbit Coupling on Magnetic Resonance in Some Semiconductors*, Phys. Rev. **96**, 266 (1954). [Cit. on p. 53]
- [Epp88] R. Eppenga and M. F. H. Schuurmans, *Effect of bulk inversion asymmetry on [001], [110], and [111] GaAs/AlAs quantum wells*, Phys. Rev. B **37**, 10923 (1988). [Cit. on p. 49]
- [Fab07] J. Fabian, A. Matos-Abiague, C. Ertler, P. Stano, and I. Žutić, *Semiconductor Spintronics*, Acta Phys. Slov. **57**, 565 (2007). [Cit. on p. 1, 45]
- [Fai93] J. Faist, F. Capasso, C. Sirtori, D. L. Sivco, A. L. Hutchinson, S. N. G. Chu, and A. Y. Cho, *Measurement of the intersubband scattering rate in semiconductor quantum wells by excited state differential absorption spectroscopy*, Applied Physics Letters **63**, 1354 (1993). [Cit. on p. 42]
- [Fas87] G. Fasol, N. Mestres, A. Fischer, and K. Ploog, *Coupled Plasmons and Single Particle Excitations in the Two-Dimensional Electron Gas*, Physica Scripta **T19**, 109 (1987). [Cit. on p. 59, 61, 69]
- [Fer89] R. Ferreira and G. Bastard, *Evaluation of some scattering times for electrons in unbiased and biased single- and multiple-quantum-well structures*, Phys. Rev. B **40**, 1074 (1989). [Cit. on p. 42]
- [Fer06] A. C. Ferrari, J. C. Meyer, V. Scardaci, C. Casiraghi, M. Lazzeri, F. Mauri, S. Piscanec, D. Jiang, K. S. Novoselov, S. Roth, and A. K. Geim, *Raman Spectrum of Graphene and Graphene Layers*, Phys. Rev. Lett. **97**, 187401 (2006). [Cit. on p. 19]
- [Gam90] D. Gammon, B. V. Shanabrook, J. C. Ryan, and D. S. Katzer, *Spin-density waves in a quasi-two-dimensional electron gas*, Phys. Rev. B **41**, 12311 (1990). [Cit. on p. 35]
- [Gam92] D. Gammon, B. V. Shanabrook, J. C. Ryan, D. S. Katzer, and M. J. Yang, *Exchange and correlation in the nonhomogeneous electron gas in semiconductor heterojunctions*, Phys. Rev. Lett. **68**, 1884 (1992). [Cit. on p. 35]

- [Gan01] S. D. Ganichev, E. L. Ivchenko, S. N. Danilov, J. Eroms, W. Wegscheider, D. Weiss, and W. Prettl, *Conversion of Spin into Directed Electric Current in Quantum Wells*, Phys. Rev. Lett. **86**, 4358 (2001). [Cit. on p. 47]
- [Gan02] S. D. Ganichev, E. L. Ivchenko, V. V. Bel'kov, S. A. Tarasenko, M. Sollinger, D. Weiss, W. Wegscheider, and W. Prettl, *Spin-galvanic effect*, Nature **417**, 153 (2002). [Cit. on p. 47]
- [Gan04] S. D. Ganichev, V. V. Bel'kov, L. E. Golub, E. L. Ivchenko, P. Schneider, S. Giglberger, J. Eroms, J. De Boeck, G. Borghs, W. Wegscheider, D. Weiss, and W. Prettl, *Experimental Separation of Rashba and Dresselhaus Spin Splittings in Semiconductor Quantum Wells*, Phys. Rev. Lett. **92**, 256601 (2004). [Cit. on p. 47]
- [Gig07] S. Giglberger, L. E. Golub, V. V. Bel'kov, S. N. Danilov, D. Schuh, C. Gerl, F. Rohlfing, J. Stahl, W. Wegscheider, D. Weiss, W. Prettl, and S. D. Ganichev, *Rashba and Dresselhaus spin splittings in semiconductor quantum wells measured by spin photocurrents*, Phys. Rev. B **75**, 035327 (2007). [Cit. on p. 47]
- [Gov97] A. O. Govorov, *Resonant light scattering induced by Coulomb interaction in semiconductor microstructures*, J. Phys.: Condens. Matter **9**, 4681 (1997). [Cit. on p. 33]
- [Gri12a] M. Griesbeck, *Spin dynamics in high-mobility two-dimensional electron systems embedded in GaAs/AlGaAs quantum wells*, PhD thesis, Universität Regensburg (2012). [Cit. on p. 16]
- [Gri12b] M. Griesbeck, M. M. Glazov, E. Y. Sherman, D. Schuh, W. Wegscheider, C. Schüller, and T. Korn, *Strongly anisotropic spin relaxation revealed by resonant spin amplification in (110) GaAs quantum wells*, Phys. Rev. B **85**, 085313 (2012). [Cit. on p. 75]
- [Haa92] S. Haacke, R. Zimmermann, D. Bimberg, H. Kal, D. E. Mars, and J. N. Miller, *Fermi enhancement and band-gap renormalization of $\text{Al}_x\text{Ga}_{1-x}\text{As}/\text{GaAs}$ modulation-doped quantum wells*, Phys. Rev. B **45**, 1736 (1992). [Cit. on p. 16]
- [Ham69] D. Hamilton and A. L. McWhorter, *Light Scattering Spectra of Solids*, Springer (1969). [Cit. on p. 33, 34, 57]
- [Hey10] S. Heydrich, M. Hirmer, C. Preis, T. Korn, J. Eroms, D. Weiss, and C. Schüller, *Scanning Raman spectroscopy of graphene antidot lattices: Evidence for systematic p-type doping*, Appl. Phys. Lett. **97**, 043113 (2010). [Cit. on p. 19]
- [Hir11] M. Hirmer, M. Hirmer, D. Schuh, W. Wegscheider, T. Korn, R. Winkler, and C. Schüller, *Fingerprints of the Anisotropic Spin-Split Hole Dispersion in Resonant Inelastic Light Scattering in Two-Dimensional Hole Systems*, Phys. Rev. Lett. **107**, 216805 (2011). [Cit. on p. 47]

- [Hir12] M. Hirmer, *Elektronische Raman-Streuung und die Spin-Bahn-Wechselwirkung in p-dotierten GaAs/AlGaAs Quantentrögen*, PhD thesis, Universität Regensburg (2012). [Cit. on p. 10]
- [Iba09] H. Ibach and H. Lüth, *Festkörperphysik*, Springer (2009). [Cit. on p. 86]
- [Ish14] J. Ishihara, Y. Ohno, and H. Ohno, *Direct imaging of gate-controlled persistent spin helix state in a modulation-doped GaAs/AlGaAs quantum well*, Appl. Phys. Exp. **7**, 013001 (2014). [Cit. on p. 72]
- [Ivc05] E. L. Ivchenko, *Optical Spectroscopy of Semiconductor Nanostructures*, Alpha Science Int. (2005). [Cit. on p. 49, 50, 54]
- [Jac99] J. D. Jackson, *Classical Electrodynamics*, New York: Wiley (1999). [Cit. on p. 45]
- [Jai85] J. K. Jain and P. B. Allen, *Predicted Raman intensities for bulk and surface plasmons of a layered electron gas*, Phys. Rev. Lett. **54**, 947 (1985). [Cit. on p. 31]
- [Jai87] J. K. Jain and S. Das Sarma, *Elementary electronic excitations in a quasi-two-dimensional electron gas*, Phys. Rev. B **36**, 5949 (1987). [Cit. on p. 28]
- [Jus92] B. Jusserand, D. Richards, H. Peric, and B. Etienne, *Zero-magnetic-field spin splitting in the GaAs conduction band from Raman scattering on modulation-doped quantum wells*, Phys. Rev. Lett. **69**, 848 (1992). [Cit. on p. 2, 46, 61]
- [Jus95] B. Jusserand, D. Richards, G. Allan, C. Priester, and B. Etienne, *Spin orientation at semiconductor heterointerfaces*, Phys. Rev. B **51**, 4707 (1995). [Cit. on p. 2, 46, 50]
- [Jus00] B. Jusserand, M. N. Vijayaraghavan, F. Laruelle, A. Cavanna, and B. Etienne, *Resonant Mechanisms of Inelastic Light Scattering by Low-Dimensional Electron Gases*, Phys. Rev. Lett. **85**, 5400 (2000). [Cit. on p. 32, 33, 74]
- [Jus03] B. Jusserand, M. El Kurdi, and A. Cavanna, *Wave vector dependent inter-Landau-level transitions in modulation-doped quantum wells*, Phys. Rev. B **67**, 233307 (2003). [Cit. on p. 87, 89, 90]
- [Kai03] J. Kainz, U. Rössler, and R. Winkler, *Anisotropic spin-splitting and spin-relaxation in asymmetric zinc blende semiconductor quantum structures*, Phys. Rev. B **68**, 075322 (2003). [Cit. on p. 47]
- [Kan57] E. O. Kane, *Band structure of indium antimonide*, Journal of Physics and Chemistry of Solids **1**, 249 (1957). [Cit. on p. 7]
- [Kat03] Y. Kato, R. C. Myers, A. C. Gossard, and D. D. Awschalom, *Coherent spin manipulation without magnetic fields in strained semiconductors*, Nature **427**, 50 (2003). [Cit. on p. 72]
- [Kle85] D. A. Kleinman and R. C. Miller, *Band-gap renormalization in semiconductor quantum wells containing carriers*, Phys. Rev. B **32**, 2266 (1985). [Cit. on p. 16]

- [Kle87] D. A. Kleinman, R. C. Miller, and A. C. Gossard, *Doubly resonant LO-phonon Raman scattering observed with GaAs-Al_xGa_{1-x}As quantum wells*, Phys. Rev. B **35**, 664 (1987). [Cit. on p. 33]
- [Koh12] M. Kohda, V. Lechner, Y. Kunihashi, T. Dollinger, P. Olbrich, C. Schönhuber, I. Caspers, V. V. Bel'kov, L. E. Golub, D. Weiss, K. Richter, J. Nitta, and S. D. Ganichev, *Gate-controlled persistent spin helix state in (In,Ga)As quantum wells*, Phys. Rev. B **86**, 081306 (2012). [Cit. on p. 2, 47, 54, 72]
- [Koo09] H. C. Koo, J. H. Kwon, J. Eom, J. Chang, S. H. Han, and M. Johnson, *Control of Spin Precession in a Spin-Injected Field Effect Transistor*, Science **325**, 1515 (2009). [Cit. on p. 1]
- [Kor09] J. D. Koralek, C. P. Weber, J. Orenstein, B. A. Bernevig, S.-C. Zhang, S. Mack, and D. D. Awschalom, *Emergence of the persistent spin helix in semiconductor quantum wells*, Nature **458**, 610 (2009). [Cit. on p. 2, 47, 53]
- [Kre96] O. Krebs and P. Voisin, *Giant Optical Anisotropy of Semiconductor Heterostructures with No Common Atom and the Quantum-Confined Pockels Effect*, Phys. Rev. Lett. **77**, 1829 (1996). [Cit. on p. 46]
- [Lan46] L. D. Landau, *On the vibrations of the electronic plasma*, Journal of Physics **10**, 25 (1946). [Cit. on p. 30]
- [Lec12] V. Lechner, *Bulk and Structure Inversion Asymmetry in Semiconductor Quantum Well Structures*, PhD thesis, Universität Regensburg (2012). [Cit. on p. 49]
- [Lee10] C. Lee, H. Yan, L. E. Brus, T. F. Heinz, J. Hone, and S. Ryu, *Anomalous Lattice Vibrations of Single- and Few-Layer MoS₂*, ACS Nano **5**, 2695 (2010). [Cit. on p. 19]
- [Lev99] M. Levinshtein, M. Shur, and S. Rumyantsev, *Handbook series on Semiconductor Parameters*, World Scientific (1999). [Cit. on p. 8]
- [Liu93] H. C. Liu, Z. R. Wasilewski, M. Buchanan, and H. Chu, *Segregation of Si delta doping in GaAs-AlGaAs quantum wells and the cause of the asymmetry in the current-voltage characteristics of intersubband infrared detectors*, Appl. Phys. Lett. **63**, 761 (1993). [Cit. on p. 13]
- [Liu07] B. Liu, H. Zhao, J. Wang, L. Liu, W. Wang, D. Chen, and H. Zhu, *Electron density dependence of in-plane spin relaxation anisotropy in GaAs/AlGaAs two-dimensional electron gas*, Appl. Phys. Lett. **90**, 112111 (2007). [Cit. on p. 47]
- [Mal97] A. G. Mal'shukov, K. A. Chao, and M. Willander, *Asymmetries of spin-flip electronic Raman scattering in a III-V semiconductor quantum well*, Phys. Rev. B **55**, R1918 (1997). [Cit. on p. 57]
- [Mar83] V. A. Marushchak, M. Stepanova, and A. Titkov, *Spin relaxation of conduction electrons in moderately doped gallium arsenide crystals*, Sov. Phys. Solid State **25**, 2035 (1983). [Cit. on p. 48]

- [Mil03] J. B. Miller, D. M. Zumbühl, C. M. Marcus, Y. B. Lyanda-Geller, D. Goldhaber-Gordon, K. Campman, and A. C. Gossard, *Gate-Controlled Spin-Orbit Quantum Interference Effects in Lateral Transport*, Phys. Rev. Lett. **90**, 076807 (2003). [Cit. on p. 72]
- [Miu08] N. Miura, *Physics of Semiconductors in High Magnetic Fields*, Oxford University Press (2008). [Cit. on p. 87, 90, 93]
- [Moo66] A. Mooradian and G. B. Wright, *Observation of the Interaction of Plasmons with Longitudinal Optical Phonons in GaAs*, Phys. Rev. Lett. **16**, 999 (1966). [Cit. on p. 81]
- [Nit97] J. Nitta, T. Akazaki, H. Takayanagi, and T. Enoki, *Gate Control of Spin-Orbit Interaction in an Inverted $\text{In}_{0.53}\text{Ga}_{0.47}\text{As}/\text{In}_{0.52}\text{Al}_{0.48}\text{As}$ Heterostructure*, Phys. Rev. Lett. **78**, 1335 (1997). [Cit. on p. 72]
- [Ohn99] Y. Ohno, R. Terauchi, T. Adachi, F. Matsukura, and H. Ohno, *Spin Relaxation in GaAs(110) Quantum Wells*, Phys. Rev. Lett. **83**, 4196 (1999). [Cit. on p. 75]
- [Olb09] P. Olbrich, J. Allerdings, V. V. Bel'kov, S. A. Tarasenko, D. Schuh, W. Wegscheider, T. Korn, C. Schüller, D. Weiss, and S. D. Ganichev, *Magnetogyrotropic photogalvanic effect and spin dephasing in (110)-grown GaAs/ $\text{Al}_x\text{Ga}_{1-x}\text{As}$ quantum well structures*, Phys. Rev. B **79**, 245329 (2009). [Cit. on p. 52]
- [Pin71] A. Pinczuk, L. Brillson, E. Burstein, and E. Anastassakis, *Resonant Light Scattering by Single-Particle Electronic Excitations in n -GaAs*, Phys. Rev. Lett. **27**, 317 (1971). [Cit. on p. 2, 35]
- [Pin80] A. Pinczuk, J. Worlock, H. Störmer, R. Dingle, W. Wiegmann, and A. Gossard, *Inelastic light scattering spectroscopy of a multilayer two-dimensional electron gas*, Surface Science **98**, 126 (1980). [Cit. on p. 2, 35]
- [Pin88a] A. Pinczuk and G. Abstreiter, *Light Scattering in Solids V*, Springer (1988). [Cit. on p. 59]
- [Pin88b] A. Pinczuk, J. P. Valladares, D. Heiman, A. C. Gossard, J. H. English, C. W. Tu, L. Pfeiffer, and K. West, *Observation of roton density of states in two-dimensional Landau-level excitations*, Phys. Rev. Lett. **61**, 2701 (1988). [Cit. on p. 87]
- [Pin89] A. Pinczuk, S. Schmitt-Rink, G. Danan, J. P. Valladares, L. N. Pfeiffer, and K. W. West, *Large exchange interactions in the electron gas of GaAs quantum wells*, Phys. Rev. Lett. **63**, 1633 (1989). [Cit. on p. 35, 40]
- [Ple12] G. Plechinger, S. Heydrich, J. Eroms, D. Weiss, C. Schüller, and T. Korn, *Raman spectroscopy of the interlayer shear mode in few-layer MoS_2 flakes*, Appl. Phys. Lett. **101**, 101906 (2012). [Cit. on p. 19]
- [Ram90] M. Ramsteiner, J. D. Ralston, P. Koidl, B. Dischler, H. Biebl, J. Wagner, and H. Ennen, *Doping density dependence of intersubband transitions*

- in GaAs/Al_xGa_{1-x}As quantum-well structures*, Journal of Applied Physics **67**, 3900 (1990). [Cit. on p. 40]
- [Ras60] E. I. Rashba, *Properties of semiconductors with an extremum loop. 1. Cyclotron and combinational resonance in a magnetic field perpendicular to the plane of the loop*, Sov. Phys. Solid State **2**, 1224 (1960). [Cit. on p. 51]
- [Ric93] D. Richards, B. Jusserand, H. Peric, and B. Etienne, *Intrasubband excitations and spin-splitting anisotropy in GaAs modulation-doped quantum wells*, Phys. Rev. B **47**, 16028 (1993). [Cit. on p. 2, 46, 61]
- [Ric96] D. Richards, B. Jusserand, G. Allan, C. Priester, and B. Etienne, *Electron Spin-Flip Raman Scattering In Asymmetric Quantum Wells: Spin Orientation*, Solid-State Electronics **40**, 127 (1996). [Cit. on p. 2, 46]
- [Ric00] D. Richards, *Inelastic light scattering from inter-Landau level excitations in a two-dimensional electron gas*, Phys. Rev. B **61**, 7517 (2000). [Cit. on p. 89, 91, 92]
- [Ruf90] T. Ruf and M. Cardona, *Nonparabolicity of the conduction band in GaAs*, Phys. Rev. B **41**, 10747 (1990). [Cit. on p. 90]
- [Sal14] G. Salis, M. P. Walser, P. Altmann, C. Reichl, and W. Wegscheider, *Dynamics of a localized spin excitation close to the spin-helix regime*, Phys. Rev. B **89**, 045304 (2014). [Cit. on p. 64]
- [Sas14] A. Sasaki, S. Nonaka, Y. Kunihashi, M. Kohda, T. Bauernfeind, T. Dollinger, K. Richter, and J. Nitta, *Direct determination of spin-orbit interaction coefficients and realization of the persistent spin helix symmetry*, Nature Nanotech. **9**, 703 (2014). [Cit. on p. 55]
- [Sch91] D. Schwarze, H. Stolz, W. von der Osten, G. Weimann, J. Röseler, D. Suiskey, and R. Enderlein, *Doubly resonant first order Raman scattering in narrow GaAsAlGaAs quantum wells: Scattering mechanism and resonance profile*, Superlattices and Microstructures **10**, 389 (1991). [Cit. on p. 33]
- [Sch96] C. Schüller, G. Biese, K. Keller, C. Steinebach, D. Heitmann, P. Grambow, and K. Eberl, *Single-particle excitations and many-particle interactions in quantum wires and dots*, Phys. Rev. B **54**, R17304 (1996). [Cit. on p. 35]
- [Sch97] C. Schüller, R. Krahne, G. Biese, C. Steinebach, E. Ulrichs, D. Heitmann, and K. Eberl, *Multiple cyclotron resonances in GaAs-Al_xGa_{1-x}As quantum wells detected by resonant inelastic light scattering*, Phys. Rev. B **56**, 1037 (1997). [Cit. on p. 87, 91, 92]
- [Sch98] C. Schüller, K. Keller, G. Biese, E. Ulrichs, L. Rolf, C. Steinebach, D. Heitmann, and K. Eberl, *Quasiatomic Fine Structure and Selection Rules in Quantum Dots*, Phys. Rev. Lett. **80**, 2673 (1998). [Cit. on p. 35]
- [Sch03] J. Schliemann, J. C. Egues, and D. Loss, *Nonballistic Spin-Field-Effect Transistor*, Phys. Rev. Lett. **90**, 146801 (2003). [Cit. on p. 2, 47]

- [Sch06] C. Schüller, *Inelastic Light Scattering of Semiconductor Nanostructures*, Springer (2006). [Cit. on p. 2, 3, 6, 10, 19, 20, 25, 26, 27, 28, 29, 31, 32, 34, 57, 70]
- [Sch12] C. Schönhuber, *Realization of the persistent spin helix condition in In-GaAs/InAlAs quantum well structures*, Diploma thesis, Universität Regensburg (2012). [Cit. on p. 49]
- [Sch14] C. Schönhuber, M. P. Walser, G. Salis, C. Reichl, W. Wegscheider, T. Korn, and C. Schüller, *Inelastic light-scattering from spin-density excitations in the regime of the persistent spin helix in a GaAs-AlGaAs quantum well*, Phys. Rev. B **89**, 085406 (2014). [Cit. on p. 47, 58, 59, 60]
- [Sih06] V. Sih, H. Knotz, J. Stephens, V. R. Horowitz, A. C. Gossard, and D. D. Awschalom, *Mechanical control of spin-orbit splitting in GaAs and In_{0.04}Ga_{0.96}As epilayers*, Phys. Rev. B **73**, 241316 (2006). [Cit. on p. 72]
- [Ste67] F. Stern, *Polarizability of a Two-Dimensional Electron Gas*, Phys. Rev. Lett. **18**, 546 (1967). [Cit. on p. 28, 30]
- [Ste99] C. Steinebach, C. Schüller, and D. Heitmann, *Resonant Raman scattering of quantum dots*, Phys. Rev. B **59**, 10240 (1999). [Cit. on p. 71]
- [Ste00] C. Steinebach, C. Schüller, and D. Heitmann, *Single-particle-like states in few-electron quantum dots*, Phys. Rev. B **61**, 15600 (2000). [Cit. on p. 71]
- [Sti07] D. Stich, J. H. Jiang, T. Korn, R. Schulz, D. Schuh, W. Wegscheider, M. W. Wu, and C. Schüller, *Detection of large magnetoanisotropy of electron spin dephasing in a high-mobility two-dimensional electron system in a [001] GaAs/Al_xGa_{1-x}As quantum well*, Phys. Rev. B **76**, 073309 (2007). [Cit. on p. 47]
- [Str94] R. Strenz, U. Bockelmann, F. Hirler, G. Abstreiter, G. Böhm, and G. Weimann, *Single-Particle Excitations in Quasi-Zero- and Quasi-One-Dimensional Electron Systems*, Phys. Rev. Lett. **73**, 3022 (1994). [Cit. on p. 35]
- [Stu09] M. Studer, G. Salis, K. Ensslin, D. C. Driscoll, and A. C. Gossard, *Gate-Controlled Spin-Orbit Interaction in a Parabolic GaAs/AlGaAs Quantum Well*, Phys. Rev. Lett. **103**, 027201 (2009). [Cit. on p. 72]
- [Tat89] M. C. Tatham, J. F. Ryan, and C. T. Foxon, *Time-resolved Raman measurements of intersubband relaxation in GaAs quantum wells*, Phys. Rev. Lett. **63**, 1637 (1989). [Cit. on p. 42]
- [Tse84] A. C. Tselis and J. J. Quinn, *Theory of collective excitations in semiconductor superlattice structures*, Phys. Rev. B **29**, 3318 (1984). [Cit. on p. 28]
- [Ull02] C. A. Ullrich and M. E. Flatté, *Intersubband spin-density excitations in quantum wells with Rashba spin splitting*, Phys. Rev. B **66**, 205305 (2002). [Cit. on p. 56]
- [Ull03] C. A. Ullrich and M. E. Flatté, *Anisotropic splitting of intersubband spin plasmons in quantum wells with bulk and structural inversion asymmetry*, Phys. Rev. B **68**, 235310 (2003). [Cit. on p. 56, 97]

- [Uma09] V. Umansky, M. Heiblum, Y. Levinson, J. Smet, J. Nübler, and M. Dolev, *MBE growth of ultra-low disorder 2DEG with mobility exceeding $35 \cdot 10^6 \text{ cm}^2/\text{Vs}$* , Journal of Crystal Growth **311**, 1658 (2009). [Cit. on p. 11, 15]
- [Unu04] T. Unuma, K. Kobayashi, A. Yamamoto, M. Yoshita, Y. Hashimoto, S. Katsumoto, Y. Iye, Y. Kanemitsu, and H. Akiyama, *Intersubband electronic Raman scattering in narrow GaAs single quantum wells dominated by single-particle excitations*, Phys. Rev. B **70**, 153305 (2004). [Cit. on p. 35, 37, 40, 42, 95]
- [Unu06] T. Unuma, K. Kobayashi, A. Yamamoto, M. Yoshita, K. Hirakawa, Y. Hashimoto, S. Katsumoto, Y. Iye, Y. Kanemitsu, and H. Akiyama, *Collective and single-particle intersubband excitations in narrow quantum wells selected by infrared absorption and resonant Raman scattering*, Phys. Rev. B **74**, 195306 (2006). [Cit. on p. 35, 37]
- [vdL80] D. von der Linde, J. Kuhl, and H. Klingenberg, *Raman Scattering from Nonequilibrium LO Phonons with Picosecond Resolution*, Phys. Rev. Lett. **44**, 1505 (1980). [Cit. on p. 81]
- [Wal12a] M. Walser, C. Reichl, W. Wegscheider, and G. Salis, *Direct mapping of the formation of a persistent spin helix*, Nature Physics **8**, 757 (2012). [Cit. on p. 2, 13, 47, 60, 64, 67, 69, 96]
- [Wal12b] M. P. Walser, U. Siegenthaler, V. Lechner, D. Schuh, S. D. Ganichev, W. Wegscheider, and G. Salis, *Dependence of the Dresselhaus spin-orbit interaction on the quantum well width*, Phys. Rev. B **86**, 195309 (2012). [Cit. on p. 48, 49, 75]
- [Win03] R. Winkler, *Spin-orbit Coupling Effects in Two-Dimensional Electron and Hole Systems*, Springer (2003). [Cit. on p. 7, 10, 46, 49, 52, 86, 89]
- [Win04] R. Winkler, *Spin orientation and spin precession in inversion-asymmetric quasi-two-dimensional electron systems*, Phys. Rev. B **69**, 045317 (2004). [Cit. on p. 1]
- [Wor83] J. Worlock, *Wave vector dependent magneto-optical interband transitions in semiconductors*, Solid State Communications **48**, 1067 (1983). [Cit. on p. 87]
- [Yaf63] Y. Yafet, *g Factors and Spin-Lattice Relaxation of Conduction Electrons*, in F. Seitz and D. Turnbull, Hg., *Solid State Physics*, Bd. 14, Academic Press (1963). [Cit. on p. 53]
- [Yu91] H. Yu and J. C. Hermanson, *Collective electronic excitations in GaAs/Al_xGa_{1-x}As quantum wells*, Phys. Rev. B **43**, 4340 (1991). [Cit. on p. 40]
- [Yug07] I. A. Yugova, A. Grelich, D. R. Yakovlev, A. A. Kiselev, M. Bayer, V. V. Petrov, Y. K. Dolgikh, D. Reuter, and A. D. Wieck, *Universal behavior of the electron g factor in GaAs/Al_xGa_{1-x}As quantum wells*, Phys. Rev. B **75**, 245302 (2007). [Cit. on p. 88]

- [Zib07] T. Zibold, *Semiconductor based quantum information devices: Theory and simulations*, PhD thesis, Technische Universität München (2007). [Cit. on p. 10]
- [Zut04] I. Zutic, J. Fabian, and S. Das Sarma, *Spintronics: Fundamentals and applications*, Rev. Mod. Phys. **76**, 323 (2004). [Cit. on p. 1, 48]

Danksagung

An diesem Punkt möchte ich mich bei allen Menschen bedanken, die mich während der letzten Jahre unterstützt und zum Gelingen dieser Arbeit beigetragen haben.

Ein besonderer Dank gilt Prof. Dr. Christian Schüller, der mir eine Promotion in seiner Arbeitsgruppe ermöglichte. Seine freundliche und interessierte Art wirkte stets motivierend und schuf ein sehr angenehmes Arbeitsklima. Mit zahlreichen Anregungen und einem offenen Ohr für Fragestellungen war er eine große Hilfe. Desweiteren möchte ich mich herzlich bei PD Dr. Tobias Korn bedanken. Bei experimentellen und technischen Problemen opferte er oftmals seine Zeit und stand immer mit guten Ratschlägen zur Seite. Für das Wachsen bzw. Bereitstellen der Proben möchte ich mich bei Dr. Dieter Schuh, Prof. Dr. Dominique Bougeard, Dr. Christian Reichl und Prof. Dr. Werner Wegscheider bedanken. Die speziellen Anforderungen der Persistenten Spin Helix zu erfüllen erfordert großes Geschick im Probenwachstum.

Ein weiterer Dank gebührt allen Mitgliedern der AG Schüller für die nette Zusammenarbeit und das kollegiale Klima. Hierbei sind besonders Philipp Nagler, Gerd Plechinger und Sven Gelfert zu erwähnen – vielen Dank für das Korrekturlesen und wunderbare Erlebnisse auch abseits der Universität. Bei Christian Gradl möchte ich mich für die angenehme Atmosphäre im Büro, zahlreiche Diskussionen und die Unterstützung bezüglich des elektrischen Gates bedanken. Ein großes Dankeschön geht auch an Markus Schwemmer und die Bachelorstudenten Stefan Bauer und Jennifer Zehner für die reibungslose Zusammenarbeit im Labor, sowie an Christof Ermer und Sebastian Krug für die Hilfe bei technischen Problemen.

Ein spezieller Dank gilt meinen Eltern. Sie ermöglichten mir diesen Weg einzuschlagen und standen mir schon immer mit vollster Unterstützung zur Seite. Vielen Dank auch an meine Brüder und deren Familien, da ich weiß, dass ich immer auf sie zählen kann. Zu guter Letzt möchte ich mich noch bei meiner Freundin bedanken. Durch ihre motivierenden Worte war sie eine große Stütze und zudem sorgte sie immer für den nötigen Ausgleich neben der Universität.